

**NEAR FIELD FORWARD SCATTERING, AND OBJECT-BASED
LOCALIZATION ALGORITHMS FOR SUBSURFACE OBJECTS**

A Thesis Presented

by

Adnan Şahin

to

The Department of Electrical and Computer Engineering

in partial fulfillment of the requirements

for the degree of

Doctor of Philosophy

in the field of

Electrical Engineering

Northeastern University

Boston, Massachusetts

August 20, 1998

Abstract

Non-invasive detection and localization of objects in the near field of a receiver array have been of interest to many researchers in recent years. Some of the most promising application areas for this technology include landmine remediation, where relatively small metallic or plastic objects are located a few centimeters from the sensors, and hazardous waste remediation, where relatively large metallic objects (eg. steel metal drums) are located on the order of meters from the sensor array. In this thesis, we consider a form of this problem where a plane wave illuminates the region of interest, which is assumed to be a homogeneous, possibly lossy medium containing one or more targets located in the near field of an array of receivers.

In the first part of the thesis we deal with the forward scattering problem in order to obtain an efficient, flexible, and stable algorithm. The forward problem refers to calculation of the scattered fields given the scatterer geometry and properties, and the incident field. Because we intend to use the forward solver as a part of information extraction algorithms, it should lend itself to repeated uses while keeping the computational complexity within practical limits. Specifically, we are interested in development and verification of a recursive algorithm capable of computing scattered fields from multiple dielectric and/or metallic objects in the near field of the array. These conditions are typical of mine detection problems for which the scattered field is observed in the near field, and a mixture of metallic and

dielectric objects may be present in the same medium. For this purpose, we present an alternative tessellation scheme and a modification to Chew’s well-known recursive T-matrix algorithm

In the second part of the thesis, we deal with the inverse problem and introduce algorithms that can detect and localize subsurface objects for near-field measurement geometries. The inherent array structure of the problem suggests that the high resolution array processing techniques quite popular in signal processing community would be well suited for the subsurface detection problem. Based on such a technique, called the Multiple Signal Classification (MUSIC) algorithm, we present two subsurface detection algorithms: computationally simple, but approximate, subarray processing, and computationally intensive, but accurate, matched field processing. Finally, we derive the Cramér-Rao performance bounds for the multiple object detection scenario where the observations are made in the near field. Analytical bounds of estimated object coordinates are then validated by running Monte-Carlo experiments for the MUSIC-based estimator.

Acknowledgements

Writing the acknowledgment part has been one of the most difficult parts of the thesis. It is nearly impossible for me to describe my gratitude in mere words for the wonderful people who have helped and supported me during this ordeal. First, and foremost, I would like to thank my advisor, Prof. Eric Miller, for his guidance, support, and understanding. As he promised, Eric has been an exceptional advisor and mentor, both academically and personally. It was a great pleasure for me to work with him during the last four years.

In addition, I am grateful to Professors Dana Brooks and Carey Rappaport for serving in my thesis committee and providing me with valuable feedback on various parts of my thesis on different occasions.

I would also like to acknowledge the financial support by the Department of Energy under contract DE-FC07-95ID13395, the Army Research Office Demining MURI under Grant DAAG55-97-1-0013, an ODDR&E MURI under Air Force Office of Scientific Research contract F49620-96-1-0028, and a CAREER Award from the National Science Foundation MIP-9623721.

It has been a rewarding and invaluable experience for me to be with talented faculty,

students and staff of Electrical and Computer Engineering, and particularly two prominent research powerhouses: Center for Electromagnetics Research (CER) and Communications and Digital Signal Processing (CDSP) Center. Special thanks to my friends and peers at Northeastern who have made graduate school life more enjoyable.

As I have always been, I am grateful to my parents for supporting my educational endeavors financially and emotionally. They have helped me develop a curious mind, encouraged me to study and learn “from cradle to grave”, and most importantly provided a loving and respectful family.

Finally, the graduate school took most of its toll on two persons that I love dearly, my wife İmge and my daughter Şule. I dedicate this thesis to them, and thank them for their never-ending patience, understanding, love, and support.

Contents

1	Introduction	1
1.1	An Overview of Forward and Inverse Scattering Algorithms	3
1.2	Contributions	6
1.2.1	Forward Scattering	6
1.2.2	Detection and Localization	7
1.3	Thesis Organization	11
2	Background	13
2.1	T Matrix Background	14
2.1.1	Single Scatterer T Matrix	15
2.1.2	Recursive T-matrix Algorithm	16
2.2	Multiple Signal Classification (MUSIC) Algorithm	19
3	Forward Scattering Model	23
3.1	An Alternative Tessellation for Conducting Scatterers for Recursive T-matrix Algorithms	24

3.1.1	Numerical Results	26
3.1.2	Summary	29
3.2	A Modified Recursive T-Matrix Algorithm for Near Field Scattering	29
3.2.1	Determination of Scattering Origin	30
3.2.2	Problems With Higher Order Harmonic Expansions	32
3.2.3	Modified Recursive T-Matrix Algorithm	34
3.2.4	Numerical Results	35
3.2.5	Summary	42
4	Detection and Localization: Subarray Processing	43
4.1	Introduction	43
4.2	Algorithm	46
4.2.1	Sub-array Processing	48
4.2.2	Crossing Analysis	50
4.2.3	Target Extraction	54
4.2.4	Frequency Diversity	55
4.3	Single Object Localization Examples	56
4.4	Multiple Object Localization Examples	59
4.4.1	Multiple Mine-like Objects	60
4.4.2	Multiple Drum-like Objects	68
4.5	Summary	74

5	Detection and Localization: Matched Field Processing	75
5.1	Introduction	76
5.2	Data Model	78
5.3	Matched Field Processing for Object Localization	80
5.3.1	Single Object Localization	80
5.3.2	Multiple Object Localization: No Interaction	84
5.3.3	Multiple Object Localization: With Interaction	86
5.4	Cramér-Rao Performance Bounds on Object Localization	89
5.5	Examples	91
5.5.1	Multiple Object Localization: No Interaction	92
5.5.2	Multiple Object Localization: With Interaction	96
5.5.3	Verification of Cramér-Rao bounds	98
5.6	Summary	101
6	Contributions, Future Work, and Conclusions	103
6.1	Contributions	103
6.1.1	Forward Scattering	104
6.1.2	Detection and Localization	106
6.2	Future Work	108
6.2.1	Forward Scattering Model	109
6.2.2	Detection and Localization	110
6.3	Closing	111

CONTENTS

vii

A Translation Matrices	113
B Bound on Electromagnetic Interactions	116
C A Simplified Proof for Frequency Diversity	120
D Derivatives of Fields in Recursive T Matrix Algorithm	123
Bibliography	127

List of Figures

2.1	Near-field geometry and translation matrices	17
2.2	Array processing when the sources are infinitely far away from the sensor array	20
2.3	Array processing problem geometry	22
3.1	Tessellation of metallic cylinders along their perimeters	25
3.2	Comparison of normalized scattering field pattern calculated using the recursive T-matrix algorithm with the analytically calculated one.	27
3.3	Comparison of normalized scattering field pattern calculated using the recursive T-matrix algorithm with [63].	28
3.4	Comparison of normalized power density calculated using the recursive T-matrix algorithm with [64].	28
3.5	Scattering Origin Regions	31
3.6	Convergence pattern of the truncated sum in the addition formula for M=5.	33
3.7	Comparison of echo width with [65] for two equal dielectric cylinders	36
3.8	Comparison of echo width with [65] for two cylinders, one lossy dielectric and one metallic	37

3.9	Scattered electric fields from 3 dielectric objects	38
3.10	Scattered electric field from 2 metallic and a dielectric objects	39
4.1	Single object localization with SAP: metallic mine-like object in lossy back-ground	46
4.2	Multiple object subarray processing concept: directions of arrivals and crossing pattern	47
4.3	Flow chart of the algorithm	47
4.4	Fitness to Poisson model for the example of Fig. 4.6. Solid lines are fitted to data using linear least squares	51
4.5	The estimation error plotted against background and signal to noise ratio variations. The images in (a)–(c) represent the base 10 logarithm of the error. Thus, values below zero indicate that the center of the object can be localized to within the support of the target.	58
4.6	Multiple mine-like object detection with SAP: object on the left is metallic and object on the right is dielectric with $\epsilon_r = 2.5$. o's and *'s denote subarrays	61
4.7	Multiple mine-like object detection with SAP: geometry for the example about the effect of relative distance between objects. Both objects are perfect conductors	62
4.8	Probability of detection of the fixed object when the other object moves under the receiver array	64

4.9	Probability of false alarm, when the moving object is located under the receiver array at various positions, dashed line shows the desired false alarm rate of 10^{-3}	65
4.10	Estimation errors in object centers, each symbol corresponds to a different position of the moving object. Number of symbols in (b) is considerably less, since the fixed object is not detected for all positions of the moving object, see Fig. 4.8.	66
4.11	Histogram of distances between two objects whose coordinates are obtained from independent, uniform random variables	67
4.12	SAP results of randomly placed objects for $P_{fa} = 0.1$ [(a)–(b)], $P_{fa} = 10^{-3}$ [(c)–(d)], and $P_{fa} = 10^{-6}$ [(e)–(f)]. The dashed lines indicate the radii of the objects, and the dotted lines indicate the diameter of the objects	69
4.13	Localization of two metallic drum-like objects with SAP, o's and *'s denote subarrays	70
4.14	Multiple drum-like object detection with SAP: geometry for the example about the effect of relative distance and depth between objects. Both objects are perfect conductors	71
4.15	Probability of detection of the moving object, when the fixed object is located at (-40,-125)cm. The solid line and dashed lines show the probability of detection when the moving object is at depth -125 cm and -137.5 cm, respectively.	71

4.16	Estimation errors in object centers, each symbol corresponds to a different position of the moving object. Number of symbols in (b) is less than that in (a), since it is not detected for all positions of the moving object, see Fig. 4.15.	73
5.1	MFP localization example: single metallic object in a lossy, homogeneous background	83
5.2	Example geometries used in multiple object localization	92
5.3	Electromagnetic interaction between scatterers, and its effect on estimated object coordinates when the objects are 15 cm away from the receiver array (top plots) and 25 cm away (bottom plots)	94
5.4	Localization of two targets located 1 meter apart, electromagnetic interactions are ignored	95
5.5	Localization fails when the target centers are 10cm apart in the no interaction case	96
5.6	Convergence of four-dimensional search into the true object coordinates when the objects are 1 meter apart, *'s indicate the initial guess, and the large circle indicates the support of the objects	97
5.7	Convergence of four-dimensional search into the true object coordinates when the objects are 10 cm apart. *'s indicate the initial guess, and large circles indicate the support of the objects	98
5.8	Comparison of analytical CRB with Monte-Carlo simulations for single object geometry given in Fig 5.1(a)	99

5.9	Comparison of analytical CRB with Monte-Carlo simulations for multiple ob- ject geometries given in Fig. 5.2	100
B.1	Finding the scattered field due to a filamentary object by incorporating the electromagnetic interactions between two scatterers step by step. Steps 2 and 3 are repeated infinitely many times successively to account for all interactions	117

List of Tables

3.1	Cost comparison for recursive algorithms. All numbers in FLOPS/ 10^6 , and c/p means convergence problems in near field calculations	40
3.2	Parameter list for Table 3.1	40
4.1	Results of localization of randomly located objects. $\langle K \rangle$ is the mean threshold averaged over 1000 realizations.	67

Chapter 1

Introduction

Non-invasive detection and localization of subsurface objects is an important application area for research on object detection. Potential practical applications include mine field remediation [1–3], waste drum recovery [1, 3], pipeline localization [4], archaeological site characterization [4], etc. Among these, mine field remediation and waste drum recovery have become very popular in recent years and these applications will be the main focus of the research presented in this thesis.

The detection and localization problems require two computation tools: forward scattering and inverse scattering codes. In the electromagnetic forward scattering problem, given the scatterer geometry and the excitation (incident field), the scattered field is determined by solving Maxwell’s equations. Even though there are many simplified scattering models for the forward problem [5–9], these are limited in scope, and for the most general problems

exact forward solvers are needed [10–17]. Within a detection and localization context, inverse scattering means determining object geometry for known incident and scattered fields. Most inverse problems need fast and efficient forward solvers, since the forward problem is solved repeatedly [1, 8, 18–22] in such algorithms. The inherent difficulty in solving the inverse problem is aggravated in subsurface detection because the scattered field can only be observed at limited locations, such as on the earth surface for ground penetrating radar (GPR) applications.

The research presented here spans both sides of the object detection problem: in the first part we will deal with the forward problem in order to obtain an efficient, flexible, and stable algorithm. The forward solver should lend itself to repeated uses while keeping the computational complexity within practical limits. Specifically, we are interested in development and verification of a recursive algorithm capable of computing scattered fields from multiple dielectric and/or metallic objects in the near field. These conditions are very typical of mine detection problems employing GPR-type measurement geometries, for which the scattered field is observed in the near field, and a mixture of metallic and dielectric objects may be present in the same medium. For this purpose, we present an alternative tessellation scheme and a modification to Chew’s well-known recursive T-matrix algorithm [14, 15, 23–27].

In the second part, we will deal with the inverse problem and introduce algorithms that can detect and localize subsurface objects for GPR-type measurement geometries. The inherent array structure of the GPR problem suggests that the high resolution array processing techniques [28, 29] quite popular in signal processing community would be well suited

for the subsurface detection problem. Based on such a technique, called the Multiple Signal Classification (MUSIC) algorithm, we will present two subsurface detection algorithms: computationally simple subarray processing, and computationally intensive, yet accurate, matched field processing [30–32]. Of particular interest here are problems for which we know the shapes of the targets. This assumption is quite reasonable for practical applications such as mine detection and waste drum recovery. The physical phenomenon associated with forward scattering for detection part is further simplified by ignoring the air-earth interface. However, the inverse algorithms themselves are independent of the forward solver, and can be used when air-earth interface is present.

1.1 An Overview of Forward and Inverse Scattering Algorithms

In general, all inverse problem algorithms are associated with a forward solver, which produce the scattered field given the incident field, object characteristics and locations, and the medium of propagation. In most inverse problems, the Born approximation [5] is used as the forward solver. The Born approximation is attractive since it uses a linear forward scattering model, based on the assumption that the scatterers do not disturb the medium of propagation significantly. Therefore, it is appropriate for cases where the dielectric contrast between the scatterer and the background is small. The Born approximation may also be used in an iterative scheme to improve the performance [18,33] of the inversion algorithm. There

are other simplifications to the scattering model similar to the Born approximation which attempt to relax the small perturbation limit such as the extended Born approximation [6] which improves upon the Born approximation by introducing a computationally manageable yet highly accurate non-linearity in the scattering model [19] appropriate for low frequency problems. The advantage of using any of these approximations, of course, is the simplification in the scattering model which results in computationally less demanding algorithms. Some inverse scattering algorithms, on the other hand, use exact forward solvers such as the method of moments, finite differences, fast multipole methods and the transition matrix (T-matrix). Even though these techniques ideally solve the exact problem, finite precision arithmetic, discretization and truncation may introduce a certain amount of error in the fields which are calculated.

The most popular of the exact techniques, the method of moments (MoM) [10], is based on a fine discretization of the region of interest and requires the inversion of a large dense matrix to calculate the scattered field. As this task requires $O(N^3)$ calculations where N is the number of grid points, MoM is known to be computationally quite intensive. The fast multipole technique [11] developed recently can reduce the complexity of MoM-type problems, and can be used alternatively as a fast forward solver. Finite difference techniques are also frequently used as forward solvers and like MoM rely on a full space discretization. Although the resulting matrices are sparse, one still faces the delicate task of specifying an absorbing boundary condition to terminate the computational grid. Unlike finite difference techniques, the T-matrix approach does not require an absorbing boundary condition and

substitutes the discretization of space with harmonic expansions of the fields, thereby reducing the number of unknowns for a wide range of problems. Furthermore, due to spatial discretization, finite difference and MoM methods are used in inverse problems where pixelated reconstructions (i.e. images) are required. The T-matrix method, on the other hand, can be used within object-based localization framework.

Chew and co-workers have pioneered the development of a number of fast, recursive T-matrix algorithms for determining the scattered fields in a variety of scenarios [14, 15, 23–27]. These methods basically function by tessellating electrically large objects into small sub-scatterers whose individual T matrices can be well represented using low-order harmonic expansions. A recursive formula then is used to aggregate the effects of all the sub-scatterers to compute the fields.

In subsurface object detection most often a pixel-by-pixel map of the region of interest is produced and the detection is then performed by post-processing the image [4, 8, 20–22, 34]. However, since the inverse problem is inherently ill-posed, this image-then-detect approach is quite sensitive to noise. While the ill-posedness can be off-set through regularization [35, 36], typical regularization methods result in smooth images thereby making the detection all the more difficult. On the other hand, making use of the fact that the ultimate goal of the problem is the localization of objects with known structures, we can reparameterize the problem within the object-based detection framework [1, 37–41] where a small parameter vector containing the coordinates of the objects is identified. By constraining the degrees of freedom in this manner, ill-posedness is substantially reduced and the resulting algorithms

prove to be robust to noise.

1.2 Contributions

In this section, we review the contributions of this thesis to the forward scattering, and object detection and localization areas.

1.2.1 Forward Scattering

For the forward scattering problem, we desire to solve scattering problems in the near field for the linear array geometry shown in Fig. 2.1. Specifically, we are interested in the development and verification of a recursive algorithm capable of computing scattered fields from multiple dielectric and/or metallic objects in the near field. For simplicity, we considered an E_z polarized plane wave incident on a two dimensional problem geometry in which multiple scatterers each possessing a circular cross-section (*i.e.*, infinite circular cylinders) are located in an infinite medium of constant complex permittivity. Rather than decomposing each full scatterer into a large number of small sub-objects, the goal here is to develop a recursion based on higher-order harmonic expansions for the individual, large objects. The result is an algorithm comprised of a small number of high dimensional T-matrix computations rather than a large number of low dimensional recursions with the idea that the former approach will be more efficient than the latter. For the near-field calculations, however, we show that the higher-order expansions result in instabilities in the original recursions developed by Chew. By modifying these recursions, we obtain a stable algorithm which is capable of both

near and far-field computations. Finally, we demonstrate that this approach retains the low asymptotic computational complexity of the method in [15] but in practice requires far fewer floating point operations.

In addition to this contribution, we will also show that the original T-matrix recursions can be used for metallic scatterers by tessellating such objects along their circumferences with small metallic cylinders. In [26,27,42], Gürel et al. use metallic strips and patches, whose individual T matrices are found via MoM. Alternatively, we use small sub-cylinders along the perimeter of conducting scatterers for tessellation [16]. The advantage of tessellating conducting objects with small metallic cylinders rather than strips or patches is that one need not use MoM to find the T matrices of individual metallic cylinders.

The contributions in this area can be summarized as:

- Definition and determination of an “optimum scattering origin” for the recursive T-matrix algorithm in the near field,
- Modification of the original recursive algorithm in order to circumvent a convergence problem that stems from near field observations and the optimum scattering origin,
- Introduction of an alternative tessellation scheme for metallic scatterers for recursive T-matrix algorithm.

1.2.2 Detection and Localization

For the detection and localization part we introduce algorithms that are especially useful for ground penetrating radar (GPR) type measurement geometries of Fig. 2.3. The algorithms

presented here are some of the earliest applications of high resolution array processing in the subsurface object localization area. The only previous work in this area before this thesis is a work by a group of European researchers [43]. The work in [43] concentrates on polarimetric radar imaging with MUSIC algorithm. Our work is different in that we take an object-based approach rather than an imaging approach. Therefore, the localization algorithms presented in this thesis are the first ones that detect and localize subsurface, near field objects using the MUSIC algorithm.

Of particular interest here are problems for which we know the shapes of the targets. This assumption is quite reasonable for practical applications such as mine detection and waste drum recovery. The subarray processing (SAP) does not require the knowledge of electrical characteristics and the number of targets for detection and localization. The matched field processing (MFP) based algorithm, however, does require the knowledge of these quantities. For practical problems like mine detection, the electrical properties of the targets are usually known as well as the shapes. The number of objects in the region of interest can be estimated using signal processing techniques like information theoretic criterion of Akaike [44,45] or the Minimum Description Length (MDL) criterion [46,47]. Alternatively, the number of objects in the region can be determined by first using SAP which will also give rough estimates of the object locations. These rough estimates can then be used to initialize the MFP.

To be precise, the problem we address in this part is the localization of single or multiple, cylindrical objects, buried in a known, homogeneous, lossy background. The objects can all be metallic, all dielectric or a collection of both. The physical phenomenon associated with

forward scattering for detection part is further simplified by ignoring the air-earth interface. However, the algorithms themselves are independent of the forward solver, and can be used when air-earth interface is present.

The subarray processing involves two processing steps. First, we partition the receiver array such that the scattered field from the targets are locally planar at each sub-array, then use the so-called MUSIC algorithm [48] for plane waves to obtain a set of directions of arrivals (DOA) for each locally planar wave. By triangulating these angles, a collection of crossings, crowding the expected object locations, are acquired. Second, we extract clusters of the crossings which are then declared estimates of object locations. In this second stage, the crossings are modeled as Poisson distributed points, which have a large rate parameter around the targets and a low rate parameter elsewhere. The target locations can be determined by applying hypothesis testing to see whether target-sized windows have high rate parameter of a target or low rate parameter of the background. We demonstrate the performance of this approach for the detection and localization of multiple mine-like and drum-like targets located in the near field of the receiver array. For mine-like targets relative positions of the objects are changed to see the effect of object geometry on detectability. We show that the detectability improves and false alarm rate decreases when the objects are located far apart. For drum-like targets, we demonstrate the effect of relative depth as well as relative distance between objects on detectability.

For the matched field processing based algorithm, we modify MUSIC so that the direction vector is composed so as to model the type of wavefront which is impinging on the array.

Therefore, the problem of non-planar wavefronts is overcome, and an estimate of both angle and range can be produced. We demonstrate that using MFP, single and multiple objects can be localized very accurately over a wide range of signal to noise ratios. In addition, we derive the Cramér Rao performance bound for both single and multiple object cases. Our Cramér-Rao Bound derivation adapts the results in [49], and accounts for near field observations. Analytical bounds on estimated object coordinates are then validated by running Monte-Carlo experiments for the MUSIC estimator.

Previously published work in this area can be categorized in two groups: distributed source localization and near field point source localization. In the area of distributed source localization, Valaee et al. [50] introduced a MUSIC-based localization algorithm that parametrically localizes far field distributed sources. In [50], the far field sources are modeled with bell shaped distributions characterized by their peak position and 3dB beam-width. They successfully localize coherent and incoherent sources. Our work is different from their work in that the sources (or scatterers) in our problem are in the near field of the array. Furthermore, even though the sources in our work are extended as in [50], our source model is governed by the electromagnetic scattering, not by bell shaped source distributions. In the area of near field source localization, previous work has been limited to independently radiating, point sources [51–54]. Coherent source localization in near field is also dealt with in [52]. In [51, 52], independent, spherical sound and noise sources are located using MUSIC based array processing methods. In [53] and [54], a similar near-field source localization scenario is considered, and performance bounds for coordinate estimates were derived

for MUSIC and higher order ESPRIT based algorithms, respectively. In this thesis different from previous work, we consider extended multiple sources whose radiation pattern depends on the relative positions of other scatterers.

The contributions in this area can be summarized as:

- Introduction of MUSIC-based subarray processing for localization of both single and multiple objects,
- Introduction of MUSIC-based matched field processing for localization of both single and multiple objects,
- Derivation of analytical Cramér-Rao bounds, and verification of these bounds with Monte-Carlo simulated error variances.

1.3 Thesis Organization

The rest of the thesis is organized as follows. Chapter 2 contains background material for T matrix algorithms. Single scatterer T-matrix method, and multiple scatterer recursive T-matrix algorithms are described in detail. In addition, the multiple signal classification algorithm (MUSIC) for plane wave incidence is explained in this chapter. In Chapter 3, a modified recursive T-matrix will be given along with an alternative tessellation scheme for conducting objects. In Chapter 4, we describe the subarray processing (SAP), and discuss the Poisson modeling of crossings. In Chapter 5, we explain the matched field processing (MFP) for localization of single and multiple targets. We also discuss the signal coherence issue,

and attempt to decorrelate the autocovariance matrix using frequency diversity. Finally, in Chapter 6, we summarize the results and contributions of this thesis, and indicate future research directions.

Chapter 2

Background

In the first part of this chapter, a brief overview of the T matrix theory and the recursive T-matrix algorithm of [33] will be presented. Because of its efficiency in calculating scattered fields from simple shapes, the recursive T-matrix method is an appropriate forward solver for subsurface detection of objects which are modeled well by simple shapes. Thus, it will be our choice of forward solver throughout this work. Since in later parts of the research we have modified this algorithm, it is appropriate to review the technique here, while our contributions to the forward solver are presented in Chapter 3. In the second part of this chapter, we describe the Multiple Signal Classification (MUSIC) algorithm for determining direction of arrival (DOA) of plane waves and its application to subsurface object detection when the objects are infinitely far from the receiver array. Since the MUSIC algorithm forms the basis for both our detection algorithms, we felt it necessary to review the theory behind MUSIC here, before we introduce our algorithms in Chapters 4 and 5.

2.1 T Matrix Background

As we have mentioned in Chapter 1, inverse scattering algorithms need fast and efficient forward solvers. In this work, the T matrix based recursive algorithm will be used as the fast forward solver, since it is very efficient in finding the scattered field from simple shapes.

Around the late 1960s, Waterman developed the T matrix theory for acoustic scattering problems [55] for single scatterer, and later extended the results for electromagnetic scattering problems [56]. Then, Peterson and Ström developed an iterative scheme that employed the T matrix theory [57, 58] to find the fields from multiple scatterers. Since their work, T matrix theory has been widely used in acoustic and electromagnetic scattering problems [59]. Chew and co-workers have pioneered the development of a number of fast, recursive T-matrix algorithms for determining the scattered fields in a variety of scenarios [14, 15, 23–27]. These methods basically function by tessellating electrically large objects into small sub-scatterers whose individual T matrices can be well represented using low-order harmonic expansions. A recursive formula then is used to aggregate the effects of all the sub-scatterers to compute the fields. Here, we will review the T matrix theory and describe the recursive T-matrix algorithm.

2.1.1 Single Scatterer T Matrix

The total scalar electromagnetic (or acoustic) wave in a homogeneous background with a homogeneous scatterer is given by¹:

$$\psi(\underline{r}) = \psi^{inc}(\underline{r}) + \psi^{sca}(\underline{r}) \quad (2.1)$$

where $\psi^{inc}(\underline{r})$ is the wavefield incident on the scatterer and $\psi^{sca}(\underline{r})$ is the field scattered from the object.

Applying the Poincaré-Huygens principle and the Gauss theorem we can write the total field outside the scatterer as [58]:

$$\psi(\underline{r}) = \psi^{inc}(\underline{r}) + \int_S dS' \{ \psi_+(\underline{r}') \nabla' g(k|\underline{r} - \underline{r}'|) - [\nabla'_\perp \psi(\underline{r}')] g(k|\underline{r} - \underline{r}'|) \} \quad (2.2)$$

where S is a piecewise smooth surface enclosing the scatterer, ψ_+ and $\nabla'_\perp \psi$ are the total field $\psi(\underline{r})$ and its gradient on the outer surface of the scatterer, and $g(k|\underline{r} - \underline{r}'|)$ is the free space Green's function. The vectors \underline{r} and \underline{r}' are from the scattering origin to observation points and to source points on the scatterers, respectively. The Green's function can be expanded in terms of cylindrical basis functions (in 2-D) as follows [58]:

$$g(k|\underline{r} - \underline{r}'|) = -j \frac{\pi}{2} \sum_n \psi_n(k\underline{r}_>) Rg\psi_n(k\underline{r}_<) \quad (2.3)$$

where $\psi_n(k\underline{r}) = H_n^{(2)}(kr)e^{-jn\phi}$ are the basis functions representing traveling waves and $Rg\psi_n(k\underline{r}) = J_n(kr)e^{-jn\phi}$ are the basis functions representing the standing waves. Here, Rg stands for “regular part of”, $H_n^{(2)}(z)$ is the n th order Hankel function of second kind, $J_n(z)$ is the n th order Bessel function, and $\underline{r}_>$ ($\underline{r}_<$) means the larger (smaller) of \underline{r} and \underline{r}' .

¹The time factor of $e^{j\omega t}$ is suppressed

Based on the same decomposition, the scattered and incident fields can be expanded as [58]:

$$\psi^{sca}(\underline{r}) = \sum_n f_n \psi_n(\underline{r}) = \underline{\psi}^T \underline{f} \quad \text{if } |\underline{r}| > |\underline{r}'| \quad (2.4)$$

and

$$\psi^{inc}(\underline{r}) = \sum_n a_n Rg\psi_n(\underline{r}) = Rg\underline{\psi}^T \underline{a} \quad (2.5)$$

where $\underline{\psi}$ and $Rg\underline{\psi}$ are column vectors filled with $\psi_n(\underline{r})$ and $Rg\psi_n(\underline{r})$, respectively and T stands for transposition.

The T-matrix now is defined as [55,58]:

$$\underline{f} = \mathbf{T}\underline{a}. \quad (2.6)$$

The elements of \mathbf{T} can be found by using (2.2), (2.3) and the boundary conditions. For a detailed analysis of the single object T-matrix method, the reader is referred to [55,56,58].

2.1.2 Recursive T-matrix Algorithm

The recursive T-matrix algorithm [15,33,60] uses the basic principle of single scatterer T-matrix formulas in that for each object, the scattered fields from others are assumed a part of total incident field. This way for every scatterer a T-matrix can be assigned. The recursion starts with the T-matrices of individual scatterers, then one by one scatterers are incorporated into the equation and the T-matrices are updated until, for every scatterer, the final form of the T-matrix, including all multiple scattering effects, is obtained.

Formally, for L scatterers, the harmonic expansion of scattered field, similar to (2.4), can

be written as [15]:

$$\psi^{sca}(\underline{r}) = \sum_{i=1}^L \underline{\psi}^T(\underline{r}_i) \mathbf{T}_{i(L)} \boldsymbol{\beta}_{i,0} \underline{a} \quad (2.7)$$

where $\mathbf{T}_{i(L)}$ is the T-matrix for i th object in the presence of L scatterers and $\boldsymbol{\beta}_{i,0}$ is the translation matrix used to translate same type basis functions between scattering coordinate center (x_s, y_s) and i th object's local coordinate center (x_i, y_i) , *i.e.* *standing* waves in i th local coordinate system to *standing* waves in 0th (scattering) coordinate system; or *traveling* waves in i th local coordinate system to *traveling* waves in 0th (scattering) coordinate system. The translation matrix $\boldsymbol{\beta}$ contains Bessel functions and complex exponentials. For details about this matrix see Appendix A.

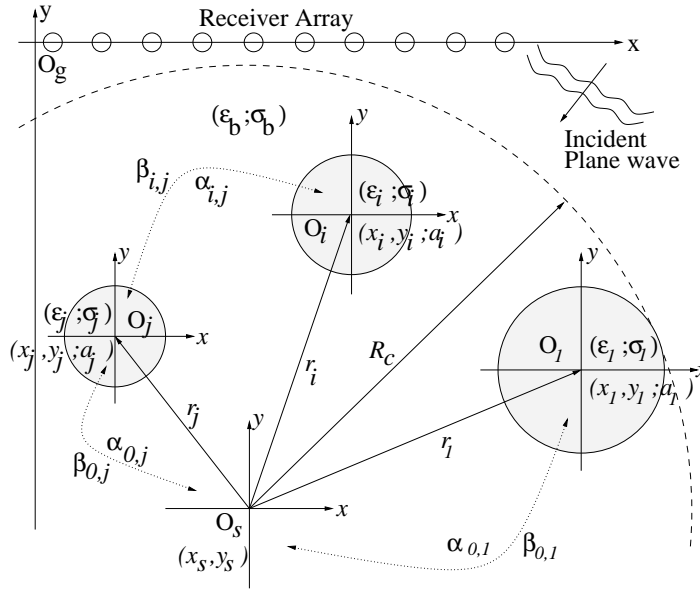


Figure 2.1: Near-field geometry and translation matrices

Fig. 2.1 pictorially shows the coordinate systems and how the translation matrices work. Expansion of the scattered field in (2.7) is valid if all observation points are outside the circle enclosing all scatterers. Following Chew's derivation, the recursive construction of $\mathbf{T}_{i(L)}$ can

be written as [15, eq.10-11] :

$$\mathbf{T}_{n+1(n+1)}\boldsymbol{\beta}_{n+1,0} = \left[\mathbf{I} - \mathbf{T}_{n+1(1)} \sum_{i=1}^n \boldsymbol{\alpha}_{n+1,i} \mathbf{T}_{i(n)} \boldsymbol{\beta}_{i,0} \boldsymbol{\alpha}_{0,n+1} \right]^{-1} \mathbf{T}_{n+1(1)} \left[\boldsymbol{\beta}_{n+1,0} + \sum_{i=1}^n \boldsymbol{\alpha}_{n+1,i} \mathbf{T}_{i(n)} \boldsymbol{\beta}_{i,0} \right] \quad (2.8)$$

and

$$\mathbf{T}_{i(n+1)}\boldsymbol{\beta}_{i,0} = \mathbf{T}_{i(n)}\boldsymbol{\beta}_{i,0} + \mathbf{T}_{i(n)}\boldsymbol{\beta}_{i,0}\boldsymbol{\alpha}_{0,n+1}\mathbf{T}_{n+1(n+1)}\boldsymbol{\beta}_{n+1,0} \quad (2.9)$$

where $n = 1, 2, \dots, L$, $i = 1, 2, \dots, n$ and $\boldsymbol{\alpha}_{n,i}$ is the translation matrix used to change different basis functions between reference coordinate systems (Fig. 2.1), *i.e.* *standing* waves in n th local coordinate system to *traveling* waves in i th local coordinate system. For definition, and structure of the matrix $\boldsymbol{\alpha}$, the reader is referred to Appendix A. The recursion starts with the individual T-matrices, $\mathbf{T}_{i(1)}$, of the scatterers, *i.e.* the T-matrix of the i th scatterer when there are no other scatterers in the medium.

Because of the requirements on the loci of observation points imposed by (2.4) for single objects and (2.7) for multiple objects, the scattering origin O_s in Fig. 2.1 should be carefully selected. The field expansions require that the scattering origin (x_s, y_s) relative to O_g must be selected such that there must be at least one circle, centered at (x_s, y_s) , encircling all objects with no receivers inside it. When the observation points are in the far field, selection of the scattering origin is not critical, since it is guaranteed that the receivers are outside the limiting circle. For near field observations, however, the scattering origin needs to be selected using the criterion presented in Section 3.2.1.

Theoretically the matrices $\boldsymbol{\alpha}$, $\boldsymbol{\beta}$, \mathbf{T} are of infinite dimension. T-matrix algorithms truncate these matrices with finite values N and M such that the residual error is below the

machine precision or acceptable levels. Here N represents the number of harmonics used to expand the fields at the scattering origin and M represents the number of harmonics used to expand the fields in the objects' local coordinate systems. Thus, the T-matrix is of size $M \times M$, $\beta_{i,0}$ is of size $M \times N$ and $\alpha_{i,n+1}$ is of size $M \times M$. The parameters N and M are related to the distance of scatterers from the scattering origin and the radii of the scatterers, respectively. As the distances between scatterers and the scattering origin increase, N needs to be increased, and as the radii of scatterers increase, M needs to be increased [15].

2.2 Multiple Signal Classification (MUSIC) Algorithm

The MUSIC algorithm is one of the most thoroughly studied and best understood subspace based direction finding methods. It was originally developed by Schmidt [48] in 1979. The performance improvement of MUSIC was so significant that it became an alternative to most existing estimators, e.g. classical, and MVDR (Minimum Variance Distortionless Response) beamformers. Later on, Stoica et al. [49, 61] derived Cramer-Rao bound for the MUSIC algorithm and investigated the relationship between MUSIC and maximum likelihood (ML) estimators.

Like all other direction finding techniques, MUSIC assumes that the sources are located infinitely far away such that the wavefronts at the receiver array are planar (Fig. 2.2). Based on this assumption, MUSIC determines the angle at which a plane wave is incident on the sensor array. Usually a uniformly spaced, N -element linear array samples M distinct plane

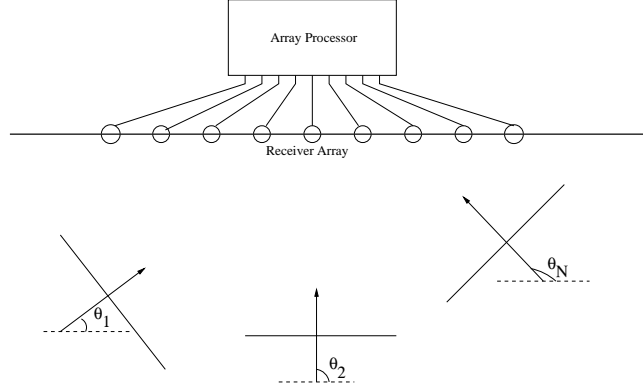


Figure 2.2: Array processing when the sources are infinitely far away from the sensor array waves ($M < N$) and the measured data at the sensor outputs are ²:

$$\mathbf{y} = \mathbf{A}\mathbf{x} + \mathbf{n}, \quad (2.10)$$

where $\mathbf{A} = [\mathbf{a}(\theta_1), \mathbf{a}(\theta_2), \dots, \mathbf{a}(\theta_M)]$ with $\mathbf{a}(\theta_m) = [e^{-jkd \cos \theta_m} \quad e^{-j2kd \cos \theta_m} \quad \dots \quad e^{-jNkd \cos \theta_m}]^T$, d is the distance between consecutive receivers, k is the wave number in the medium of propagation, \mathbf{x} is $M \times 1$ vector comprised of 1's, and \mathbf{n} is spatially and temporally white Gaussian noise.

The experiment as represented by the data model in (2.10) is repeated many times in order to determine the statistics of \mathbf{y} . In particular, if L experiments are performed, then the maximum likelihood estimate of the spatial autocovariance matrix \mathbf{R} is given by:

$$\hat{\mathbf{R}} = \frac{1}{L} \sum_{l=1}^L \mathbf{y}_l \mathbf{y}_l^H \quad (2.11)$$

where \mathbf{y}_l is the data measured at the l th experiment, and superscript H denotes the conjugate transpose. The MUSIC algorithm is based on eigenspace decomposition of the spatial

²The time factor of $e^{j\omega t}$ is suppressed

autocovariance matrix $\hat{\mathbf{R}}$, into the signal and noise subspaces. Thus, we can write $\hat{\mathbf{R}}$ as [28]:

$$\hat{\mathbf{R}} = \hat{\mathbf{U}}_s \hat{\mathbf{\Lambda}}_s \hat{\mathbf{U}}_s^H + \hat{\mathbf{U}}_n [\hat{\sigma}^2 \mathbf{I}] \hat{\mathbf{U}}_n^H \quad (2.12)$$

where $\hat{\mathbf{U}}_s$ is the estimated signal subspace matrix and contains the M “signal eigenvectors”, and $\hat{\mathbf{U}}_n$ is the estimated noise subspace matrix and contains $N - M$ noise eigenvectors of multiple noise eigenvalue $\hat{\sigma}^2$. The projection operator onto the noise subspace is defined as [28]:

$$\hat{\mathbf{\Pi}}_n = \hat{\mathbf{U}}_n \hat{\mathbf{U}}_n^H. \quad (2.13)$$

The basic idea behind the MUSIC algorithm is that the reciprocal of the “distance” between the estimated noise subspace and the true noise subspace has sharp peaks around the DOAs. Thus, if one plots this quantity versus all possible angles, estimates of DOAs can be determined by the maxima of the angular spectrum. The spatial spectrum of the MUSIC algorithm is, then, given by [28]:

$$P_{MUSIC}(\theta) = \frac{\mathbf{a}(\theta)^H \mathbf{a}(\theta)}{\mathbf{a}(\theta)^H \hat{\mathbf{\Pi}}_n \mathbf{a}(\theta)} \quad (2.14)$$

where $\mathbf{a}(\theta) = [e^{-jkd \cos \theta} \quad e^{-j2kd \cos \theta} \quad \dots \quad e^{-jNkd \cos \theta}]^T$ is the direction vector.

It is important to realize that the conventional use of MUSIC implicitly assumes infinitely distant radiators so that the scattered field has planar wavefronts at the sensor array. Thus, the elements of the direction vector $\mathbf{a}(\theta)$ in (2.14) are complex exponentials indicative of plane wave signals. However in subsurface detection applications, the receivers are in the near-field region of the radiating sources, resulting in non-planar wavefronts, Fig. 2.3. Therefore, in order to use the array processing techniques in subsurface detection either the direction

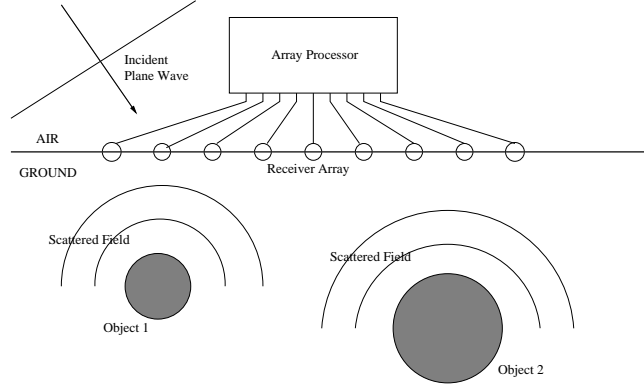


Figure 2.3: Array processing problem geometry

vector $\mathbf{a}(\theta)$ in (2.14) should be filled with non-planar waveforms as in Chapter 5, or the problem with non-planar wavefronts should be circumvented as in Chapter 4. Both these approaches reconfigure the plane wave MUSIC such that the target localization problem becomes determining not only the DOA, but also the range of the target from a point on the array.

Chapter 3

Forward Scattering Model

In this chapter, we will present our contributions to the forward scattering model, the recursive T-matrix algorithm. First, an alternative tessellation scheme for conducting scatterers is introduced to further reduce the complexity of the algorithm, which makes it useful for cases when both dielectric and metallic scatterers exist in the same medium. Then, it is demonstrated that recursive T-matrix algorithm, originally used for calculating scattered fields at the far zone, cannot be directly used for near field scattering problems. The scattering origin has to be carefully selected to minimize the number of harmonics used in the field expansions and, at the same time it should not violate the harmonic expansion given in (2.7). Given the scatterer and receiver geometry, we present the formula to determine the “optimum” scattering origin which minimizes the number translation harmonics, thus minimizing the computational cost. It is also shown that the “optimum” scattering origin creates a convergence problem in the addition theorem [62] identities used in the recursive

T-matrix algorithm. With the modification introduced in this section, the convergence problem is circumvented so that the recursive algorithm can be used with near field measurement geometries of Fig. 2.1. It is important to be able to calculate the scattered field in the near field, since for most shallow subsurface detection problems like mine detection, the scattered field is observed in the near field.

3.1 An Alternative Tessellation for Conducting Scatterers for Recursive T-matrix Algorithms

Traditionally, the recursive T-matrix algorithm has been applied in one of two manners. In the case of dielectric scatterers, the whole object was decomposed into small cylinders, low order harmonic expansions were used to represent the fields from each object, and the recursive algorithm was used to solve the scattering problem [14, 15, 25, 33]. For metallic objects, the equivalence theorem was used to decompose the surface of the scatterer into small strips, moment methods were then employed to find the individual T-matrices for each strip, and the same T-matrix recursions were used to solve the overall scattering problem [24, 26, 27, 42]. By combining these two approaches, it is possible to calculate the scattered field from a collection of both metallic and dielectric objects. For subsurface detection problems, the ability to calculate the scattered field from both metallic and dielectric objects is important. Typical examples may involve calculation of the scattered fields from metallic and dielectric mines buried side by side, or a mine that is comprised of both metallic and

dielectric parts. Thus, we attempt to further simplify the use of the recursive T-matrix algorithm with conducting objects by eliminating the need to use MoM to find the individual T matrices. Since all scatterers are finely tessellated, this technique can be used to find the scattered fields not only from simple shapes but also from more complex shapes at the expense of increased computation time.

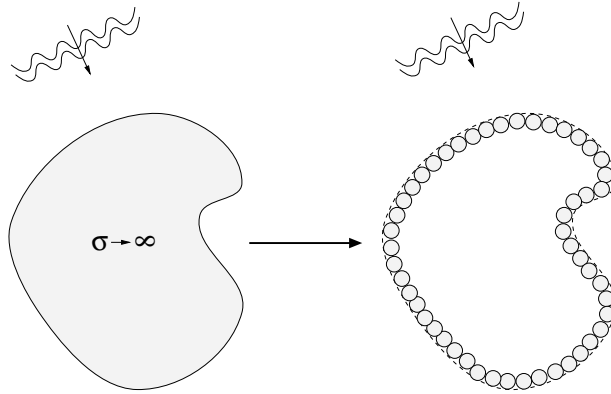


Figure 3.1: Tessellation of metallic cylinders along their perimeters

In this part of the research, we have demonstrated that based on the equivalence theorem, the recursive T-matrix algorithm given in (2.8) and (2.9) can be used to calculate the scattered fields from metallic objects by placing small metallic cylinders on their perimeter as depicted in Fig.3.1. We have shown that [16] one may make use of tessellation with cylinders and still obtain highly accurate solutions. In particular, by using cylinders, the need to use MoM to find individual T matrices is eliminated since one may employ the closed-form harmonic expansion method to find the individual T matrices [60] of scatterers. Even though the examples in the next section depict the scattering from only conducting materials, this tessellation approach can also be used when both metallic and dielectric scatterers

are present in the same medium as shown in Section 3.2.4.

3.1.1 Numerical Results

We now verify that replacing metallic objects with small metallic cylinders along their perimeters actually produces the results reported in the literature or results obtained analytically. First we define the terms used in this section. The normalized scattering field pattern is defined as:

$$F(\phi) = 10 \log_{10} \left\{ \lim_{r \rightarrow \infty} 2\pi r \frac{|\psi^{sca}(\underline{r})|^2}{\max\{|\psi^{sca}(\underline{r})|^2\}} \right\}. \quad (3.1)$$

Normalized power density, or the “gain”, is defined as:

$$G_E(\phi) = \lim_{r \rightarrow \infty} \frac{|\psi^{sca}(\underline{r})|^2}{\frac{1}{2\pi} \int_0^{2\pi} |\psi^{sca}(\underline{r})|^2 d\phi}. \quad (3.2)$$

In all examples the cylinders are embedded in free space with an E_z polarized plane wave incident on them. The first example is the scattering from a single circular cylinder of radius 0.8λ ($ka = 5$). As seen in Fig. 3.2(a), the cylinder is approximated by 60 smaller cylinders along its circumference which corresponds to a sampling 12 cylinders per wavelength. The normalized scattering field pattern, $F(\phi)$, obtained from the recursive algorithm is plotted against the analytical solution in Fig. 3.2(b). The second example is the scattering from two circular cylinders with radii of 0.8λ ($ka = 5$) and separated by a distance 2.55λ ($kd = 16$). As in previous example, each cylinder is approximated by 60 small metallic cylinders with 12 cylinders per wavelength. Fig. 3.3(a) shows the scattering geometry and Fig. 3.3(b) compares the normalized scattering patterns obtained using the recursive T-matrix algorithm with

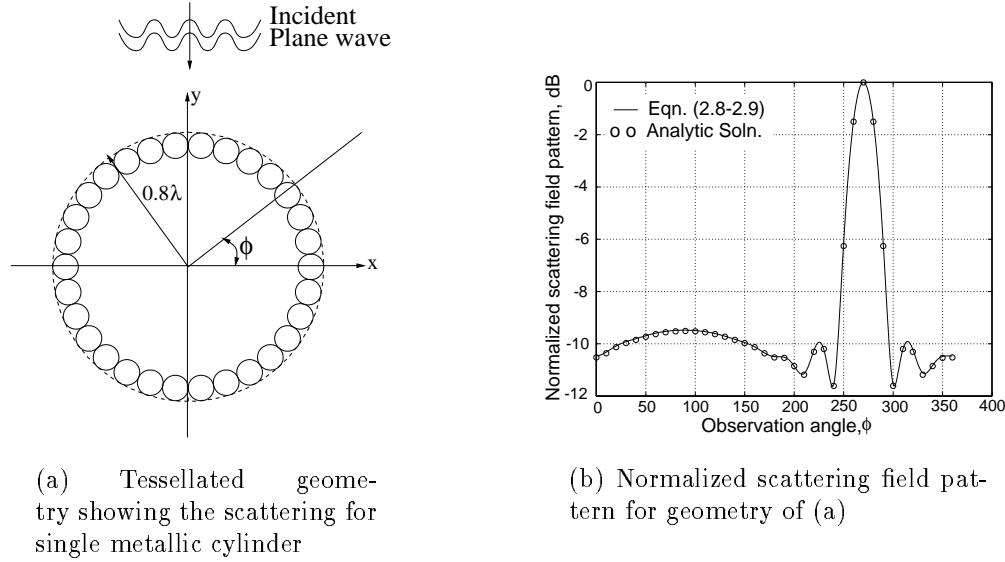
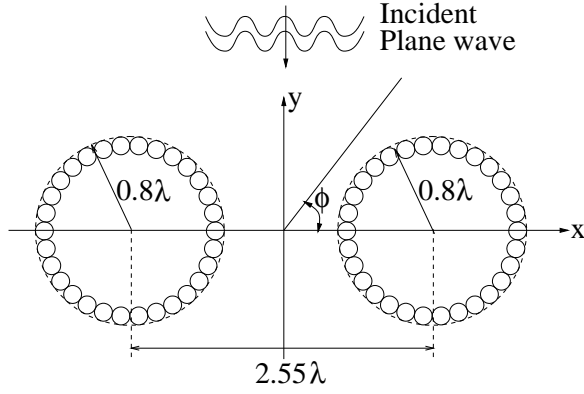
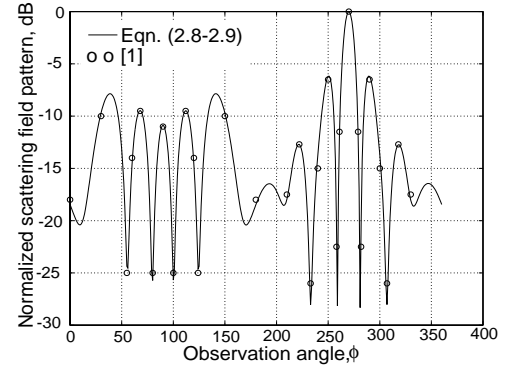


Figure 3.2: Comparison of normalized scattering field pattern calculated using the recursive T-matrix algorithm with the analytically calculated one.

those given in [63]. The last example shows the normalized power densities for a slanted rectangular cylinder for two different sizes. The geometry is shown in Fig. 3.4(a) and the far field power densities, $G_E(\phi)$, for $ka = 3$ and $ka = 5$ ($a = 0.48\lambda$ and $a = 0.8\lambda$, both with $a = 2b$) are depicted in Fig. 3.4(b). For both cases, the perimeter is sampled at approximately 13 cylinders per wavelength. In this figure, the scattering patterns are compared with the results reported in [64]. As these plots have shown, the scattered fields from metallic objects can be found by replacing these objects with smaller cylinders along the perimeter and then using the recursive T-matrix algorithm given by (2.8) and (2.9). All examples here show the scattering from only conducting materials. The dashed curve Fig. 3.8 in Section 3.2.4 depicts an example where both metallic and dielectric scatterers are present in the same medium, and the metallic scatterer is tessellated with small cylinders along its circumference and the

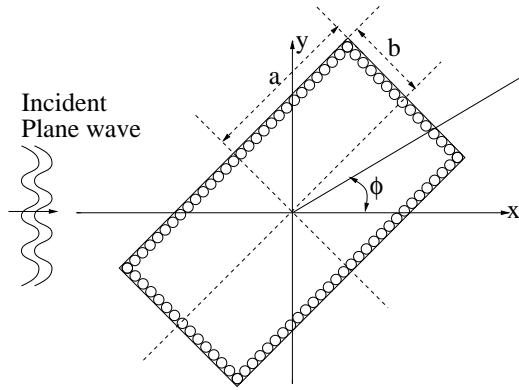


(a) Tessellated geometry showing the scattering for two metallic cylinders

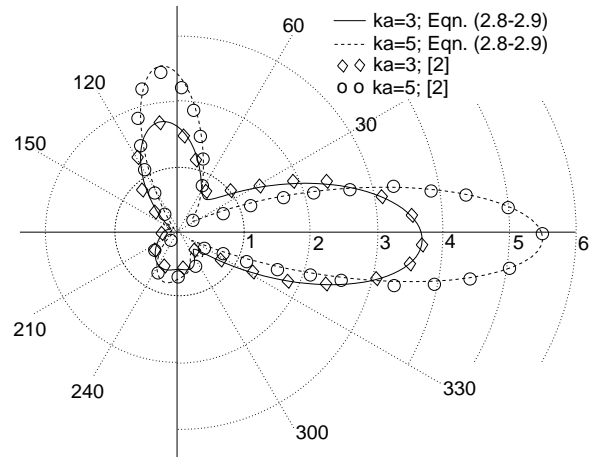


(b) Normalized scattering field pattern for geometry of (a)

Figure 3.3: Comparison of normalized scattering field pattern calculated using the recursive T-matrix algorithm with [63].



(a) Tessellated geometry showing the scattering for 45° slanted metallic rectangle



(b) Polar plot showing the normalized power density vs. ϕ for geometry of (a)

Figure 3.4: Comparison of normalized power density calculated using the recursive T-matrix algorithm with [64].

dielectric scatterer is tessellated with small cylinders over its cross-section.

3.1.2 Summary

We have presented a new application of the recursive T-matrix algorithm to calculate the scattered field from a single or multiple metallic cylinders of arbitrary shapes. Using the equivalence theorem each metallic object is replaced with small metallic cylinders along its perimeter, then scattered fields are calculated using the recursive T-matrix algorithm. Results are verified with those in the literature and analytical calculations.

3.2 A Modified Recursive T-Matrix Algorithm for Near Field Scattering

This part of the research was motivated by the desire to obtain a fast, accurate forward modeling code for ground penetrating radar type geometries illustrated in Fig. 2.1. As discussed in Chapter 1 this application requires the computation of near field values of scattered field arising from mixtures of dielectric and metallic objects. To effectively handle these requirements, we propose a formulation of the recursive T-matrix algorithm based on the representation of the scattered field from each full object using high order expansions (*i.e.* large M) in the recursions in (2.8) and (2.9).

In principle, this approach supports the computation of scattered fields from arbitrary

collections of dielectric and metallic objects. In fact, we demonstrate that this is true specifically for far-field calculations. Unfortunately, the use of higher order expansions results in an instability in a particular harmonic expansion formula upon which the original recursive T-matrix algorithm is based when near field computations are required. In the remainder of this section, we describe explicitly this difficulty and propose a modified recursion which by-passes this addition formula and results in a stable method for solving the problem of interest.

3.2.1 Determination of Scattering Origin

Unlike most radar applications, in a GPR measurement geometry the scattered field is generally observed in the near or intermediate field. Since the harmonic expansions upon which the recursive T-matrix algorithm is based have validity regions (see eqn.(2.4)), there are certain limitations as to where the scattering origin can be placed relative to the receiver array. In this section, we will briefly discuss how the scattering origin is determined, when the object locations and radii are given for the GPR-type configuration in Fig. 2.1. The triplet $(x_i, y_i; a_i)$ represents x and y coordinates of the center and radius of the i th circular object relative to the global origin O_g and L is the number of objects buried under the receiver array.

Because of the requirements on the loci of observation points imposed by (2.4) for single objects and (2.7) for multiple objects, the scattering origin (x_s, y_s) relative to O_g must be selected such that there must be at least one circle, centered at (x_s, y_s) , encircling all objects

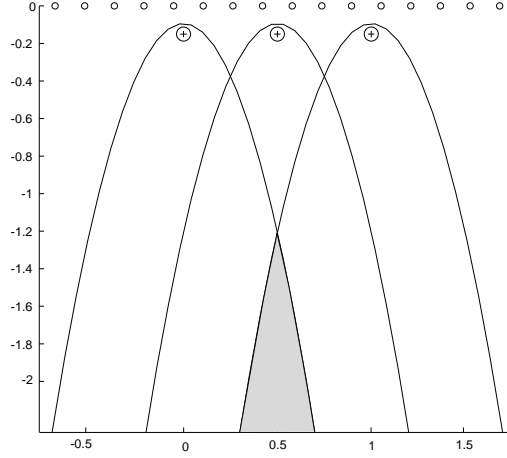


Figure 3.5: Scattering Origin Regions

with no receivers inside it. The dashed circle in Fig. 2.1 depicts such a circle. Assuming a linear receiver array, the condition to choose the scattering coordinate system is:

$$R_c < |y_s| \quad (3.3)$$

where

$$R_c = \max_{i \in \{1, 2, \dots, L\}} \left\{ \sqrt{(x_s - x_i)^2 + (y_s - y_i)^2} + a_i \right\}. \quad (3.4)$$

This condition must be met by individual objects as well as by all objects collectively. Therefore, we can rewrite the condition in (3.3) and (3.4) as the intersection of regions as follows:

$$(x_s, y_s) \in \left\{ (x, y) \mid \bigcap_{i=1}^L \sqrt{(x - x_i)^2 + (y - y_i)^2} < |y| - a_i \right\}. \quad (3.5)$$

In fact, each term under the intersection sign in (3.5) defines the region under an upside-down parabola. Fig. 3.5 depicts the parabolic regions for three objects. Placement of objects in this figure is very typical of a mine detection problem. In this geometry, any point inside the shaded area, representing the intersection of all three parabolic regions, can be selected

as the scattering origin. Ideally, we can place the scattering origin at $y_s \approx -\infty$. This choice of (x_s, y_s) will always satisfy the condition in (3.3). However, the order of harmonics used in the T-matrix algorithm is proportional to the distance between scattering origin and object centers [15], *i.e.* $N \propto kr_i$ where N is the harmonic used for translations to and from the scattering origin, k is the wave number and $i = 1, 2, \dots, L$. Therefore, the optimum scattering origin should be within this shaded area and as close as possible to the objects in order to minimize the harmonics used for translations. As we show in Section 3.2.2, with this choice of (x_s, y_s) , the distances between object centers and the scattering origin can be very close, which causes convergence problems in the addition formulas of T-matrix algorithm. In Section 3.2.3, we describe a modification in the recursive T-matrix algorithm that lets us use the algorithm with optimum choice of scattering origin.

3.2.2 Problems With Higher Order Harmonic Expansions

The convergence problems alluded to earlier can be traced to the fact that equation (2.8) uses the identity

$$\alpha_{p,q} = \beta_{p,0} \alpha_{0,q} \quad \text{if } |\underline{r}_q| \geq |\underline{r}_p| \quad (3.6)$$

which in turn requires the ordering of the objects such that $|\underline{r}_1| \leq |\underline{r}_2| \leq \dots \leq |\underline{r}_L|$. By using definitions of $\alpha_{p,q}$, $\beta_{p,0}$ and $\alpha_{0,q}$ [33,58], we can write the (m, m') th entry, $[\alpha_{p,q}]_{m,m'}$, as:

$$H_{m-m'}^{(2)}(k|\underline{r}_{pq}|)e^{-j(m-m')\phi_{pq}} = \lim_{N \rightarrow \infty} \sum_{n=-N}^N J_{m-n}(k|\underline{r}_p|)e^{-j(m-n)(\phi_p+\pi)} H_{n-m'}^{(2)}(k|\underline{r}_q|)e^{-j(n-m')\phi_q} \quad (3.7)$$

where $\underline{r}_{pq} = |\underline{r}_{pq}|e^{-j\phi_{pq}} = \underline{r}_q - \underline{r}_p$ and $\underline{r}_i = |\underline{r}_i|e^{-j\phi_i}$, $i = p, q$. This truncated sum does not converge if $\underline{r}_q = \underline{r}_p + \underline{\delta}$ where $|\underline{\delta}|$ is small as compared to $|\underline{r}_p|$ and $|\underline{r}_q|$, and if $m - m'$ is a large number ($-M \leq m \leq M$ and $-M \leq m' \leq M$.) Fig. 3.6 shows the convergence of the series in (3.7) for the corner entries of (3.6) for $M = 5$, *i.e.* $\max\{m - m'\} = 10$. Here we have three curves, showing the convergence for $\underline{\delta} = 0.1\underline{r}_p$, $\underline{\delta} = 0.25\underline{r}_p$ and $\underline{\delta} = 0.5\underline{r}_p$. $M \geq 5$ and $\underline{\delta} < 0.1\underline{r}_p$ are typical parameter choices for the problems of interest in this research. It is clear from this figure that as the magnitudes of two vectors get closer, the convergence rate slows. Chew et.al. [24] suggested a windowed addition theorem (which is originally developed for H_z polarized scattering) to overcome this problem, but the implementation of this method introduces two new variables to choose in order to set the width and shape of the window. In addition, the implementation of windowed summation introduces errors in the sum for vectors for which the convergence is not a problem.

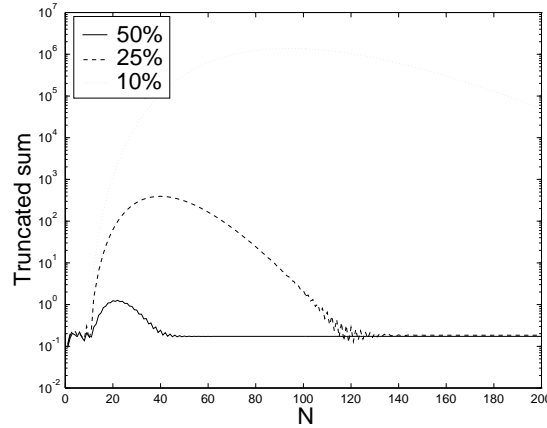


Figure 3.6: Convergence pattern of the truncated sum in the addition formula for $M=5$.

It should be noted that not all valid scattering origins for a given problem give rise to this convergence problem. Indeed, trial and error will quickly demonstrate that, for a given

collection of scatterers, there exist scattering origins where the original T-matrix recursions work just fine. These points are typically far from the scatterers, thereby requiring large N in the recursions, and moreover there does not appear to be an easy *a priori* means to determine whether a chosen origin will or will not give rise to a convergence difficulty. Thus, in the following sections, we introduce a modified recursion which bypasses the convergence issue for all valid scattering origins thereby allowing us to use the closest valid origin (*i.e.* smallest N) to solve the problem.

3.2.3 Modified Recursive T-Matrix Algorithm

The recursion in (2.8) and (2.9) takes place over the quantities $\mathbf{T}_{i(n)}\boldsymbol{\beta}_{i,0}$, and we have determined that the convergence problem stems from (3.6). Therefore, to eliminate the need to use this identity, we go one step back in the derivation of the recursion formulas, and write (2.8) as [15, eq.7-8]:

$$\mathbf{T}_{n+1(n+1)}\boldsymbol{\beta}_{n+1,0} = \left[\mathbf{I} - \mathbf{T}_{n+1(1)} \sum_{i=1}^n \boldsymbol{\alpha}_{n+1,i} \mathbf{T}_{i(n)} \boldsymbol{\alpha}_{i,n+1} \right]^{-1} \mathbf{T}_{n+1(1)} \left[\boldsymbol{\beta}_{n+1,0} + \sum_{i=1}^n \boldsymbol{\alpha}_{n+1,i} \mathbf{T}_{i(n)} \boldsymbol{\beta}_{i,0} \right] \quad (3.8)$$

and (2.9) as:

$$\mathbf{T}_{i(n+1)}\boldsymbol{\beta}_{i,0} = \mathbf{T}_{i(n)} \left[\boldsymbol{\beta}_{i,0} + \boldsymbol{\alpha}_{i,n+1} \mathbf{T}_{n+1(n+1)} \boldsymbol{\beta}_{n+1,0} \right] \quad (3.9)$$

without using (3.6). Since (3.6) is not used in (3.8) and (3.9) we can base a new recursion on these two equations and the identity:

$$\boldsymbol{\beta}_{i,0} \boldsymbol{\beta}_{0,i} = \mathbf{I} \quad (3.10)$$

where $\beta_{i,0}$ is $M \times N$, $\beta_{0,i}$ is $N \times M$, and (3.10) holds as long as $N > M$ which is always true as long as objects are not overlapping. By using (3.8), (3.9) and (3.10) the modified recursion equations can be written as:

$$\mathbf{T}_{n+1(n+1)}\beta_{n+1,0} = \left[\mathbf{I} - \mathbf{T}_{n+1(1)} \sum_{i=1}^n \alpha_{n+1,i} \mathbf{T}_{i(n)} \beta_{i,0} \beta_{0,i} \alpha_{i,n+1} \right]^{-1} \mathbf{T}_{n+1(1)} \left[\beta_{n+1,0} + \sum_{i=1}^n \alpha_{n+1,i} \mathbf{T}_{i(n)} \beta_{i,0} \right] \quad (3.11)$$

and

$$\mathbf{T}_{i(n+1)}\beta_{i,0} = \mathbf{T}_{i(n)}\beta_{i,0} + \mathbf{T}_{i(n)}\beta_{i,0}\beta_{0,i}\alpha_{i,n+1}\mathbf{T}_{n+1(n+1)}\beta_{n+1,0}. \quad (3.12)$$

Note that the recursion is still over the same block, $\mathbf{T}_{i(n)}\beta_{i,0}$, but since (3.6) is eliminated these new recursion equations do not suffer from convergence problems.

As reported in [15] the original recursive T-matrix algorithm has a complexity of $O(M^2 N)$ per recursion. It is easily shown that the modified algorithm also has a complexity of $O(M^2 N)$ per recursion with a slightly larger constant in front of $M^2 N$ resulting from extra multiplications to obtain $\mathbf{T}_{i(n)}$ from $\mathbf{T}_{i(n)}\beta_{i,0}$. To calculate the scattered field from L objects, $L(L-1)/2$ recursions are required. Therefore, the overall complexity of both the recursive and modified recursive algorithm is $O(L^2 M^2 N)$.

3.2.4 Numerical Results

We now verify the modified algorithm against published results and then provide a collection of examples that are relevant for near-field applications. As most previously published results for scattering problems involve far-field computations, in verifying our approach we also demonstrate its ability to handle far-zone calculations. Where appropriate, we compare the

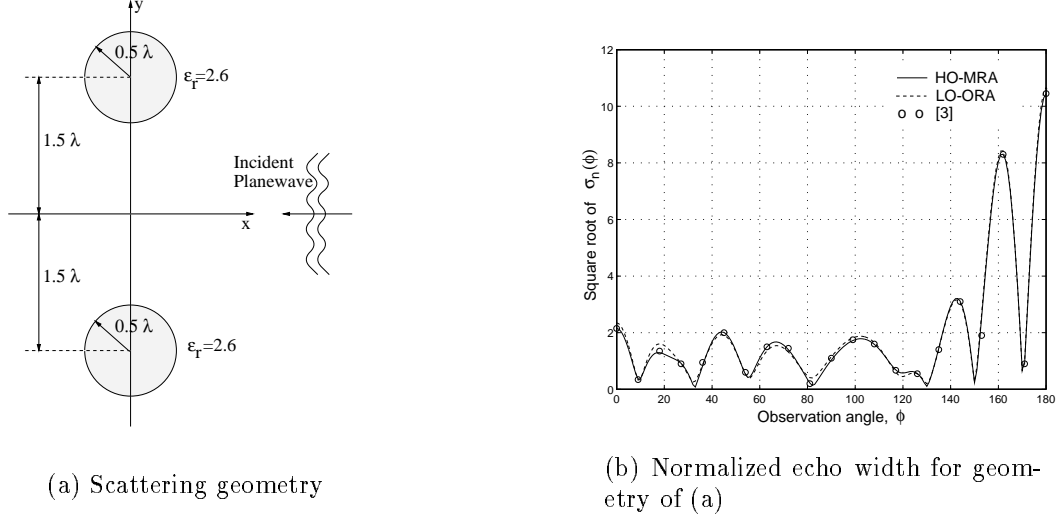


Figure 3.7: Comparison of echo width with [65] for two equal dielectric cylinders

computational cost of our higher-order, modified recursive algorithm (HO-MRA) against two alternate T-matrix approaches. First, we implement the lower-order, original recursive algorithm (LO-ORA) of [15] for near and far-field problems. For far-zone problems with mixed dielectric and metallic scatterers, we consider high-order (*i.e.*, large M) forms of the original recursions (HO-ORA) (2.8) and (2.9), where, because of the far field assumption, the instability problem is not an issue.

Before we proceed, we define the normalized echo width as [65]:

$$\sigma_n(\phi) = \lim_{r \rightarrow \infty} \frac{2\pi r}{\lambda} \left| \frac{\psi^{sca}(\underline{r})}{\psi^{inc}(\underline{r})} \right|^2, \quad (3.13)$$

where λ is the wavelength in the medium of propagation.

We first calculated the scattered field due to two dielectric cylinders placed in free space, each with relative dielectric constant of 2.6, and radius of 0.5λ . The distance between the

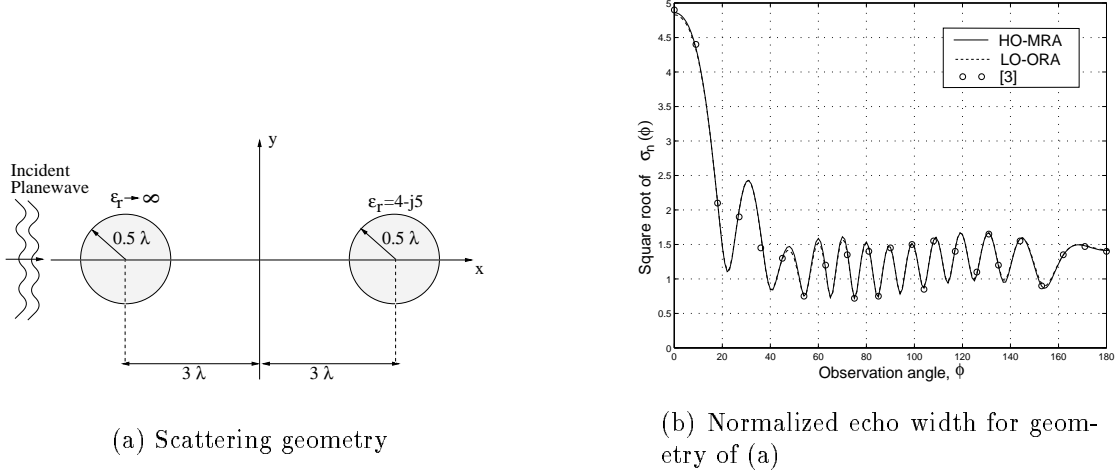


Figure 3.8: Comparison of echo width with [65] for two cylinders, one lossy dielectric and one metallic

cylinders is 3λ (Fig. 3.7(a).) An E_z polarized plane wave is incident from 0° . Fig. 3.7(b) shows the square root of the echo width calculated using the HO-MRA of this section (solid line), the LO-ORA of [15] (dashed line) and results in [65] (circles). Since HO-ORA produced essentially the same fields as HO-MRA, the results of this approach is not shown here. Fig. 3.8(b) shows a similar comparison for a mixed object case depicted in Fig. 3.8(a), *i.e.*, one cylinder is metallic and the other is lossy dielectric with $\epsilon_r = 4 - j5$. In this example, to calculate the scattered field using LO-ORA, the conducting scatterers have to be tessellated along their perimeters. In [26,27], Gürel et al. use metallic strips and patches, whose individual T matrices are found via MoM, with LO-ORA. Adapting their approach, one can tessellate conducting scatterers with flat or curved metallic strips in the examples. Alternatively, [16] uses small sub-cylinders along the perimeter of conducting scatterers for tessellation. We have used the second approach with LO-ORA to calculate the scattered

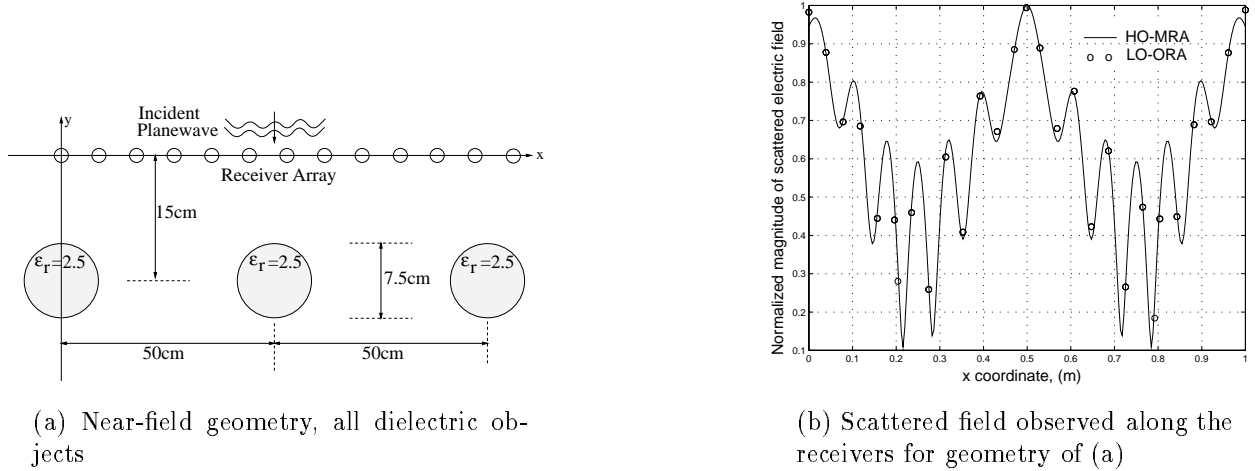
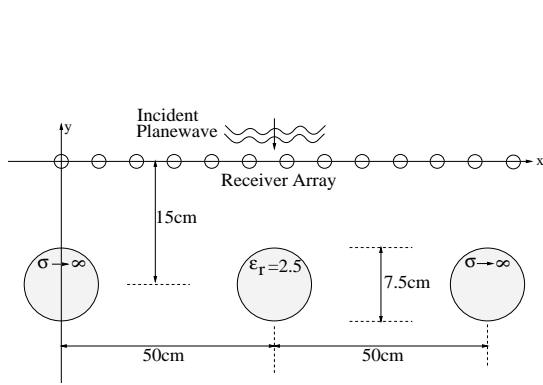


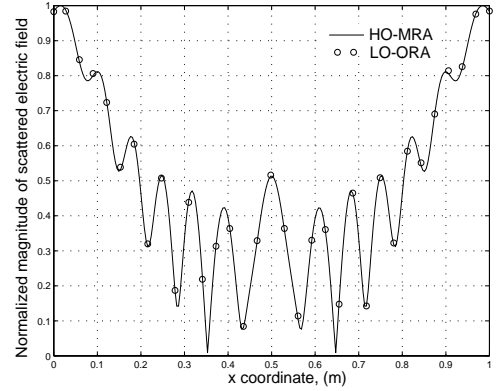
Figure 3.9: Scattered electric fields from 3 dielectric objects

field since it does not require the use of MoM. As in the previous example, the square root of the echo width obtained using the modified algorithm, LO-ORA and that reported in [65] are very close.

Now, we present scattering examples that are representative of near-field applications. All objects are assumed to lie in a homogeneous, lossy background ($\epsilon_b = 6\epsilon_0$, $\sigma_b = 5 \times 10^{-2} S/m$); the operating frequency is 1 GHz and a plane wave is incident from 90° , see Fig. 3.9(a). We first find the scattered field from 3 dielectric objects with diameters 7.5 cm as shown in Fig. 3.9(a). All objects have a relative permittivity of 2.5. The scattering origin has to be placed far away from the receiver array ($x_s = 0.5$ m, $y_s = -1.25$ m), because the objects are close to the receivers, which in turn requires a large value, 120, for N . For this case, we calculated the scattered field using both the LO-ORA and HO-MRA defined in Section 2.1.2 and Section 3.2.3, respectively. Fig. 3.9(b) shows the normalized scattered fields observed



(a) Near-field geometry, mixed objects



(b) Scattered field observed along the receivers for geometry of (a)

Figure 3.10: Scattered electric field from 2 metallic and a dielectric objects

along the receiver array using the HO-MRA (solid line) and the LO-ORA (circles). It is clear from this figure that both approaches yield very similar fields.

The second near-field example depicts a mixed object case since the objects at the sides are metallic and the object at the center is dielectric with a relative dielectric constant of 2.5, Fig. 3.10(a). The locations of the objects are the same as the previous example, and the scattering origin is still at $(x_s = 0.5 \text{ m}, y_s = -1.25 \text{ m})$. As a result $N = 120$, and since the object radii are relatively small $M = 12$. The normalized scattered field observed along the receiver array for mixed object case is shown in Fig.3.10(b). As in the far-field example, for LO-ORA implementation, metallic objects are tessellated using the approach in [16].

We now compare computational costs of the HO-MRA, LO-ORA, and HO-ORA. To ensure a fair comparison, whenever a tessellation is required, we set the density of sub-scatterers to be close to that used in [15]. Performance of each approach is measured by the

	HO-MRA	LO-ORA	HO-ORA
Fig. 3.7	0.6	1150	0.64
Fig. 3.8	1.9	766	1.9
Fig. 3.9	18.94	857	c/p
Fig. 3.10	18.95	393	c/p

Table 3.1: Cost comparison for recursive algorithms. All numbers in FLOPS/ 10^6 , and c/p means convergence problems in near field calculations

	HO-MRA	LO-ORA	HO-ORA
Fig. 3.7	L=2,M=7,N=23 (x_s, y_s)=(0,0)	L=398,M=1,N=23 (x_s, y_s)=(0,0)	L=2,M=7,N=28 (x_s, y_s)=(0,0.3 λ)
Fig. 3.8	L=2,M=10,N=40 (x_s, y_s)=(0,0)	L=249,M=1,N=40 (x_s, y_s)=(0,0)	L=2,M=10,N=44 (x_s, y_s)=(0.3 λ ,0)
Fig. 3.9	L=3,M=12,N=120 (x_s, y_s)=(0.5,-1.25)	L=93,M=2,N=120 (x_s, y_s)=(0.5,-1.25)	c/p
Fig. 3.10	L=3,M=12,N=120 (x_s, y_s)=(0.5,-1.25)	L=63,M=2,N=120 (x_s, y_s)=(0.5,-1.25)	c/p

Table 3.2: Parameter list for Table 3.1

floating point operations (flops) required to calculate the scattered field. Table 3.1 shows the flop count of all three recursive T-matrix algorithms that can be used to find the scattered fields from multiple, spatially separated cylinders. Table 3.2 shows the number of scatterers L , number of harmonics M , N and the location of the scattering origin (x_s, y_s) used in these examples.

The first two rows of Tables 3.1 and 3.2 correspond to examples from the two-dimensional scattering literature. For these cases, all observation points are in the far field so that the convergence problem alluded to earlier is not an issue. As seen from Table 3.1 LO-ORA's flop count is quite large as compared to HO-MRA and HO-ORA. The reason behind this large cost is that numerous sub-scatterers are required for each cylinder. One would expect the computational complexity of HO-ORA to be less than that of HO-MRA since the latter needs extra multiplications to obtain $\mathbf{T}_{i(n)}$ from $\mathbf{T}_{i(n)}\boldsymbol{\beta}_{i,0}$. However, since the scattering origin is placed at a different location in HO-ORA to prevent the convergence problem, the number of harmonics N has to be increased accordingly, which increases the flops required for HO-ORA considerably.

The last two rows of Table 3.1 show the flops needed to find the scattered field for near-field examples and Table 3.2 shows the number of scatterers, harmonics and the locus of the scattering origin used in these examples. Unlike previous examples, these geometries require measuring the scattered field in the near field with a linear receiver array, which restricts the regions where the scattering origin can be placed. As we have shown in Section 3.2, the choice of optimum scattering origin results in convergence problems in HO-ORA for

near-field geometries. Alternatively, LO-ORA can be used in these problems, however, one has to spend approximately 45 and 21 times more flops than it is needed for HO-MRA for examples in Fig. 3.9 and Fig. 3.10, respectively.

3.2.5 Summary

We have presented an efficient, stable, recursive T-matrix algorithm to calculate the scattered field from a heterogeneous collection of spatially separated objects. The algorithm is based on the use of higher-order multipole expansions than those typically employed in recursive T-matrix techniques. The use of these expansions introduces instability in the recursions developed in [15, 33] specifically in the case of near-field computations. By modifying the original recursive algorithm to avoid these instabilities we arrive at a flexible and efficient forward solver appropriate for a variety of scattering calculations. The algorithm can be applied when the objects are dielectric, metallic, or a mixture of both. We verify this method for cases where the scatterers are electrically small (fraction of a wavelength) or relatively large ($1-2 \lambda$). While developed for near-field calculation, this approach is applicable for far-field problems as well. Finally, we demonstrate that the computational complexity of this approach compares favorably with comparable recursive algorithms.

Chapter 4

Detection and Localization: Subarray Processing

In this chapter, we will present the Subarray Processing (SAP) approach for detection and localization of subsurface objects. In Section 4.1 we will define the problem and motivation behind the algorithm. In Section 4.2, we present the details of the algorithm, i.e. the partition of the array and DOA determination, crossing analysis and clustering, target extraction, and frequency diversity. We continue this chapter by presenting the numerical examples in Section 4.4, and conclude with a summary in Section 4.5.

4.1 Introduction

The localization problem of particular interest is shown by the measurement geometry in Fig. 2.3. A plane wave illuminates the region of interest assumed to be a homogeneous,

possibly lossy medium containing one or more targets located in the near field of an array of receivers. The array structure of the receivers in Fig. 2.3 implies that the high-resolution array processing methods [28, 29] would be appropriate for the near-field localization problem. Adapting such methods to the problem of interest here presents a collection of interesting challenges. First, these array processing techniques typically assume that the sources are infinitely far away so that the waveform received on the array is planar. For our problem, since the objects are located relatively close to the receiver array, this key assumption is not valid. Second, for such near-field objects both range as well as the direction of arrival has to be determined in order to localize the object. Finally, a problem common to both the near-field and far-field array processing algorithms is that the number of incident waveforms/targets is not known *a priori*.

To deal with the non-planar nature of the wavefronts over the array in this chapter, we partition the receiver array into sub-arrays, such that the scattered field is locally planar at each sub-array, i.e. the scatterer is in the far-field of the sub-array. Then, using high resolution array processing techniques, each sub-array identifies a single direction of arrival (DOA) corresponding to the most dominant scatterer in the vicinity of that sub-array. The localization of the objects in terms of their ranges and bearings is achieved by triangulating the directions of arrival from all subarrays which in turn results in a crossing pattern of DOA intersections. Examination of typical crossing structures reveals that there are two distinct patterns where the crossings are either dense or sparse. Dense crossing regions clearly indicate object locations and are distinguished from “background” regions where the

crossings are sparse. The problem of object detection and localization then is reduced to the processing of the crossings obtained from our triangulation procedure.

For this purpose, we introduce a simple yet accurate stochastic model describing the spatial distribution of DOA crossings. Such modeling is warranted for two reasons. First, due to the noise in the data, the DOA intersection points are inherently randomly distributed in the plane. Second, such modeling forms a solid basis for algorithm development and quantitative performance analysis in the form of detection and false alarm rates.

In this work, we model the two classes of crossings (dense vs. sparse) using a pair of spatial Poisson distributions [66]. The Poisson model in the target region has a large rate parameter while that of the background region is considerably smaller. Based on these target and background models, we develop a hypothesis testing technique for the joint estimation of the rate parameters and the localization of dense crossing regions which indicate the existence of targets. Simple post-processing of the hypothesis testing results provides both the number of targets and estimates of their locations. Finally, we verify that the Poisson model is in fact a rather accurate description of the spatial distribution of crossings.

We demonstrate the performance of this approach for the detection and localization of multiple mine-like and drum-like targets located in the near field of the receiver array. For mine-like targets relative positions of the objects are changed to see the effect of object geometry on detectability. We show that the detectability improves, and false alarm rate decreases as the objects are located far apart. For drum-like targets, we demonstrate the effect of relative depth as well as relative distance between objects on detectability.

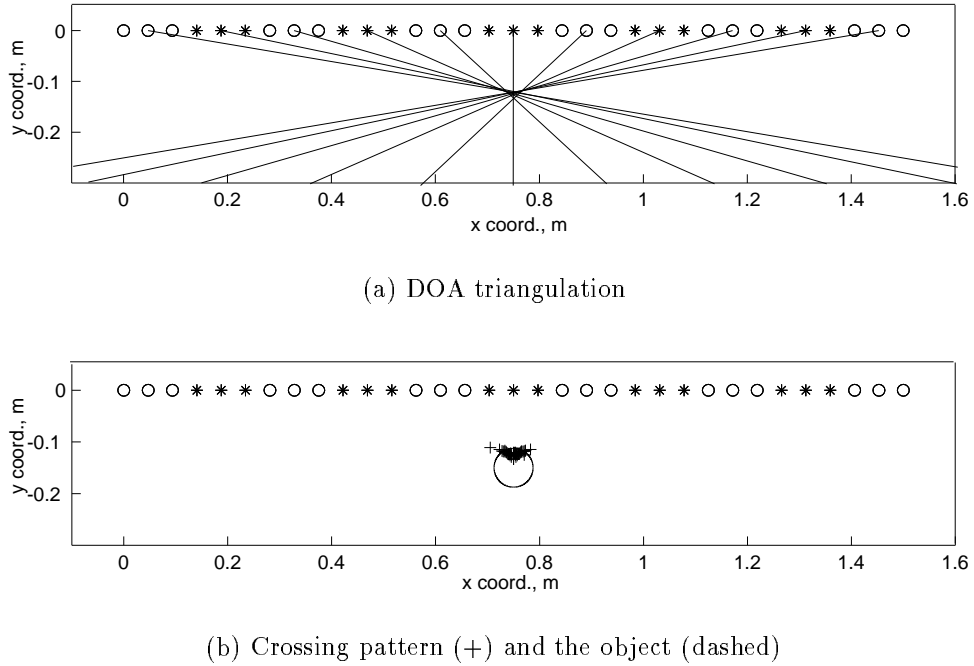


Figure 4.1: Single object localization with SAP: metallic mine-like object in lossy background

4.2 Algorithm

A key element of the work in this thesis is the development of a sub-array processing method for detection of multiple objects in the near field of an array. In Section 4.3, we examine such a technique for detection and localization of single metallic and dielectric objects. As illustrated in Fig. 4.1 (and as is generally the case), the localization problem in Section 4.3 is straightforward since typically all crossings are densely packed within the radius of the object. Therefore, the location of the object can be inferred quite easily. For multiple objects, however, the crossing pattern is quite complicated, since DOAs of different objects create unwanted crossings as shown in Fig. 4.2. The clusters of object crossings are embedded in this unwanted background crossings, and have to be extracted carefully.

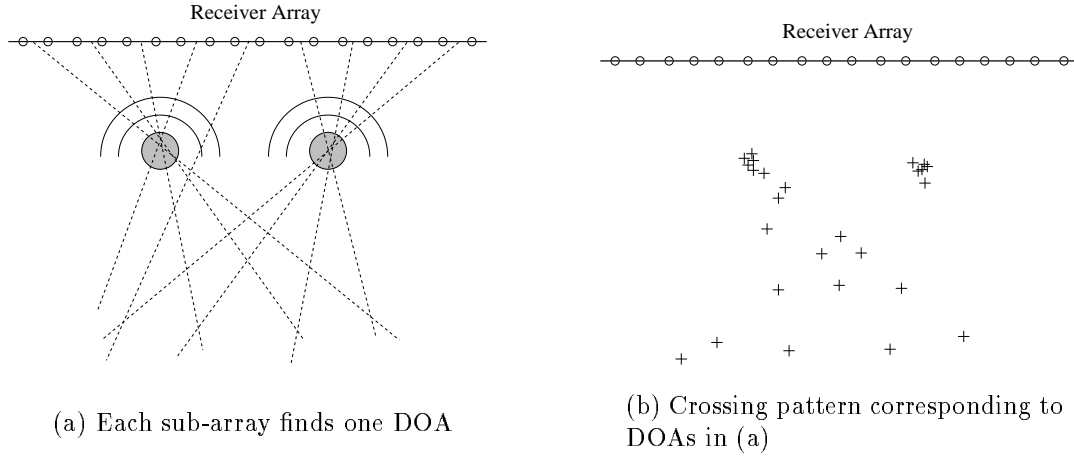


Figure 4.2: Multiple object subarray processing concept: directions of arrivals and crossing pattern

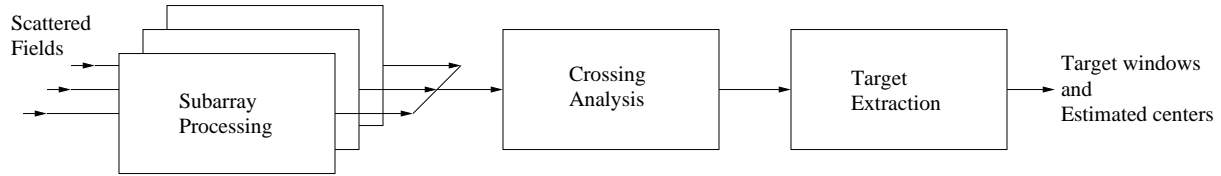


Figure 4.3: Flow chart of the algorithm

Before introducing the details of our approach, we want to briefly describe the algorithm with the help of flow chart in Fig. 4.3. The algorithm proceeds as follows:

1. **Sub-array processing:** At this stage of the algorithm, we partition the receiver array so that the observed scattered field is locally planar at each sub-array. The directions of arrival (DOAs) are found using MUSIC as if planar waves are impinging on the sub-arrays. The criterion for which the impinging waves are locally planar over the subarray aperture is presented in Section 4.2.1. The DOAs are then triangulated to obtain the crossing pattern. This stage of the algorithm is repeated several times for plane waves

at different temporal frequencies to improve performance and resolution. The crossing patterns obtained at different frequencies are overlaid to yield an aggregate crossing pattern which is, then, passed onto the second stage of the algorithm.

2. **Crossing analysis:** In the second stage, the crossing pattern is modeled with two Poisson counting processes, corresponding to target and background regions. After estimating the required rate parameters using the crossing data, a hypothesis testing procedure is employed to determine a set of “window” regions corresponding to areas containing targets.
3. **Target extraction:** At the final stage of the algorithm, the individual detection windows are aggregated into a number of spatially disjoint groups. The total number of groups indicates the estimated number of targets, and average coordinates of centers of all windows in a group indicate the estimated center of the corresponding target.

4.2.1 Sub-array Processing

The direction finding algorithms traditionally assume plane wave incidences and determine the DOA associated with each plane wave. For near-field problems, however, both DOA and the range of the source (in our case scatterer) should be acquired. Here, we describe a sub-array processing (SAP) scheme which only requires one-dimensional search in DOA space of each sub-array. The idea behind the sub-array processing is that if the aperture of the sub-array is small enough, the scattered field impinging upon it can be assumed locally planar. Planar wavefronts are a consequence of scatterers being in the far field of the receiver

array. Therefore, given the subarray span, D , we can determine the distance beyond which the scatterer is in the far field using [67]:

$$\frac{2 D^2}{\lambda}, \quad (4.1)$$

where λ is the wavelength in the medium of propagation. Any source located farther than the limit given in (4.1) is in the far field of the subarray, and thus the wavefields emanating from that position will have approximately planar wavefronts at the subarray aperture. For practical problems, however, the distances between the scatterers and the subarrays are not known. Therefore, the subarray span should be chosen small enough to guarantee that the expected distances to the targets are more than the limit given in (4.1). Once the planar wavefronts are guaranteed at the subarrays, the plane wave MUSIC can be used to find DOAs at each sub-array, and by triangulation, it is possible to localize the scatterers.

When there are $M > 1$ objects in the vicinity of the array (it is assumed that the number of sensors in each subarray is always greater than M), we have two options in terms of how MUSIC is employed:

1. Each sub-array finds M DOAs for all locally planar waves scattered from M objects,
or
2. Each sub-array finds one DOA for the locally planar wave dominant in the total scattered field (Fig. 4.2 shows $M = 2$ case).

Given M objects and S sub-arrays, for each operating frequency the first and second options result in $0.5SM(SM - 1)$ and $0.5S(S - 1)$ crossings, respectively. The first option creates

many unwanted crossings when DOAs belonging to different objects intersect. In addition, we have to know the number of objects under the array to use this option. On the other hand, the second option does not require the knowledge of number of objects, and the scattered fields from targets closer to the sub-arrays, particularly in a lossy medium such as soil, dominate the total scattered field at the sub-arrays. This option may fail to find DOAs for objects for which the scattered fields are at comparable strengths. For some cases, it may also prevent determination of a DOA for a weak scatterer, if there is a strong scatterer nearby. Given all these pros and cons, the latter option seems more practical especially when one wants to avoid estimating the number of scatterers first, and is used in the remainder of this chapter.

Once one DOA at each sub-array is determined, all DOAs are triangulated to estimate the target locations. Fig. 4.2(a) shows the triangulation of DOAs, and (b) shows the crossings. In contrast to the single object case, for multiple objects, the crossing pattern may get quite complicated since DOAs belonging to different objects also intersect each other to create unwanted crossings. Thus, a second level of processing is required to extract the clusters indicating the estimated object centers.

4.2.2 Crossing Analysis

In this section we present an approach that models the DOA crossings with Poisson point processes. Inspecting Fig. 4.2(b), we see two distinct regions where the density of the crossings are quite different: in the first region (*background region*) the crossings are sparse, and

in the second region (*target region*) the crossings are dense. By exploiting this difference, it is possible to isolate target locations. Hence, we introduce a Poisson model for DOA crossings which has a large rate parameter (intensity) in target regions and a small rate parameter in the background region.

Formally, for a given crossing pattern, we count the number of crossing $Y_j, j = 1, 2, \dots, N_y$, in a window of size $w_x \times w_y$, where N_y is the total number of *non-overlapping* windows, w_x and w_y are the width of the windows in x and y directions, respectively. The windows must be non-overlapping to guarantee the independence of random variables Y_j .

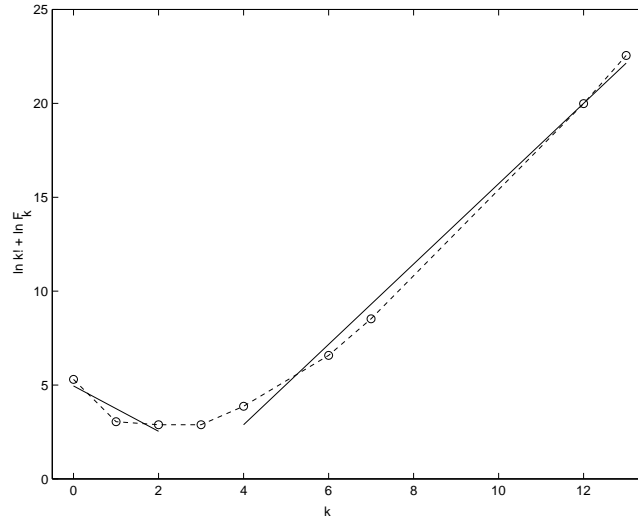


Figure 4.4: Fitness to Poisson model for the example of Fig. 4.6. Solid lines are fitted to data using linear least squares

In order to ensure that Y_j is Poisson distributed, we tested for fitness to Poisson distribution by using the graphical technique presented in [68]. The technique proposes that for each count k observed in Y_j , we plot k versus $(\ln k! + \ln F_k)$ where $F_k = \sum_{j=1}^{N_y} [Y_j = k]$ is the number of data values Y_j equal to k . If the fit to the Poisson model is satisfactory, then the plot should form a straight line with slope approximately $\ln \lambda$, where λ is the rate

parameter of the distribution. When we apply this test to a typical crossing pattern, instead of a straight line, we observed the curve in Fig. 4.4. By examining this curve, we notice that it can be decomposed into two parts, each roughly corresponding to a straight line. The first part is when the crossing count k is small (between 0 and 2), and the second part is when k is large (greater than 3.) It is clear that these two regions correspond to the background process which is expected to have a small count of crossings, and the target process which is expected to have a large count of crossings. Furthermore, using these two approximately linear regions, we can decouple background and target processes by identifying k_b and F_{kb} for the background, and k_t and F_{kt} for the target regions where $k_b = 0, 1, 2$, $k_t = 3, 4, \dots$, $F_{kb} = \sum_{j=1}^{N_y} [Y_j = k_b]$ and $F_{kt} = \sum_{j=1}^{N_y} [Y_j = k_t]$. Then, the rate parameters for the background and the target regions are given by their maximum likelihood estimates [68]:

$$\hat{\lambda}_b = \frac{1}{N_b} \sum_{kb=0}^2 k_b F_{kb}, \quad (4.2)$$

and

$$\hat{\lambda}_t = \frac{1}{N_t} \sum_{kt=3}^{\infty} k_t F_{kt}, \quad (4.3)$$

where $N_b = \sum_{k_b} F_{k_b}$ and $N_t = \sum_{k_t} F_{k_t}$. Having estimated $\hat{\lambda}_b$ and $\hat{\lambda}_t$, the probability mass functions in the background and target regions can be expressed as:

$$f_X(k|\text{Background}, \hat{\lambda}_b) = P\{X = k|\text{Background}, \hat{\lambda}_b\} = \frac{1}{k!} e^{-\hat{\lambda}_b} \hat{\lambda}_b^k \quad (4.4)$$

and

$$f_X(k|\text{Target}, \hat{\lambda}_t) = P\{X = k|\text{Target}, \hat{\lambda}_t\} = \frac{1}{k!} e^{-\hat{\lambda}_t} \hat{\lambda}_t^k. \quad (4.5)$$

To extract crossing clusters, we sweep the region of interest with a test window of size $w_x \times w_y$. It is important that the area of the test window is equal to the area of the non-overlapping windows used in estimating the rate parameters. At each location of the test window, we count the number of crossings T_j , $j = 1, 2, \dots, N_{test}$, where N_{test} is the total number of *overlapping* sweep windows in the region of interest. The number of overlapping test windows N_{test} defines the resolution of detection, and it is greater than N_y . Since we are going to test each T_j one by one, the use of overlapping windows is allowed. The hypothesis test permits us determine whether the test window is over a background region or over a target region. The hypothesis test is then formally written as:

- H_0 : T_j is Poisson distributed with a small rate parameter $\hat{\lambda}_b$,
- H_1 : T_j is Poisson distributed with a large rate parameter $\hat{\lambda}_t$.

Based on this hypothesis test, if H_0 is true, we decide that the window belongs to a background process with a small intensity. However, if H_1 is true, we declare that the window belongs to a target process with a large intensity and call it a detection.

The generalized likelihood ratio for the hypothesis test is formed in terms of the probability mass functions of (4.4) and (4.5) as:

$$\Lambda(T_j) = \frac{f_X(T_j|H_1, \hat{\lambda}_t)}{f_X(T_j|H_0, \hat{\lambda}_b)}$$

The decision is, then, made based on the generalized likelihood ratio test:

$$\ln\{\Lambda(T_j)\} = T_j \stackrel{H_1}{>} K, \tag{4.6}$$

where the decision threshold, K , is found from a specified false alarm rate P_{fa} using (4.7) below. This means that all windows which have K or more crossings in them will be declared as target locations. The probability of false alarm P_{fa} can be written in terms of the decision threshold K and probability mass function of background process in (4.4) as :

$$P_{fa} = \sum_{k=K}^{\infty} f_X(k|H_0, \hat{\lambda}_b). \quad (4.7)$$

Given the decision threshold K , the probability of detection for the Poisson model developed in this section is given by:

$$P_d = \sum_{k=K}^{\infty} f_X(k|H_1, \hat{\lambda}_t). \quad (4.8)$$

It might be argued that since target windows are obtained via thresholding, there would be no need for a Poisson-based model as described in this section. A plain thresholding scheme on DOA crossings would also locate the targets successfully. However, the Poisson model provides a solid groundwork for a detailed statistical analysis. With the model, it is possible to define probabilities of false alarm and detection. Based on these statistical analyses, it is possible to make educated predictions about the performance of the system under different conditions.

4.2.3 Target Extraction

Hypothesis testing with the Poisson model results in detection windows as shown in Fig. 4.6. By looking at this figure, a human operator may conclude the target locations and their numbers. However, we want the detection algorithm to do these decisions and calculations for us automatically. In effect, we want the algorithm to yield the number of targets in

the region of interest and their estimated locations, rather than the intertwined pattern of detection windows.

The pattern of detection windows suggests that the detection windows belonging to the same targets overlap. Therefore, we classify the detection windows so that all overlapping windows form a distinct group. The number of targets is, then, equal to the number of groups and the estimated object centers are obtained by averaging the coordinates of the windows in each group. The grouping algorithm we use, therefore, proceeds as follows. Start with the first window on the list of detection windows and place it in the first group. For each of the other windows, test if they overlap with any window in the k th group for $k = 1, 2, \dots, G_c$, where G_c is the number of currently available groups. If the window overlaps with only one group, add it to that group. If the window overlaps with more than one groups, merge those groups, and reduce the number of current groups G_c accordingly. If the window does not overlap with any windows among G_c groups, then form $(G_c + 1)$ th group with that window and increment G_c . When all detection windows are classified, G_c gives the number of objects, and averaged coordinates of all windows in each group give the estimates of center of the objects they represent.

4.2.4 Frequency Diversity

Frequency diversity is often used in detection applications for two important reasons: to increase the resolution (high frequencies) and to allow radar signals to penetrate deeper into the medium (low frequencies). Therefore, with a wide frequency range, one can ideally get

more resolution in the vicinity of the radar, and more penetration to probe deeper objects. To take advantage of these benefits, we use our sub-array processing algorithm in a multi-frequency scheme. For each frequency the sub-array processing described in Section 4.2.1 is carried out to obtain the DOAs and the crossing pattern. Then, these multiple crossing patterns are overlaid to give an aggregate crossing pattern which is modeled as the Poisson counting processes in Section 4.2.2.

4.3 Single Object Localization Examples

In this section, we will present examples about single object localization using the sub-array processing. The main difference between multiple and single object localization is that for single object case, the DOA crossings tend to cluster in one region. We can obtain the estimated target centers by directly averaging the crossing coordinates. Therefore, there is no need for the crossing analysis with Poisson distribution presented in Section 4.2.2 or the target extraction presented in Section 4.2.3. Frequency diversity may be employed to improve the detection performance. However, since we consider simple detection examples, we will only use 1.0 GHz operating frequency in this section. The scattered field is observed along a 16-element uniform, linear receiver array. We considered three detection scenarios. The first case involves a relatively small metallic object (SM), the second case is a small dielectric object with relative permittivity 2.5 (SD) and the third case is a larger metallic object (LM). The first two cases correspond to mine detection problems where objects are relatively small (7.5 cm in diameter) and buried shallow (the centers are 15cm below the

array). The last case corresponds to waste container detection problem where the object is larger (60cm in diameter) and buried deeper (the center is 120cm below the array). For the SM and SD experiments the sensor array spans a 30cm distance as opposed LM case where it spans 75cm. In all examples in this section, the objects are positioned at the mid-point of the array, and the signal to noise ratio is defined to be:

$$snr = \frac{\mathbf{E}_s^H \mathbf{E}_s}{M\sigma^2},$$

where \mathbf{E}_s is the scattered field measured over M -element receiver array, and σ^2 is the noise variance. The estimation error is defined as:

$$Error = \frac{\sqrt{(\Delta x)^2 + (\Delta y)^2}}{a} \quad (4.9)$$

where Δx and Δy are the difference between true center coordinates (x_0, y_0) and estimated center coordinates (\hat{x}, \hat{y}) and a is the radius of the target.

The first group of results show that the SAP can successfully localize the objects within their supports under different soil properties. Fig. 4.5(a-c) shows the 10 base logarithm of estimation error for SM, SD, and LM cases. The objects are estimated within their support when the error measure given by (4.9) is less than one, or its 10 base logarithm is less than zero. The white boxes in these figures indicate conductivity and relative permittivity combinations corresponding to realistic soil conditions [69]. It is clear that SAP can locate the targets within a fraction of their radii for all three cases, for all soil conditions.

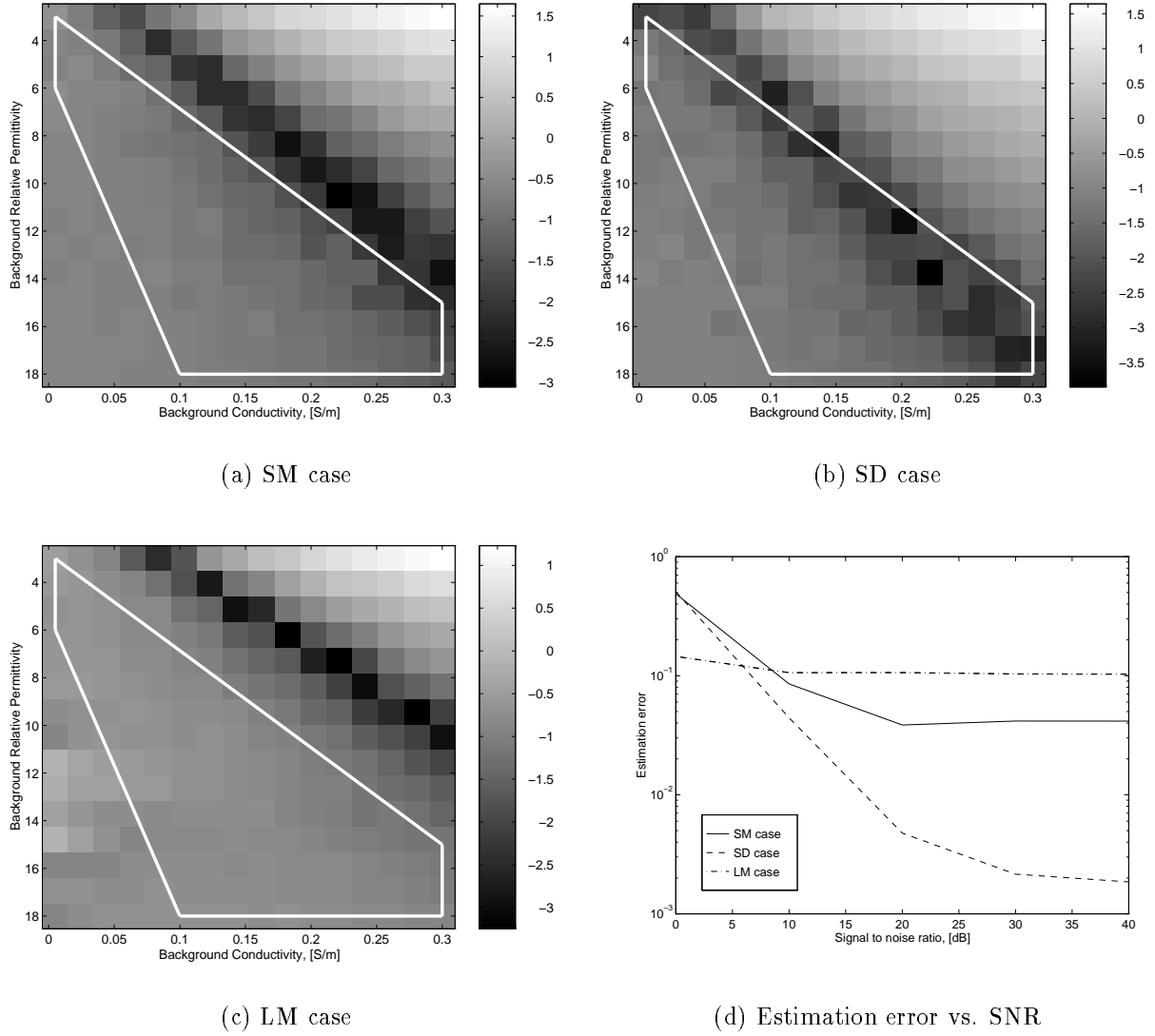


Figure 4.5: The estimation error plotted against background and signal to noise ratio variations. The images in (a)–(c) represent the base 10 logarithm of the error. Thus, values below zero indicate that the center of the object can be localized to within the support of the target.

4.4 Multiple Object Localization Examples

In this section, we present applications of sub-array processing to the detection of multiple mine-like and multiple drum-like objects. In order to simplify the scattering phenomenon associated with the detection problem, both mine-like and drum-like objects are modeled with simple, circular objects. The system parameters for both applications are kept constant to provide a better comparison of the method between applications. In order to introduce frequency diversity, the objects are illuminated with plane waves at three different frequencies: 1.2, 1.0 and 0.8 GHz. The frequency range used is typical of that used in practical subsurface sensing systems. The scattered field is observed along a 33-element, uniform, linear receiver array which spans an aperture of 1.5 m. The sensors are assumed to be ideal, isotropic receivers, and the inter-element spacing of the receivers are chosen such that it is less than half a wavelength for the soil characteristics [69] at the frequencies used. The receiver array is divided into 11 three-element sub-arrays for the processing. Selection of array and subarray parameters should guarantee that the scattered fields would have planar wavefronts at each subarray. Using the criterion given in (4.1), we find that the far field limit is approximately 17.2, 14.4, and 11.5 cm at 1.2, 1.0 and 0.8 GHz, respectively. It should be noted that for most cases, the minimum distance between an object and a subarray is more than 15 cm, which clearly indicates that the wavefronts over each subarray aperture are approximately planar. The objects are placed in a lossy, homogeneous background which has the same electrical characteristics of 5% moist San Antonio clay loam or 10% moist Puerto Rico clay loam ($\epsilon_b = 6\epsilon_0$, $\sigma_b = 5 \times 10^{-2} \text{ S/m}$) at around 1.0 GHz [69].

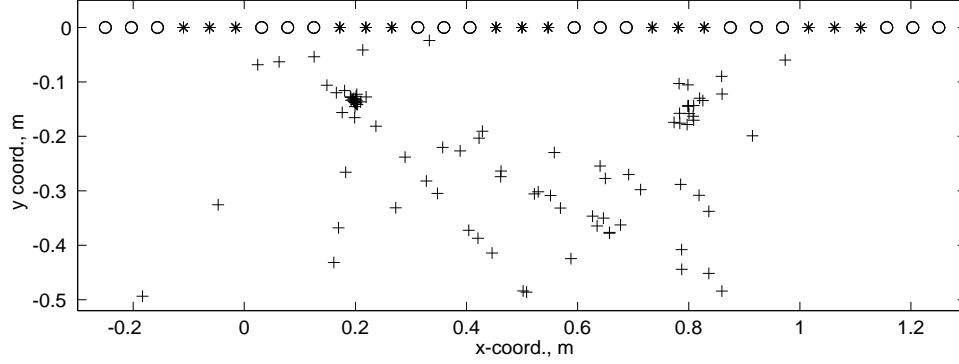
For the simulations, the definition of signal to noise ratio (SNR) is not obvious. In practical problems, SNR is imposed by the nature of the system noise. However, in computer simulations we want to reference the noise power to a fixed quantity that does not change as the positions of the objects change. For this purpose SNR is referenced to the scattered field strength of a single, cylindrical, metallic object placed at the same depth as the objects, in the same lossy medium. The radius of the reference scatterer is the same as the radii of the targets. With this definition, the noise power is always proportional to the power of reference scattered field, not the power of the field scattered from targets, which changes as the positions of objects change.

In all examples the exact scattered field due to multiple objects embedded in a homogeneous, lossy background is calculated using the recursive T-matrix algorithm [16,17,26,33] to keep the computational requirements at reasonably low levels.

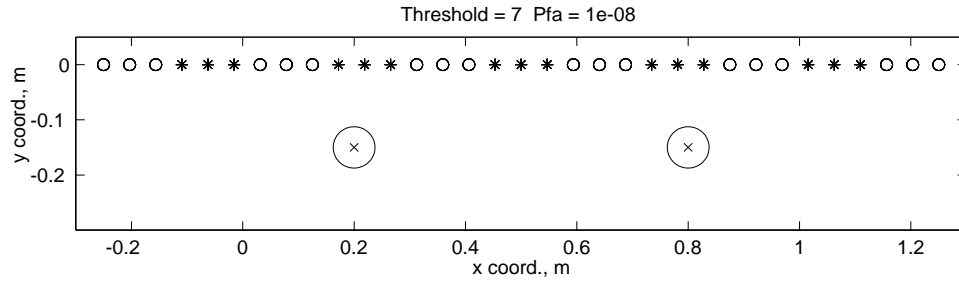
4.4.1 Multiple Mine-like Objects

In these examples, we placed two mine-like objects, each with 7.5 cm. diameter, 15 cm. under the receiver array. Even though the algorithm is capable of detecting more than two objects, it seems likely that for practical purposes no more than two mines will be placed in the array's aperture of 1.5 meters. We have not explored the performance of the processing with respect to varying depth objects, assuming that mine-like objects will be placed at uniform depths under the array.

The first example demonstrates the utility of the sub-array processing in detecting and



(a) DOA crossings



(b) Detection windows overlaid on true object positions

Figure 4.6: Multiple mine-like object detection with SAP: object on the left is metallic and object on the right is dielectric with $\epsilon_r = 2.5$. o's and *'s denote subarrays

localizing both a metallic and a dielectric object in the same medium. For this purpose, a metallic object and a dielectric object with dielectric constant of 2.5 are placed at (20, -15) cm and (80, -15) cm, respectively, in the homogeneous background described before, Fig 4.6. Signal to noise ratio is fixed at 10 decibels. Fig 4.6 shows the directions of arrivals, and detection windows when probability of false alarm is 10^{-8} , which corresponds to a crossing threshold of $K = 7$. The two circles in this figure denote the objects, and the intertwined squares, due to overlaps in test windows, depict the estimated target windows. The detection

windows are then used in the grouping algorithm described in Section 4.2.3. As expected two distinct groups of overlapping windows indicated that there are two objects beneath the array. The estimated center for the objects are found to be $(19.52, -14.02)$ cm and $(80.10, -14.82)$ cm. Consequently, both metallic and dielectric objects are detected within acceptable estimation error margins.

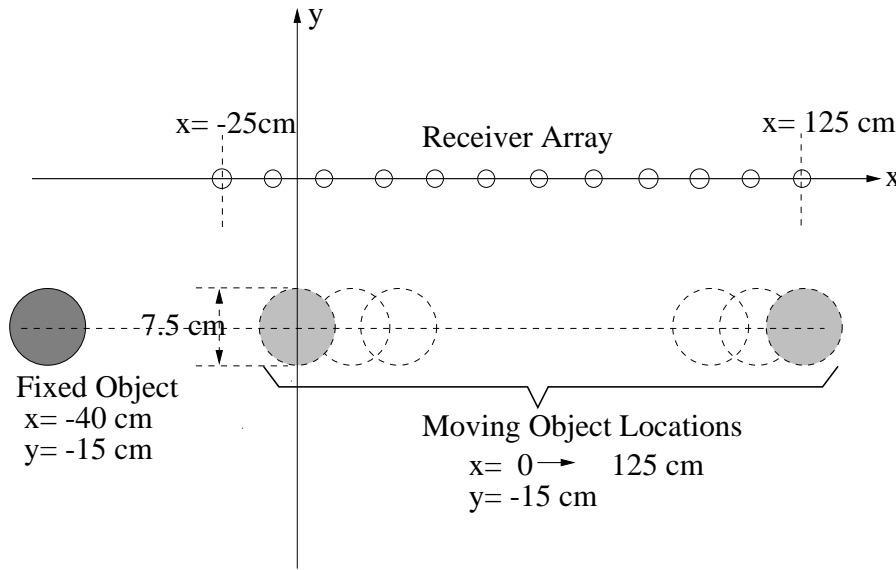


Figure 4.7: Multiple mine-like object detection with SAP: geometry for the example about the effect of relative distance between objects. Both objects are perfect conductors

Next, we consider an example that demonstrates the detectability of objects and the performance of SAP as relative positions of the objects change. In this example, both objects are assumed to be metallic in order to see the influence of relative distance between same type of objects on detectability and estimation error. For this purpose, we fixed the location of the first object at $(x, y) = (-40, -15)$ cm. The other one is moved from $x = 0$ cm to $x = 125$ cm in the lateral direction while its depth is kept at the same level as the fixed object, Fig. 4.7. The signal to noise ratio is assumed to be 30 decibels.

With this geometry, the moving object is always located under the array, and thus detected for all combinations of relative positions. Detection of the fixed object, on the other hand, is challenging since it lies outside the span of the array. Fig 4.8 shows the average simulated probability of detection of the fixed object over 100 Monte-Carlo simulations as the other object is moved under the array when probability of false alarm is set to 10^{-3} . As it is clear from this figure, the fixed object can be detected only if the other object is well away from it. The fixed object may also be detected with less than 10% probability when the moving object is located between $x = 0$ and $x = 20$ cm. This is due to the fact that for these relative locations, both objects are close enough so that DOAs belonging to the moving object create crossings around the fixed object as well as the moving object. In fact, because of this effect, the region between the two objects is incorrectly detected as targets, and thus false alarm rate is large when relative distance between two objects is small, Fig. 4.9. Simulated $P_{fa,sim}$ as depicted in Fig. 4.9 approaches to the false alarm rate set at the beginning of the simulation (dashed line), as the relative distance between the objects increase.

We have also investigated the effect of relative distance on estimated object centers. For this purpose, we plotted the averaged estimation error in x -direction ($\Delta x = x_{true} - x_{estimated}$) versus the averaged estimation error in y -direction ($\Delta y = y_{true} - y_{estimated}$) for both fixed and moving objects in Fig. 4.10(a-b). The estimated object coordinates are obtained by averaging 100 Monte-Carlo simulations. For the case when the objects are located at (-40,-15) cm and (125,-15) cm, the estimated object centers are (-43.32,-16.17) cm and (126.09,-15.05) cm. For

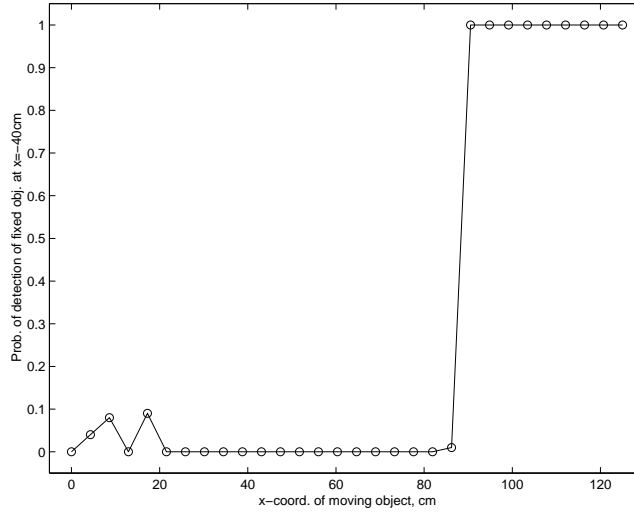


Figure 4.8: Probability of detection of the fixed object when the other object moves under the receiver array

the same case, the standard deviations over all Monte-Carlo simulations are $(2.269, 1.587)$ cm and $(0.297, 0.163)$ cm. As expected, the mean center and the standard deviation for the object located outside the span of the array is worse than those for the object located at the right edge of the array. The dashed circles indicate the boundaries of the objects. The closer the symbols (o's or \diamond 's) are to the center, the smaller is the estimation error. Since the moving object is always detected, each small circle in Fig. 4.10(a) corresponds to a different position of the moving object. As seen from this plot, the estimation error of the moving object is only a small fraction of the radius. Small circles outside the object boundary (dashed circle) correspond to locations where the moving object is close to the fixed object. Each small circle and diamond in Fig. 4.10(b) corresponds to a relative position when the fixed object is detected. The small circles denote the error in estimated centers when the moving object's x -coordinate is greater than 95 cm, and small diamonds correspond to other locations of the moving object for which the fixed object is detected. The loci of small circles and diamonds

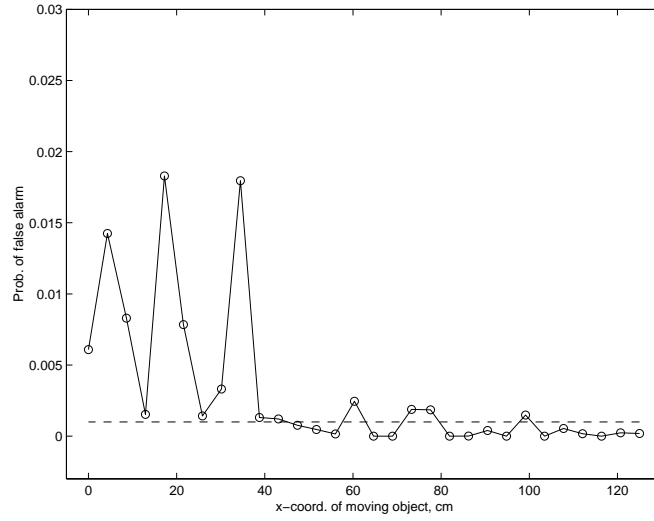


Figure 4.9: Probability of false alarm, when the moving object is located under the receiver array at various positions, dashed line shows the desired false alarm rate of 10^{-3}

clearly imply that as the relative distance between the objects gets larger, the estimation error in the position of the fixed object gets smaller.

The last example in this section will be the localization of randomly placed objects. For this purpose, two metallic mine-like objects are located randomly in $-25 \leq x \leq 125$ cm and $-30 \leq y \leq -10$ cm. The x and y -coordinates of the objects are obtained from independent random variables uniformly distributed over the ranges specified. If the random positions result in overlaps of objects, we repeated the random experiment to generate a new set of object positions. The signal to noise ratio is 30 dB as before, and 1000 Monte-Carlo simulations have been performed. We repeated this experiment for three different probabilities of false alarm, 10^{-1} , 10^{-3} and 10^{-6} . These false alarm rates correspond to different threshold values for the hypothesis test described by (4.6).

There are several issues associated with localization of randomly placed objects. The

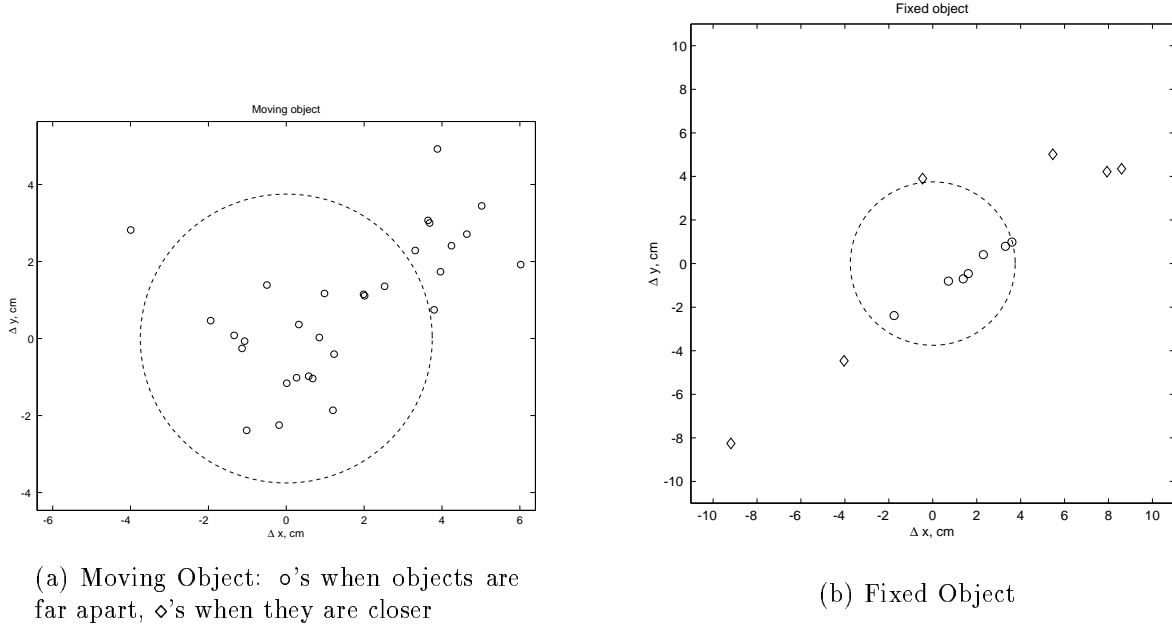


Figure 4.10: Estimation errors in object centers, each symbol corresponds to a different position of the moving object. Number of symbols in (b) is considerably less, since the fixed object is not detected for all positions of the moving object, see Fig. 4.8.

first one is that SAP cannot always detect both objects, since for some cases the objects are far too closer for SAP to resolve them. In fact, Fig. 4.11 shows a histogram of distances between two objects whose coordinates are obtained from a uniform random variable. As clear from this figure, for almost half of the realizations, the distance between the scatterers is less than 50 cm. We define a $P_{det,both}$ as the probability of detection of both objects. An estimated object center is assumed to be a detection if it is within a diameter length. We also define N_{two} as the number of realizations for which the SAP concluded that there are two targets in the region of interest. For other cases, the SAP detects only one object, or none at all. We define N_{one} as the number of realizations for which SAP determines that there is

at least one object in the region of interest, and $P_{det,one}$ as the probability of detection of one object. Table 4.1 denotes these parameters for different preset false alarm rates. The poor performance of SAP in these cases is attributed to the way we selected the random positions of the objects. As Fig. 4.11 shows, for most cases the objects are too close to resolve.

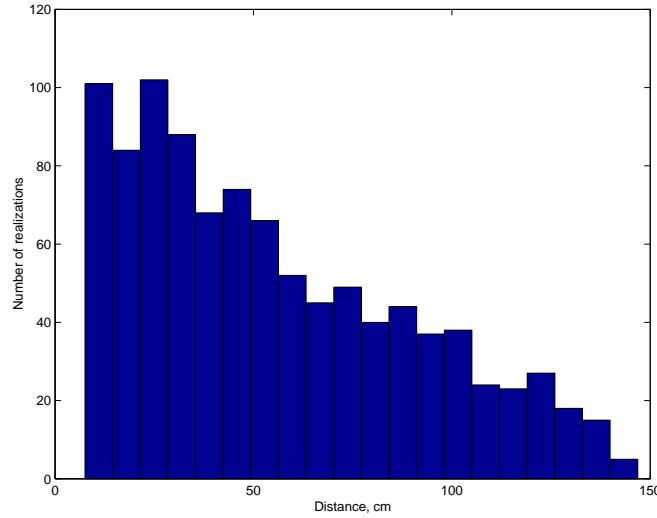


Figure 4.11: Histogram of distances between two objects whose coordinates are obtained from independent, uniform random variables

P_{fa}	$\langle K \rangle$	N_{two}	$P_{det,both}$	N_{one}	$P_{det,one}$
10^{-1}	1.15	323	0.134	509	0.322
10^{-3}	2.86	494	0.375	650	0.513
10^{-6}	4.55	518	0.422	719	0.571

Table 4.1: Results of localization of randomly located objects. $\langle K \rangle$ is the mean threshold averaged over 1000 realizations.

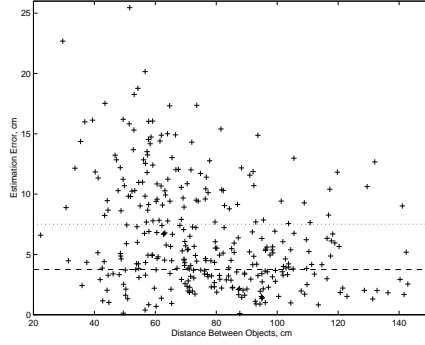
In Fig. 4.4.1, we show the performance results for randomly positioned objects. The figures on the left depict the distance separating the two objects versus the estimation error for three different false alarm rates. Histograms on the right show the distribution of estimation errors for the plots on the left. The dashed lines indicate the radii of the objects,

and the dotted lines indicate the diameter of the objects. These figures clearly indicate that as the relative distance between objects increase, the detection performance of SAP increases with a noticeable threshold between 50 and 60 cm.

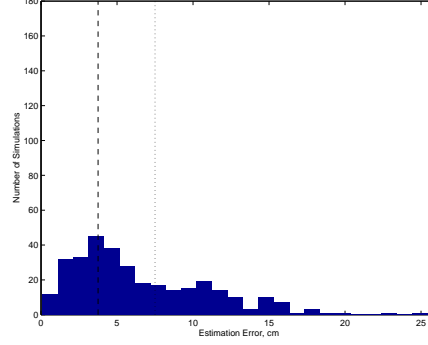
As mentioned before, the random placement of the objects is a quite difficult test for SAP, since the objects can be very close most of the time, Fig. 4.11. While finding the random positions, we only prevented the overlap of objects. However, it might be a better idea to impose a larger minimum separation between two objects to measure the performance of SAP.

4.4.2 Multiple Drum-like Objects

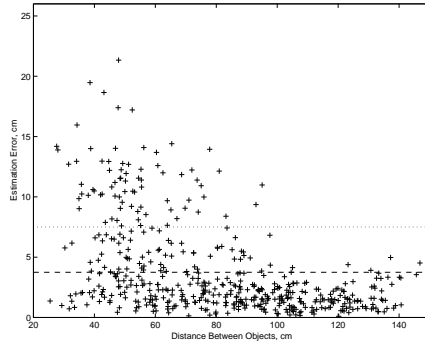
In this section, two drum-like objects, each with 50 cm. diameter, are placed at various depths from the receiver array. Since drums are made of metal, the objects are assumed to have infinitely large conductivity. The signal to noise ratio is set at 10 decibels. The detection windows for a typical case is shown in Fig. 4.13. In this example one object is at $(-40, -125)$ cm and the other is at $(140, -125)$ cm, while the lossy, homogeneous background is the same as previous example. The threshold of detection corresponding to a false alarm rate of 10^{-8} is found to be $K = 6$. Fig. 4.13(b) depicts the detection windows obtained after hypothesis testing. These windows are then processed by the grouping algorithm of Section 4.2.3. As expected, we found two overlapping window groups which imply that there are two objects in the region of interest with centers located at $(-40.02, -111.70)$ cm and $(139.93, -108.46)$ cm.



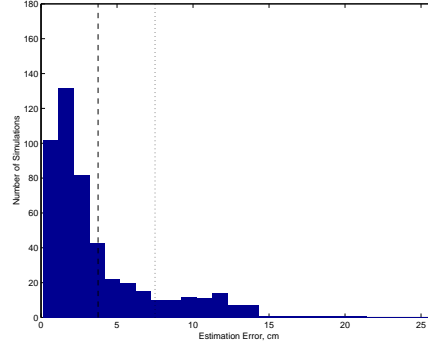
(a) Relative distance vs. estimation error for $P_{fa} = 0.1$



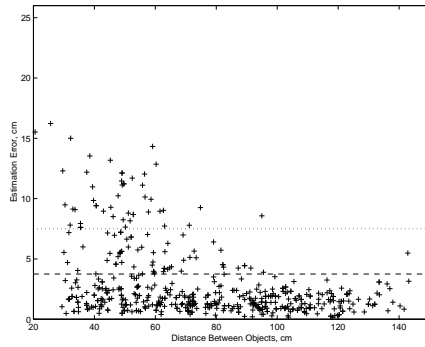
(b) Histogram of estimation error for $P_{fa} = 0.1$



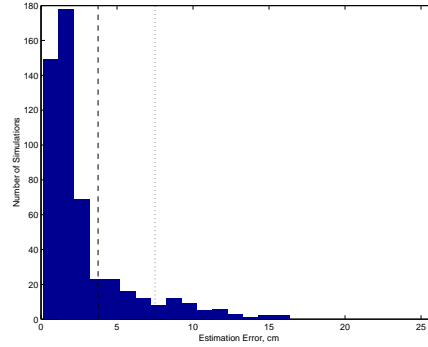
(c) Relative distance vs. estimation error for $P_{fa} = 10^{-3}$



(d) Histogram of estimation error for $P_{fa} = 10^{-3}$

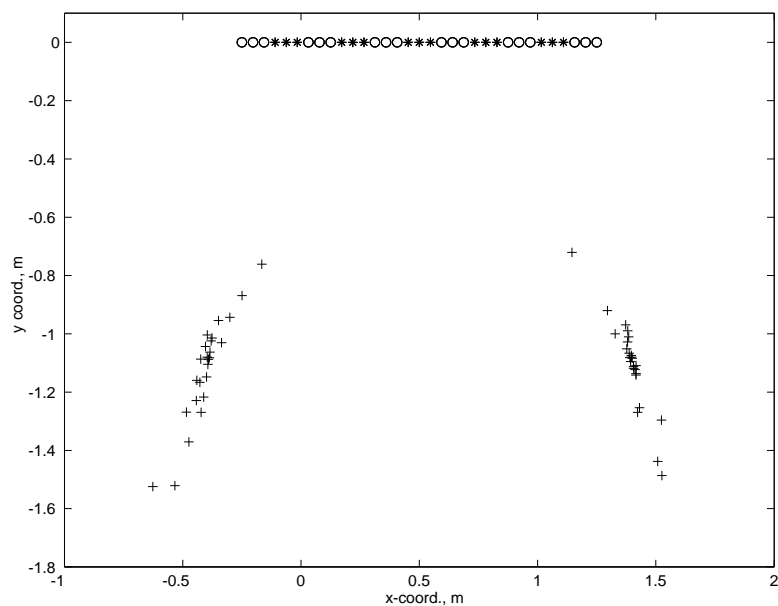


(e) Relative distance vs. estimation error for $P_{fa} = 10^{-6}$

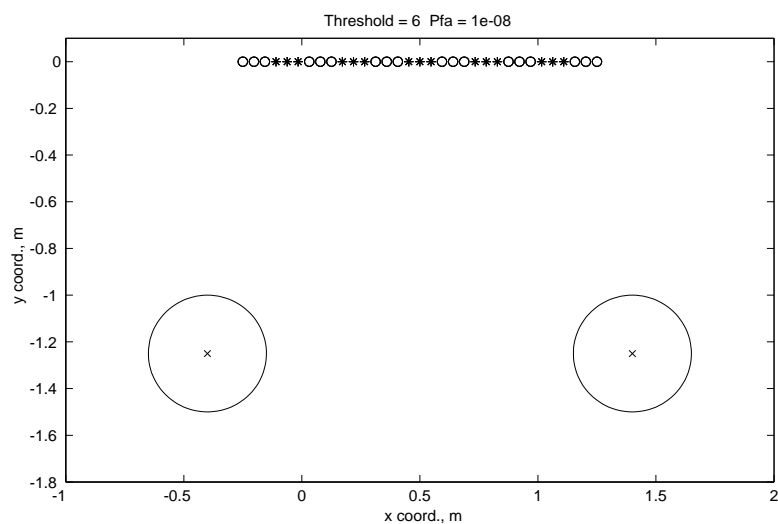


(f) Histogram of estimation error for $P_{fa} = 10^{-6}$

Figure 4.12: SAP results of randomly placed objects for $P_{fa} = 0.1$ [(a)–(b)], $P_{fa} = 10^{-3}$ [(c)–(d)], and $P_{fa} = 10^{-6}$ [(e)–(f)]. The dashed lines indicate the radii of the objects, and the dotted lines indicate the diameter of the objects



(a) DOA crossings



(b) Detection windows overlaid on true object positions

Figure 4.13: Localization of two metallic drum-like objects with SAP, o's and *'s denote subarrays

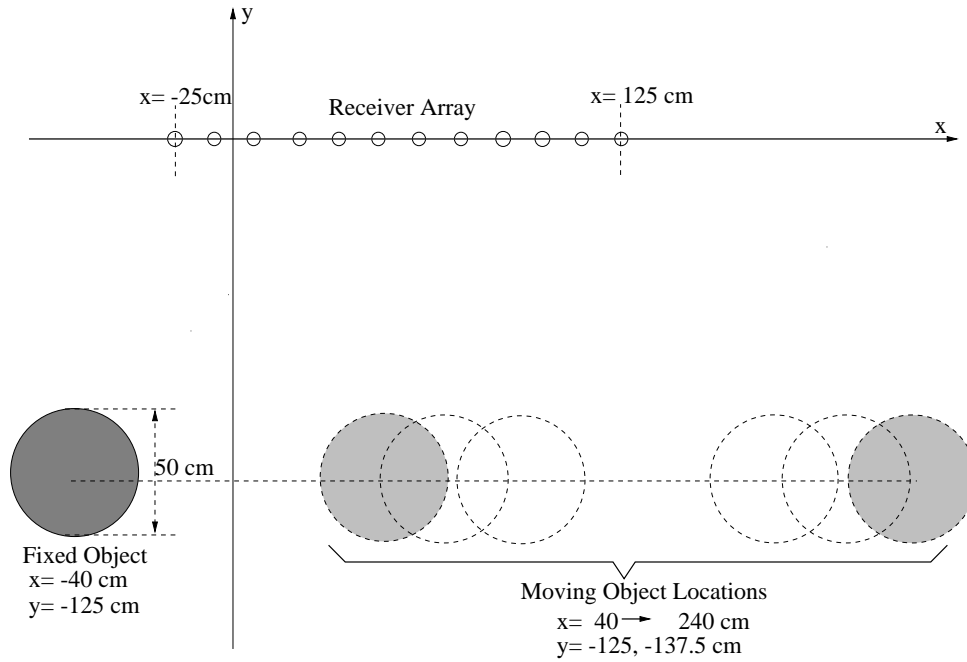


Figure 4.14: Multiple drum-like object detection with SAP: geometry for the example about the effect of relative distance and depth between objects. Both objects are perfect conductors

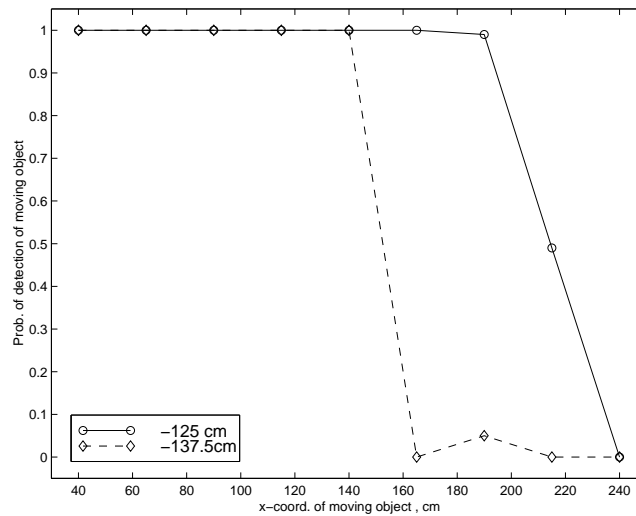
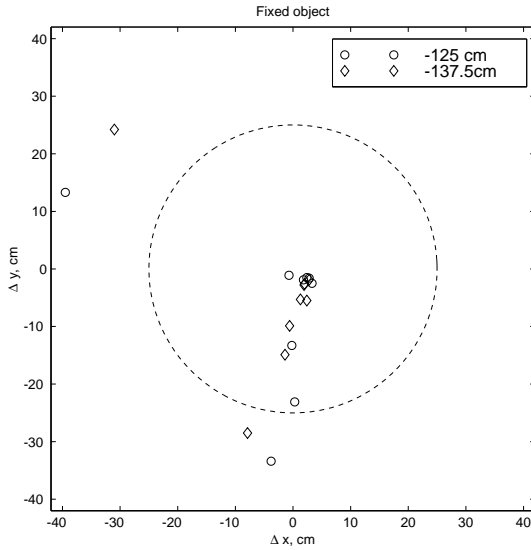


Figure 4.15: Probability of detection of the moving object, when the fixed object is located at $(-40, -125)$ cm. The solid line and dashed lines show the probability of detection when the moving object is at depth -125 cm and -137.5 cm, respectively.

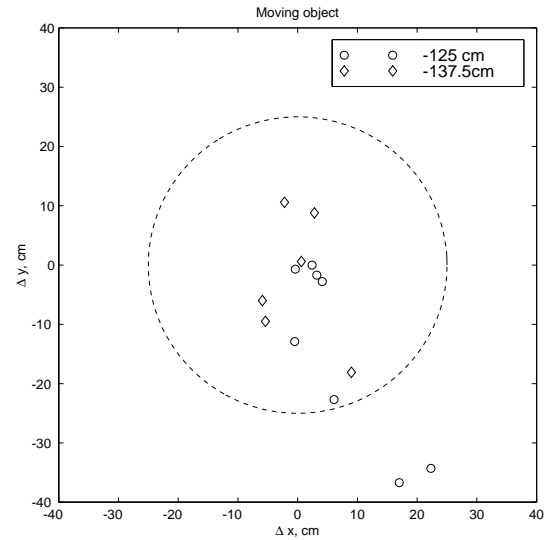
As the second example of this section, we considered keeping one of the objects at a fixed location, and moving the other object around below the array. The first object is fixed at $(-40, -125)$ cm, and the other is moved from $x = 40$ cm to $x = 240$ cm in the lateral direction at two different depths, -125 cm and -137.5 cm, Fig. 4.14. The SNR is set to 30 dB. Contrary to the mine-like object example, in this case the fixed object is at an advantageous location and detected with a probability of 1.0 regardless of the position of the moving object in the defined region. The moving object is hard to detect, since it is placed either outside the span of the array most of the time, or deeper than the fixed object. Fig. 4.15 depicts the average probability of detection of the moving object over 100 Monte-Carlo simulations for two depths when probability of false alarm is set to 10^{-3} . It is clear that as the moving object is placed far from the array, it is less likely to be detected. Relative to the depth of the fixed object, if the moving object is placed deeper, it has to be nearer to the array to be detected. Simulated probability of false alarm ($P_{fa,sim}$) for this example is zero for all positions of the moving object, since both objects are too far apart to cause a false detection window.

We have also investigated the effect of relative distance and depth on estimated object centers. For this purpose, we plotted the estimation error in x -direction ($\Delta x = x_{true} - x_{estimated}$) versus the estimation error in y -direction ($\Delta y = y_{true} - y_{estimated}$) for both fixed and moving objects for two depths in Fig. 4.16(a-b). The estimated object coordinates are obtained by averaging 100 Monte-Carlo simulations. The dashed circles indicate the boundaries of the objects. Circles shows the estimation errors when both objects are at the

same depth, and diamonds show those when the moving object is a half radius deeper than the fixed object. Symbols (circle/diamond) inside the dashed circle indicate the estimation errors less than the radius of the object. In Fig. 4.16(a-b) it is observed that as the moving object gets far from the array, the estimation error in position of the moving object increases, and that in position of fixed object becomes smaller. Placing the moving object at a deeper location increases the estimation error in its position, and slightly improves that in fixed object's position.



(a) Fixed Object. Depth of the moving object: o=-125 cm and ◊=-137.5 cm.



(b) Moving Object. Depth of the moving object: o=-125 cm and ◊=-137.5 cm.

Figure 4.16: Estimation errors in object centers, each symbol corresponds to a different position of the moving object. Number of symbols in (b) is less than that in (a), since it is not detected for all positions of the moving object, see Fig. 4.15.

4.5 Summary

In this chapter we presented an algorithm that can detect and localize an unknown number of objects in the near field of a linear sensor array. The issues related to near-field scattering were overcome by partitioning the full array into sub-arrays so that the non-planar scattered field becomes locally planar at each sub-array. DOAs corresponding to these locally planar waves were then determined using array processing techniques. Triangulation of such DOAs resulted in a pattern of dense and sparse regions of crossings which are modeled with a pair of spatial Poisson distributions. Estimated object locations and the number of objects are finally obtained by applying a hypothesis test to Poisson models and then extracting groups of spatially disjoint detection windows.

We demonstrated the performance of the algorithm using simulated data. The usefulness of this algorithm was exhibited for both mine-like and drum-like objects. For mine-like targets, we showed that the algorithm can detect and localize multiple targets with different electrical properties. Then, we demonstrated the detectability of such objects when relative distance between them changes. We concluded that the detectability improves as the objects are located farther from each other while staying within a reasonable distance from the array. In addition, it was shown that theoretical and simulated probabilities of false alarm and detection were in agreement. For drum-like targets, we demonstrated the usefulness of the algorithm for detection and localization of multiple objects. Furthermore, the effect of relative distance and relative depth on detectability was treated. Results of this analysis supported the results obtained for mine-like objects.

Chapter 5

Detection and Localization: Matched Field Processing

The algorithms presented in this chapter modify the conventional direction finding array processing techniques, and use the spatial complexities of the fields to determine both the range and the bearing of the targets in the region of interest. For multiple object localization, we considered both the case when the electromagnetic interactions between objects are taken into account and also when they are ignored. Examples of typical object localization geometries are given in Section 5.5.

We also compute explicitly the analytical expressions for the Cramér-Rao bounds (CRB) for position estimates in Section 5.4. The Cramér-Rao Bound gives the lower bound for the variances of the estimates, and thus, specifies the lowest possible error variance that can be attained with an unbiased estimator. The theoretical Cramér-Rao bounds are then verified

using Monte-Carlo simulated error variances in Section 5.5. A summary of the chapter will be presented in Section 5.6.

5.1 Introduction

In this chapter, we solve the object localization problem described in Section 4.1 with a completely different approach. Here, instead of using conventional plane wave MUSIC, we use the MUSIC method in a matched field processing [30] framework to account for non-planar wavefronts.

As we discussed in Chapter 4 in detail, knowledge of the DOA is sufficient for characterizing a planar wavefront, since the range of the radiator for this case is infinity. For the near-field target localization problem, however, the fields impinging on the array have non-planar wavefronts. Therefore, the scattered field in this case should be characterized by both the range and the bearing variables in order to localize a target. Matched field processing (MFP) [30] has been successfully used for localization of point sources in ocean acoustics. MFP is an array processing technique that uses the spatial complexities of the fields to localize sources, and thus allows for estimation of both the range and the bearing of the objects.

Here, we present a MFP-based algorithm that localizes multiple, extended near-field scatterers when electromagnetic interactions are taken into account. The physical phenomenon associated with multiple scattering is modeled exactly, and the model is formulated in target coordinates explicitly using the recursive T matrix algorithm [16, 17, 33]. For single object

localization, we use the Mie series expansions [70] to calculate the scattered field over the receiver array. For localization of multiple scatterers, we have two options. We may ignore the electromagnetic interactions between targets, and treat the problem as if a number of independent, single scatterers are scattering the incident electromagnetic field. While the resulting method has the same order of computational complexity of the single object case, its accuracy deteriorates as objects get closer and the multiple scattering effects become more prominent. Furthermore, scattering from multiple, independent, single scatterers results in the signal coherence issue which will be addressed in detail in Section 5.3.2.

The second option in localizing multiple objects is to take multiple scattering effects into consideration. While this approach is more computationally costly than the former, by modeling the non-trivial interactions of wavefields among scatterers, we improve our ability to resolve closely spaced scatterers. In fact, it can easily localize the targets in geometries where the former approach fails to resolve the target positions.

Finally, we will derive the Cramér-Rao bounds for the multiple object detection scenario. Our Cramér-Rao Bound derivation adapts the results in [49], and accounts for near field observations. Analytical bounds of estimated object coordinates are then validated by running Monte-Carlo experiments for the estimator presented in this chapter.

The remainder of the chapter is organized as follows. In Section 5.2, we introduce the data model used in the algorithm. In Section 5.3, we introduce the matched field processing for localization of single and multiple objects. The Cramér-Rao lower bound for MFP is derived in Section 5.4. Numerical examples are presented in Section 5.5, and in Section 5.6,

we conclude with a summary.

5.2 Data Model

The near field measurement scheme depicted in Fig. 2.3 is considered. The objects are buried in a background for which the constant electrical characteristics (relative permittivity and conductivity) are assumed known. A transverse magnetic (TM) polarized plane wave, $E_i(\mathbf{r})$, impinges on the objects, inducing surface and volume currents which in turn radiate a scattered field, $E_s(\mathbf{r})$ ¹. An important assumption in our approach is that the material properties and the shapes of the objects are known a priori, since in most of the practical problems of interest we have a general idea of these properties. We also assume that the number of scatterers is known. Thus, we are particularly interested in finding only the positions of these targets.

The scattered electric field from N objects is spatially sampled by a uniformly spaced, linear array with M isotropic receivers, $M > N$. When the multiple scattering effects are taken into consideration, the measured data at the sensor outputs can be written as:

$$\mathbf{y} = \mathbf{A}\mathbf{x} + \mathbf{n}, \quad (5.1)$$

where $\mathbf{A} = [\mathbf{E}_{s1}(\mathbf{r}_1, \dots, \mathbf{r}_N) \ \mathbf{E}_{s2}(\mathbf{r}_1, \dots, \mathbf{r}_N) \ \dots \ \mathbf{E}_{sN}(\mathbf{r}_1, \dots, \mathbf{r}_N)]$. Each vector $\mathbf{E}_{si}(\mathbf{r}_1, \dots, \mathbf{r}_N)$ is $M \times 1$, and denotes the scattered field observed at the array due to the i th object, in the presence of all other $(N - 1)$ scatterers, $i = 1, 2, \dots, N$. The vector $\mathbf{E}_{si}(\mathbf{r}_1, \dots, \mathbf{r}_N)$ can be calculated using the modified recursive T-matrix algorithm presented in Chapter 3. For time

¹All analysis is in the frequency domain, and thus the $e^{j\omega t}$ time dependence will be dropped.

domain applications, the vector \mathbf{x} contains the narrow band time variations. Since we do our analysis in the frequency domain, and suppress $e^{j\omega t}$, $\mathbf{x} = [1 \ 1 \cdots 1]^T$. The i th column of matrix \mathbf{A} depends not only on the position of the i th object, but also that of $(N - 1)$ other objects. Therefore, for practical purposes, we may replace \mathbf{Ax} in (5.1) with an $M \times 1$ vector $\mathbf{B} = \mathbf{E}_s(\mathbf{r}_1, \mathbf{r}_2 \cdots \mathbf{r}_N) = \mathbf{E}_{s1}(\mathbf{r}_1, \dots, \mathbf{r}_N) + \mathbf{E}_{s2}(\mathbf{r}_1, \dots, \mathbf{r}_N) + \dots + \mathbf{E}_{sN}(\mathbf{r}_1, \dots, \mathbf{r}_N)$, which denotes the total scattered field at the receiver array.

The recursive T matrix algorithm [16,17,33] can be used to calculate the exact scattered field $\mathbf{E}_{si}(\mathbf{r}_1, \dots, \mathbf{r}_N)$ due to the i th object in the presence of other objects. The algorithm described in Chapter 3 is designed for the efficient solution of near field scattering problems with a heterogeneous collection of metallic and dielectric objects. In addition, the recursive T-matrix algorithm can be written in a closed form, which enables us to take derivatives analytically. This property is especially useful in obtaining gradients and derivatives in the multi-dimensional parameter search and in the Cramér-Rao Bound analysis presented in Sections 5.3.3 and 5.4, respectively.

As mentioned in the introduction of this chapter, electromagnetic interactions between the objects may be ignored to reduce the computational complexity. For this case we have the same data model as in (5.1), except that the matrix \mathbf{A} is redefined to be

$$\mathbf{A} = [\mathbf{E}_s(\mathbf{r}_1) \ \mathbf{E}_s(\mathbf{r}_2) \cdots \mathbf{E}_s(\mathbf{r}_N)] \quad (5.2)$$

where each $M \times 1$ vector $\mathbf{E}_s(\mathbf{r}_i)$ denotes the scattered field due to a single object located at \mathbf{r}_i , $i = 1, 2, \dots, N$, and is calculated using the Mie series. Therefore, each column of \mathbf{A} contains the scattered field that is a function of position of only one particular object. The

vector \mathbf{x} is the same as before, $\mathbf{x} = [1 \ 1 \cdots 1]^T$.

5.3 Matched Field Processing for Object Localization

Matched field processing was introduced to use the spatial complexities of the relevant fields to localize sources in underwater acoustics or to infer parameters of the ocean waveguide itself [30]. In a similar manner, plane wave MUSIC outlined in Chapter 2 can be modified so that the direction vector is filled with the type of wavefront impinging on the array [1,2]. As a result, the problem of non-planar wavefronts caused by near field scattering is resolved, and both the range and angle of the scatterer can be estimated. We have divided this section into three parts: in the first we will describe single object localization. Even though single object localization is a subset of multiple object localization, we present it separately in order to explain the multiple object case more clearly. The second part will deal with multiple objects, but the electromagnetic interaction between objects will be ignored. In the last part, we will treat multiple object detection problem when the multiple scattering effects are taken into account.

5.3.1 Single Object Localization

By using the spatial distribution of the scattered field, we can fill the so-called direction vector in plane wave MUSIC with non-planar scattered fields to locate the near field objects. By modifying the spatial MUSIC spectrum in (2.14), we form the following spectrum:

$$P_{MUSIC}(r, \theta) = \frac{\mathbf{E}_s(r, \theta)^H \mathbf{E}_s(r, \theta)}{\mathbf{E}_s(r, \theta)^H \hat{\mathbf{\Gamma}}_n \mathbf{E}_s(r, \theta)} \quad (5.3)$$

where the new “direction” vector (actually, the *locus vector* in r and θ space) $\mathbf{E}_s(r, \theta)$ is now filled with the type of wavefront expected to impinge on the receiver array. For the single object localization problem the vector $\mathbf{E}_s(r, \theta)$ is filled with the scattered field when an object is located at $\mathbf{r} = (r, \theta)$. Then, the location $(\hat{r}, \hat{\theta})$ maximizing the MUSIC spectrum in (5.3) is selected as the estimated object center. Because a two dimensional search requires that the exact scattered field be calculated at each point of the parameter mesh, this technique is in general computationally intensive. In the event that the object to be detected is modeled as a simple shape, however, computing the exact scattered field can be relatively simple. When the targets are modeled as infinitely long cylinders in two dimensions, the scattered field from such objects due to a plane wave can be calculated using the Mie series [67, 70]:

$$E_s(\rho, \phi) = \sum_{n=-\infty}^{\infty} c_n H_n^{(2)}(k\rho) e^{jn(\phi + \pi - \phi_{inc})} \quad (5.4)$$

where $H_n^{(2)}(.)$ is the Hankel function of the second kind of order n representing cylindrical outgoing waves, k is the wavenumber in the homogeneous, possibly lossy, background, and ϕ_{inc} is the incidence angle of the plane wave. The coefficients c_n are determined from the boundary conditions when ρ is equal to the radius of the cylinder. For computer implementations, the infinite sum in (5.4) is truncated at a finite value beyond which the coefficients c_n are below machine precision. Here ρ and ϕ denote the coordinates of the receivers since (5.4) assumes that the center of the cylinder is located at the origin. In implementing the MUSIC spectrum in (5.3), however, translations from object-to-receiver coordinate system

(ρ, ϕ) to array-to-object-position coordinate system (r, θ) are required. These translations do not significantly alter the computational load or functional form implied by (5.4).

To summarize, the MUSIC-based MFP algorithm proceeds as follows:

1. Using the data model in (5.1), perform L , single-frequency scattering experiments each producing a snapshot vector, \mathbf{y}_l , composed of the observed scattered fields over the receiver array
2. Estimate the autocovariance matrix $\hat{\mathbf{R}}$ using (2.11)
3. Perform an eigenanalysis on $\hat{\mathbf{R}}$ to find the noise-subspace projector using $\hat{\mathbf{\Pi}}_n$ (2.12) and (2.13)
4. Carry out a two-dimensional search in the target position space (r, θ) . For each point (r_k, θ_k) on a predefined range and angle grid, fill in the locus vector $\mathbf{E}_s(r_k, \theta_k)$ with the scattered field due to an object placed in that location, and calculate the associated value of $P_{MUSIC}(r_k, \theta_k)$ in (5.3)
5. Choose $(\hat{r}, \hat{\theta})$ as the estimate of the target location as the grid point with the largest P_{MUSIC} .

Fig. 5.1(b) shows the MUSIC spectrum for the mine-like object localization scenario when a small metallic object in 7.5 cm diameter is placed 15 cm below the array as depicted in Fig. 5.1(a). The 33-element linear, uniform receiver array spans an aperture of 1.5 meters. All sensors are assumed to be ideal, isotropic receivers. The operating frequency is 1.0 GHz and the plane wave is incident with 90 degrees. The lossy, homogeneous background has the same electrical characteristics of 5% moist San Antonio clay loam or 10% moist Puerto Rico

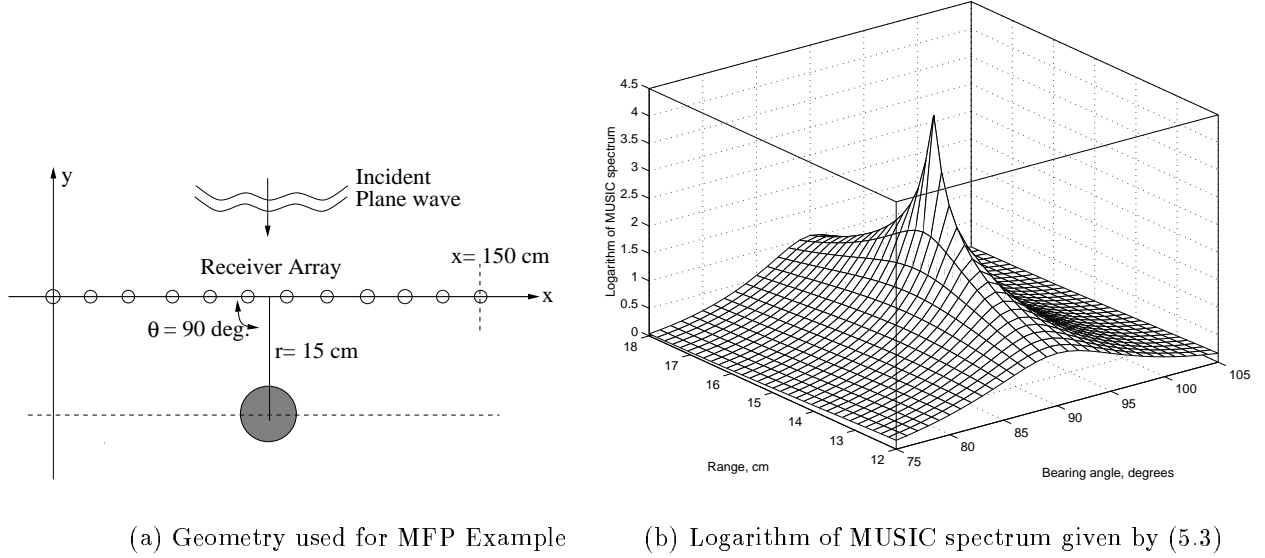


Figure 5.1: MFP localization example: single metallic object in a lossy, homogeneous background

clay loam ($\epsilon_b = 6\epsilon_0$, $\sigma_b = 5 \times 10^{-2} \text{ S/m}$) at around 1.0 GHz [69]. The signal to noise ratio (SNR) is fixed at 0 decibels. As Fig. 5.1(b) depicts, the location of the object ($r = 15\text{cm}$, $\theta = 90^\circ$) is indicated with a very sharp peak. We note that the prominent peak structure of the spectrum in this example is representative of a wide range of other cases for which the background electrical properties, target electrical characteristics and the signal to noise ratios are varied. For this purpose, in [1] the background dielectric constant is changed from 3 to 18 and the the background conductivity is changed from 5×10^{-3} to $0.3 \frac{\text{S}}{\text{m}}$. For each of these background properties, the signal to noise ratio is varied from 0 to 40 dB, for both metallic and dielectric scatterers with a relative permittivity of 2.5. In all cases, we observed a sharp peak as in Fig. 5.1(b).

5.3.2 Multiple Object Localization: No Interaction

In this section, we describe multiple object localization when the electromagnetic interaction between objects are ignored. While neglecting the interactions reduces the computational demand of localization considerably, it may introduce large estimation errors if the interactions are in fact sizeable. Therefore, we need a criterion that tells us when the multiple scattering effects between objects can or cannot be ignored. For this purpose, we derived the analytical expressions for the interaction terms between two infinitely thin scatterers in Appendix B. As we will show in Section 5.5.1, the normalized interaction terms for filamentary objects bound those for the extended objects for a wide range of distances. Thus, the simple expression in Appendix B can be used to determine the degree of interaction between two scatterers in terms of their spacing and the electrical properties of the medium of propagation. By selecting a desired interaction level, we may calculate the minimum distance between scatterers that satisfy this a priori level. If the actual distance is smaller than the minimum distance, then we should not ignore the interactions between scatterers, and use the technique presented in Section 5.3.3 to accurately localize the objects.

Assuming that the objects are located relatively far apart, so that the interactions among them can be ignored, the multiple object localization becomes similar to having multiple plane waves incident on the array for plane wave MUSIC. For this case, the scattered field due to one object is independent of the positions of the other objects. Because of the structure of \mathbf{x} in (5.1), the rank of the covariance matrix of \mathbf{x} , $\mathbf{P} = E\{\mathbf{x}\mathbf{x}^H\}$, is one, and so is the rank of \mathbf{R} . Thus, the signals impinging on the array are coherent since the fields are the

same wavefronts emanating from different locations. It is well known that the performance of subspace based methods degrades severely for resolving coherent signals. Therefore, these coherent signals should be decorrelated before using MUSIC. To increase the rank of the spatial autocovariance matrix, i.e. to decorrelate the signals, we will use frequency diversity as described in the next paragraph.

Since the number of targets, N , in the region of interest is known, we repeat the scattering experiment as represented by (5.2) at N different frequencies. Thus (2.11) becomes:

$$\hat{\mathbf{R}}_i = \frac{1}{L} \sum_{l=1}^L \mathbf{y}_{li} \mathbf{y}_{li}^H \quad (5.5)$$

where \mathbf{y}_{li} is the data vector observed at the i th operating frequency, f_i , and $\hat{\mathbf{R}}_i$ is the spatial autocovariance matrix at f_i , $i = 1, 2, \dots, N$. Then, the rank enhanced autocovariance matrix $\hat{\mathbf{R}}_d$ is obtained by

$$\hat{\mathbf{R}}_d = \frac{1}{N} \sum_{i=1}^N \hat{\mathbf{R}}_i. \quad (5.6)$$

In Appendix C, we prove for two objects ($N = 2$) that in the limiting case of infinitesimal object radius, frequency diversity does, in fact, increase the rank of the autocovariance matrix $\hat{\mathbf{R}}_d$ to two.

Once the signals are decorrelated, we form the MUSIC spectrum given in (5.3), where the locus vector $\mathbf{E}_s(r, \theta)$ is filled with the scattered field due to a single scatterer located at (r, θ) . The scattered field is calculated using the Mie series in (5.4). Since the scattered field due to one object is assumed independent of position of other objects, it is sufficient to search for target locations in two dimensions, i.e. (r, θ) -space. The signal subspace of rank enhanced covariance matrix $\hat{\mathbf{R}}_d$ is of dimension N . Therefore, there will be N peaks in

the two dimensional MUSIC spectrum corresponding to estimated target locations $(\hat{r}_1, \hat{\theta}_1)$, $(\hat{r}_2, \hat{\theta}_2), \dots, (\hat{r}_N, \hat{\theta}_N)$.

To summarize, the no interaction case proceeds as follows:

1. Using the data model in (5.1) with \mathbf{A} defined as in (5.2), perform L scattering experiments at each operating frequency, f_i , $i = 1, 2, \dots, N$. Observe the snapshot vector, \mathbf{y}_{li} , over the receiver array
2. Estimate the autocovariance matrix $\hat{\mathbf{R}}_d$ using (5.5) and (5.6)
3. Perform an eigenanalysis on $\hat{\mathbf{R}}_d$ to find the noise-subspace projector $\hat{\mathbf{\Pi}}_n$ similar to eigendecomposition of $\hat{\mathbf{R}}$ in (2.12) and (2.13)
4. Carry out a two-dimensional search in the target position space (r, θ) . For each point (r_k, θ_k) on a predefined range and angle grid, fill in the locus vector $\mathbf{E}_s(r_k, \theta_k)$ with the scattered field due to an object placed in that location, and calculate the associated value of $P_{MUSIC}(r_k, \theta_k)$ in (5.3)
5. Choose $(\hat{r}_1, \hat{\theta}_1), (\hat{r}_2, \hat{\theta}_2), \dots, (\hat{r}_N, \hat{\theta}_N)$ as the estimates of the target locations at which P_{MUSIC} has its N largest local maxima.

5.3.3 Multiple Object Localization: With Interaction

In this section, we describe multiple object localization using MUSIC when the electromagnetic interactions between objects are completely taken into consideration. This case is in fact a multi-dimensional equivalent of single object detection. We may aggregate all scatterers into one, large scatterer whose electrical characteristics are defined by positions of

individual scatterers. Therefore, the total scattered field observed over the receiver array depends on the location of each individual scatterer. Since this case can be modeled with an equivalent single scatterer problem when we account for the multiple scattering effects, signal coherence will not be a problem.

For object localization, then, we form the following MUSIC spectrum:

$$P_{MUSIC}(r_1, \theta_1, r_2, \theta_2, \dots, r_N, \theta_N) = \frac{\mathbf{E}_s(\mathbf{r}_1, \mathbf{r}_2, \dots, \mathbf{r}_N)^H \mathbf{E}_s(\mathbf{r}_1, \mathbf{r}_2, \dots, \mathbf{r}_N)}{\mathbf{E}_s(\mathbf{r}_1, \mathbf{r}_2, \dots, \mathbf{r}_N)^H \hat{\mathbf{\Pi}}_n \mathbf{E}_s(\mathbf{r}_1, \mathbf{r}_2, \dots, \mathbf{r}_N)} \quad (5.7)$$

where the locus vector $\mathbf{E}_s(\mathbf{r}_1, \mathbf{r}_2, \dots, \mathbf{r}_N)$ denotes the total scattered field due to objects located at \mathbf{r}_i , $i = 1, 2, \dots, N$. The locus vector $\mathbf{E}_s(\mathbf{r}_1, \mathbf{r}_2, \dots, \mathbf{r}_N)$ can be efficiently filled by using the recursive T-matrix algorithm [16, 17, 33]. In order to find the positions of the objects, then, we perform a multi-dimensional search in location space of all objects, $(r_1, \theta_1), (r_2, \theta_2), \dots, (r_N, \theta_N)$. The coordinates $(\hat{r}_1, \hat{\theta}_1), (\hat{r}_2, \hat{\theta}_2), \dots, (\hat{r}_N, \hat{\theta}_N)$ at which the spectrum (5.7) reaches its maximum give us the estimated target locations.

The computational complexity of this approach is considerably larger than the no interaction case because of two interrelated reasons: repeated use of the forward scattering model many times for the $2N$ -dimensional search, and the extra cost of taking electromagnetic interactions into account in the exact forward model. To keep the computational load at reasonable levels, we used the recursive T-matrix algorithm given in Section 3.2 to calculate the scattered fields due to multiple objects. To further reduce the computational load, we used an efficient search routine based on steepest descent [71] with variable step-size that

quickly converges, typically in 7-10 iterations for problems of interest, to the estimated target locations. Once this routine converges to the general target area, however, we switched to a simplex search routine to save the cost of gradient calculations. This switch is needed since it takes almost the same number of iterations for a steepest descent based search and a simplex search to give a stable answer, and the per-iteration cost of the simplex search is far cheaper than that of the steepest descent based search.

To summarize, the multiple object detection with electromagnetic interaction case proceeds as follows:

1. Using the data model in (5.1), perform L scattering experiments. Observe the snapshot vector, \mathbf{y}_l , over the receiver array
2. Estimate the autocovariance matrix $\hat{\mathbf{R}}$ using (2.11)
3. Perform an eigenanalysis on $\hat{\mathbf{R}}$ to find the noise-subspace projector $\hat{\mathbf{\Pi}}_n$ using (2.12) and (2.13)
4. Carry out a $2N$ -dimensional search in the position space $\{(r_1, \theta_1), (r_2, \theta_2), \dots, (r_N, \theta_N)\}$ of all targets. For each point $\{(r_{1k}, \theta_{1k}), (r_{2k}, \theta_{2k}), \dots, (r_{Nk}, \theta_{Nk})\}$ during the search, fill in the locus vector $\mathbf{E}_s(\mathbf{r}_{1k}, \mathbf{r}_{2k}, \dots, \mathbf{r}_{Nk})$ with the scattered field due to objects placed at that point using the recursive T-matrix algorithm, and calculate the associated value of $P_{MUSIC}(r_{1k}, \theta_{1k}, r_{2k}, \theta_{2k}, \dots, r_{Nk}, \theta_{Nk})$ in (5.7)
5. Choose $(\hat{r}_1, \hat{\theta}_1), (\hat{r}_2, \hat{\theta}_2), \dots, (\hat{r}_N, \hat{\theta}_N)$ as the estimates of the target locations at which P_{MUSIC} is maximized.

5.4 Cramér-Rao Performance Bounds on Object Localization

The Cramer-Rao Bound (CRB) [72] provides very valuable information about the lower limit for the variance of any unbiased estimator. In order to find the CRB, however, one needs a closed form expression for the log-likelihood function. In this section, we will extend the results in [49] to find the Cramér-Rao bounds for the near field, multiple object detection geometries. Since the additive noise in (5.1) is white and Gaussian distributed, the log-likelihood function can be written as [49]:

$$\ln \mathcal{L} = \text{constant} - 2ML \ln \sigma - \frac{1}{\sigma^2} \sum_{l=1}^L [\mathbf{y} - \mathbf{A}\mathbf{x}]^H [\mathbf{y} - \mathbf{A}\mathbf{x}] \quad (5.8)$$

where σ^2 is the noise variance, M is the number of receivers and L is the number of data vectors used for estimating the covariance matrix $\hat{\mathbf{R}}$ in (2.11).

Given the log-likelihood function, the Fisher Information Matrix (FIM) can be written as:

$$J = E\{\psi\psi^T\} \quad (5.9)$$

where $\psi = [\frac{\partial \ln \mathcal{L}}{\partial r_1} \frac{\partial \ln \mathcal{L}}{\partial \theta_1} \dots \frac{\partial \ln \mathcal{L}}{\partial r_N} \frac{\partial \ln \mathcal{L}}{\partial \theta_N}]^T$. The FIM is then expressed in matrix form as:

$$J = \begin{bmatrix} \Gamma_{r_1 r_1} & \Gamma_{r_1 \theta_1} & \cdots & \Gamma_{r_1 r_N} & \Gamma_{r_1 \theta_N} \\ \Gamma_{\theta_1 r_1} & \Gamma_{\theta_1 \theta_1} & \cdots & \Gamma_{\theta_1 r_N} & \Gamma_{\theta_1 \theta_N} \\ \vdots & \vdots & \ddots & \vdots & \vdots \\ \Gamma_{r_N r_1} & \Gamma_{r_N \theta_1} & \cdots & \Gamma_{r_N r_N} & \Gamma_{r_N \theta_N} \\ \Gamma_{\theta_N r_1} & \Gamma_{\theta_N \theta_1} & \cdots & \Gamma_{\theta_N r_N} & \Gamma_{\theta_N \theta_N} \end{bmatrix} \quad (5.10)$$

where $\Gamma_{pq} = E[\frac{\partial^2 \ln \mathcal{L}}{\partial p \partial q}]$, $\{p, q\} = \{r_1, \theta_1, r_2, \theta_2 \dots r_N, \theta_N\}$. The entries of the FIM are [49]:

$$\Gamma_{pq} = \frac{2}{\sigma^2} \sum_{l=1}^L \text{Re}\{\mathbf{x}^H \mathbf{D}_p^H \mathbf{D}_q \mathbf{x}\}, \quad (5.11)$$

where $\mathbf{D}_p = \frac{\partial \mathbf{A}}{\partial p}$ and $\mathbf{D}_q = \frac{\partial \mathbf{A}}{\partial q}$. The columns of matrix \mathbf{A} contain the scattered fields as defined in (5.1), and since the scattered fields are calculated using the recursive T-matrix algorithm, derivatives of \mathbf{A} with respect to object positions, \mathbf{D}_p and \mathbf{D}_q , can be easily obtained (see Appendix D for details). Since \mathbf{x} is constant over L experiments, (5.11) can be further reduced to:

$$\Gamma_{pq} = \frac{2L}{\sigma^2} \text{Re}\{\mathbf{x}^H \mathbf{D}_p^H \mathbf{D}_q \mathbf{x}\}. \quad (5.12)$$

The Cramér-Rao Bound by definition is, then, the inverse of the FIM:

$$\text{CRB}(r_1, \theta_1, \dots, r_N, \theta_N) = J^{-1}. \quad (5.13)$$

The i th diagonal entry in the Cramér-Rao Bound expression in (5.13) gives the Cramér-Rao lower bound for the i th variable in the parameter set $\{r_1, \theta_1, r_2, \theta_2 \dots r_N, \theta_N\}$. In Section 5.5, we will verify the analytical expressions given by (5.13) with Monte-Carlo simulated error variances.

5.5 Examples

In this section, we present numerical examples on localization of multiple objects and verification of Cramér-Rao lower bounds with Monte-Carlo simulations. In order to simplify the scattering phenomenon associated with the detection problem, the targets are modeled as simple, circular objects. The system parameters are kept constant throughout the examples to allow meaningful comparisons. The scattered field due to an incident plane wave (see Fig. 5.2 for incidence angle) is observed along a 33-element, uniform, linear receiver array which spans an aperture of 1.5 m. The sensors are assumed to be ideal, isotropic receivers. Unless otherwise noted, the operating frequency is set to 1.0 GHz. The objects are placed in a lossy, homogeneous background which has the same electrical characteristics as 5% moist San Antonio clay loam ($\epsilon_b = 6\epsilon_0$, $\sigma_b = 5 \times 10^{-2} \frac{\text{S}}{\text{m}}$) at around 1.0 GHz [69]. In all examples the scattering simulations are repeated 250 times to estimate the autocovariance matrices, i.e. $L = 250$ in (2.11), (5.5) and (5.12).

In order to show the performance of the algorithms, we consider two object geometries. In the first case (Fig. 5.2(a)), the objects are located quite far from each other. For this object geometry, due to the lossy background, the interactions between the targets are very weak. In the second case (Fig. 5.2(b)), the objects are located closely, and the electromagnetic interactions between the objects are very strong.

For the simulations, the definition of signal to noise ratio (SNR) is not obvious. In practical problems, SNR is imposed by the nature of the system noise. However, in computer simulations we want to reference the noise power to a fixed quantity that does not change

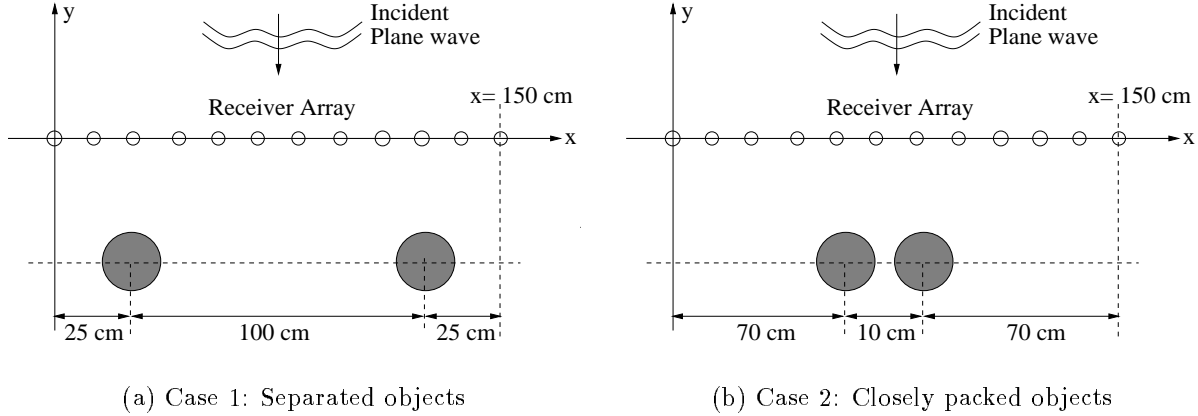


Figure 5.2: Example geometries used in multiple object localization

as the positions of the objects change. For this purpose SNR is referenced to the scattered field strength of a single, cylindrical, metallic object placed at the same depth as the objects, in the same lossy medium. The radius of the reference scatterer is the same as the radii of the targets. With this definition, the noise power is always proportional to the power of reference scattered field, not the power of field scattered from targets which changes as the positions of objects change.

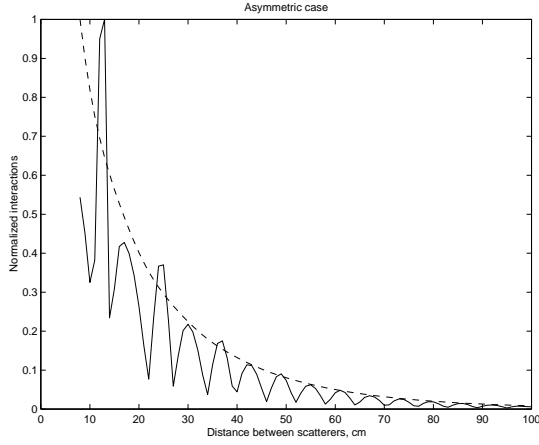
In the examples the scattered field due to multiple objects are calculated using the recursive T-matrix algorithm in [17]. The scattered field due to a single object is calculated using the Mie series given in (5.4).

5.5.1 Multiple Object Localization: No Interaction

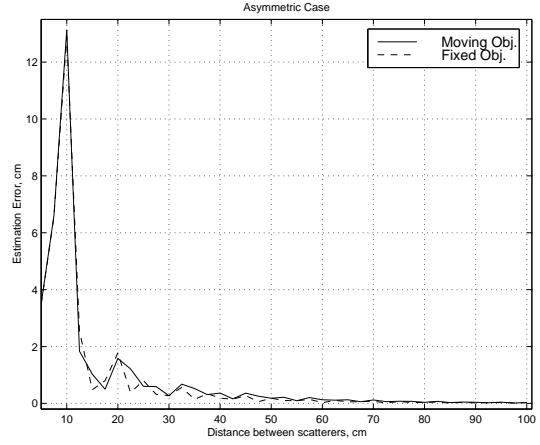
As described in Section 5.3.2, all scatterers are assumed to be scattering the incident plane wave alone. Therefore we used the Mie series as the forward solver. The issue of signal

coherence is solved by using two operating frequencies, 1.0 and 1.2 GHz. The autocovariance matrix at each frequency is estimated using (5.5), and the rank enhanced autocovariance matrix is calculated using (5.6). For a wide range of target locations, we have verified that the autocovariance matrix $\hat{\mathbf{R}}_d$ has two distinct signal eigenvalues that are quite different from the noise eigenvalues. The order of magnitude difference, of course, depends on the signal-to-noise ratio. At the 20 dB SNR level used in this example, the smallest signal eigenvalue is approximately two orders of magnitude larger than the largest noise eigenvalue.

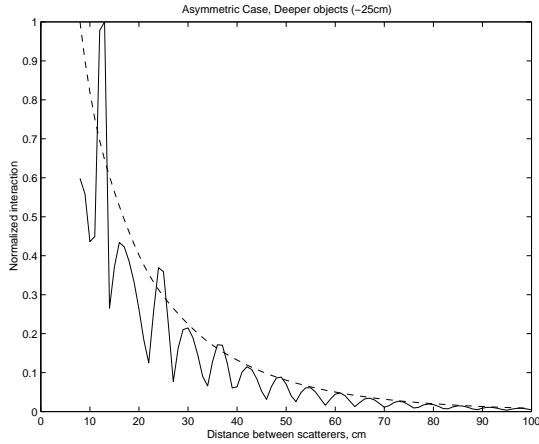
Since ignoring electromagnetic interactions may result in unwanted estimation errors, we investigated the interaction between two extended objects and compared the results with filamentary objects. For this purpose, we increased the distance between scatterers over a range from eight centimeters to one meter by fixing one object's position, and changing the other's. We then plotted the normalized interaction term given by (B.2) for both extended objects and the filamentary objects as depicted in Fig. 5.3(a). The interaction term for filament objects is obtained using the analysis presented in Appendix B. Since the simple interaction term given in the appendix is for a single receiver, for extended objects, the interaction terms are computed over the receiver array and then averaged. It is clear from this figure that for both extended and infinitesimally thin objects, the interaction terms decay very similarly. To indicate the correlation between estimation error and the separation, we plot the estimation error against the distance between scatterers in Fig. 5.3(b). Comparison of Figs. 5.3(a) and (b) reveals the expected result that both estimation errors and interaction terms decay as the objects are located farther apart. We have obtained similar results for



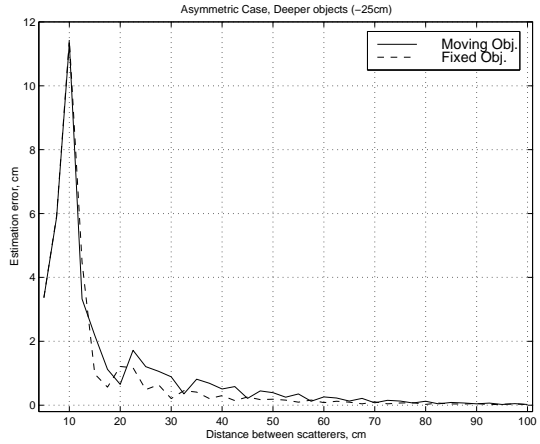
(a) Comparison of normalized interaction terms; solid line extended objects, dashed line filament objects, objects 15 cm away from the array



(b) Estimation error vs. separation for no interaction case, objects 15 cm away from the array



(c) Same as (a), objects 25 cm away from the array



(d) Same as (b), objects 25 cm away from the array

Figure 5.3: Electromagnetic interaction between scatterers, and its effect on estimated object coordinates when the objects are 15 cm away from the receiver array (top plots) and 25 cm away (bottom plots)

other cases where the objects are located deeper. Figs. 5.3(c) and (d) show the same results as Figs. 5.3(a) and (b) when the objects are 25 cm away from the receiver array. This indicates that one may use this simple interaction criterion to decide whether the no-interaction case would result in acceptable estimation errors.

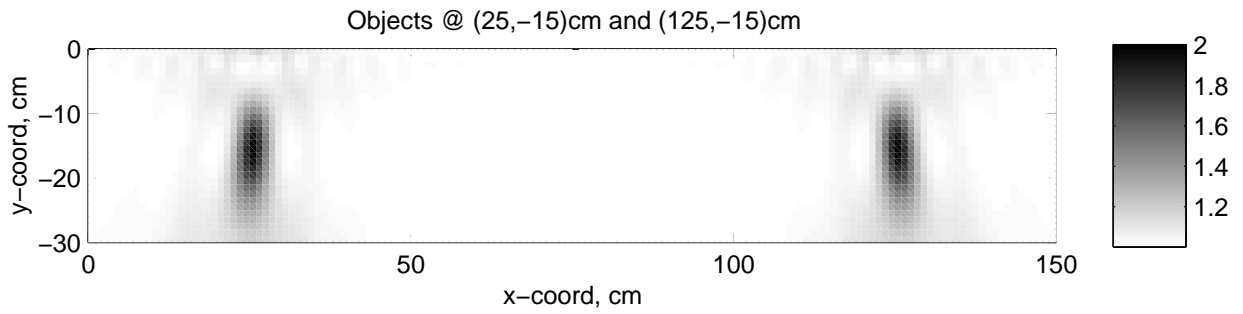


Figure 5.4: Localization of two targets located 1 meter apart, electromagnetic interactions are ignored

We then form the MUSIC spectrum in (5.3) for well separated objects, as shown in Fig. 5.4. As the figure depicts, the target locations are indicated by two peaks that are easy to distinguish from the background. Figs. 5.3(a) and (b) depict that when the objects are 1 meter apart, the interaction becomes insignificant, and the estimation errors are very small. The spectrum for the closely packed object case is shown in Fig. 5.5. It is clear from the figure that the no interaction approach fails for this case. This is expected, since the no interaction model ignores the multiscattering effects that are very strong for closely spaced scatterers. Indeed, as observed from Figs. 5.3(a) and (b), both the interaction term and the estimation error are quite large when the objects are 10 cm apart.

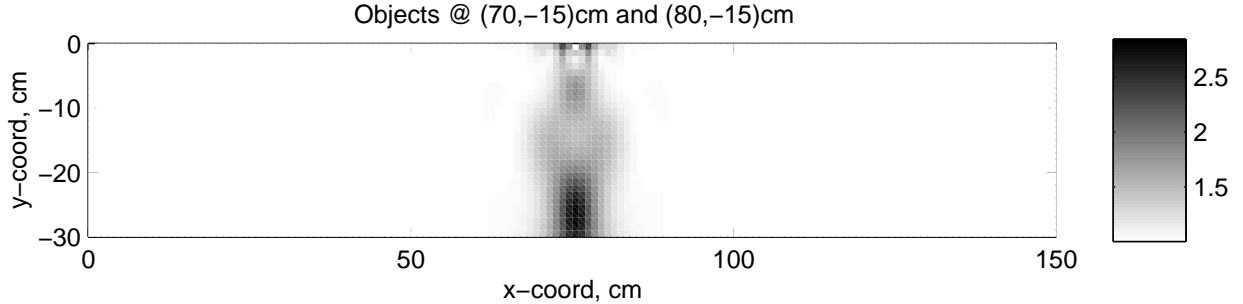


Figure 5.5: Localization fails when the target centers are 10cm apart in the no interaction case

5.5.2 Multiple Object Localization: With Interaction

We have applied the algorithm given in Section 5.3.3 to localize the targets for the two geometries: well separated and closely spaced objects. The signal to noise ratio was fixed at 20 dB and the autocovariance matrix, and the projection operator onto the noise subspace were calculated.

To determine the positions of the two targets, we searched for the maximum of the spectrum $P_{MUSIC}(r_1, \theta_1, r_2, \theta_2)$ given by (5.7) in $(r_1, \theta_1, r_2, \theta_2)$ space. To find this maximum we use a steepest descent algorithm [71] with variable step sizes in x and y -directions. We have chosen a different step size in x and y -directions since the rate of convergence in the y -direction is significantly slower than that in the x -direction. The difference in the convergence rates in x and y -directions stems from the fact that the spectrum in (5.7) changes more drastically in x -direction than it does in y -direction, and therefore, a larger step size in y -direction is needed to balance the convergence. At each iteration of the steepest descent, we search for new step sizes in x and y -directions that maximize the spectrum most. We

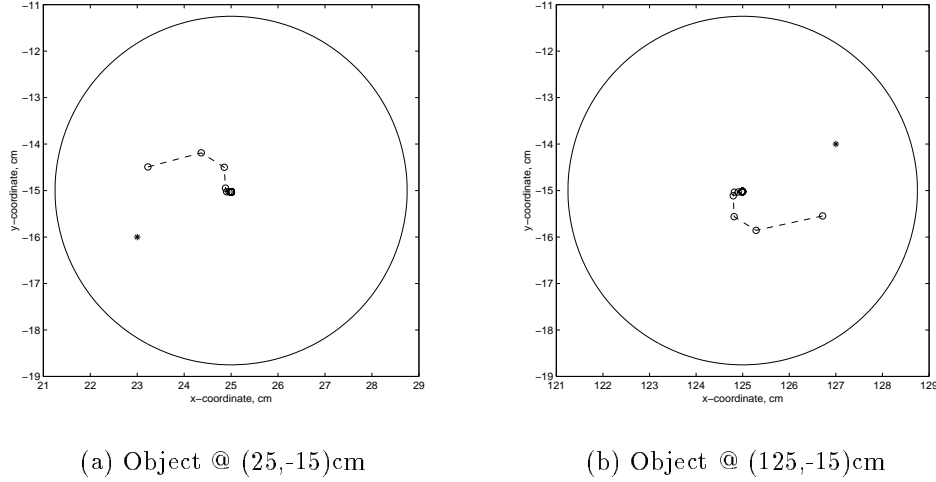


Figure 5.6: Convergence of four-dimensional search into the true object coordinates when the objects are 1 meter apart, *'s indicate the initial guess, and the large circle indicates the support of the objects

observed that this approach can quickly converge to the general maximum area (in around 7-10 iterations). However, after the initial quick convergence, many iterations are required to locate the precise maximum point. Therefore, after 7 or 10 iterations of steepest descent, we switched to a simplex search [73], and achieved rapid convergence almost as quickly as the steepest descent.

Fig. 5.6 shows the intermediate object positions at each iteration during the multi-dimensional search. The objects are located one meter apart, and the initial guesses are denoted with *'s. Although not clear from this figure, as the number of iterations increase, the location estimates get closer to the true estimates at $(25, -15)$ and $(125, -15)$ cm. Fig. 5.7 shows the object positions at each iteration during the simplex search when the objects are

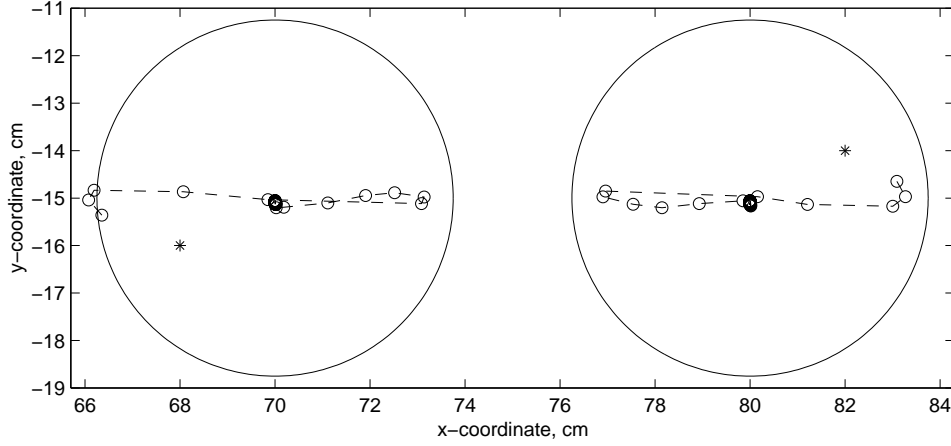


Figure 5.7: Convergence of four-dimensional search into the true object coordinates when the objects are 10 cm apart. *'s indicate the initial guess, and large circles indicate the support of the objects

closely spaced. The distance between the targets for this case is 10 cm. Again the initial guesses are indicated with *'s, and as the number of iterations increase, the location estimates get closer to the true estimates at $(70, -15)$ and $(80, -15)$ cm.

5.5.3 Verification of Cramér-Rao bounds

In this section, we will compare the analytical Cramér-Rao Bound results obtained in Section 5.4 with the Monte-Carlo simulated error variances. For this purpose, the algorithms described in Sections 5.3.1 and 5.3.3 were run 500 times at each signal to noise ratio. For each Monte-Carlo simulation, the multi-dimensional search routine requires initial values for the positions of the targets. Thus, to supply the algorithm with an initial value, we used the subarray processing described in [3]. The subarray processing can efficiently estimate the object locations, but it is less accurate than the matched field processing. Once we

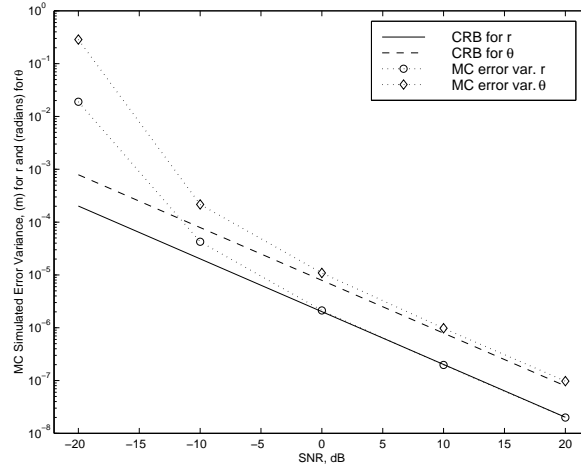


Figure 5.8: Comparison of analytical CRB with Monte-Carlo simulations for single object geometry given in Fig 5.1(a)

initialize the object positions with subarray processing, we perform the multi-dimensional search described in the previous section. The position vector maximizing the spectrum is declared as the position estimate and the error variances are calculated from the estimates.

Fig. 5.8 shows the comparison of analytical CRB calculated for a single object using (5.13) with 500 Monte-Carlo simulations of the algorithm described in Section 5.3.1. The solid line is the CRB for the radial position of the object, measured in squared meters. The dashed line denotes the CRB for the angular position, measured in squared radians. The radial and angular positions are referenced to the center point of the array. Monte-Carlo simulated error variances for range and bearing variables are shown on the same plot with \circ and \diamond symbols, respectively.

Fig. 5.9 compares the Cramér-Rao bounds with simulated error variances for multiple object geometries of Fig. 5.2 using the algorithm of Section 5.3.3. Fig. 5.9(a) shows the comparison for two objects located one meter from each other, and Fig. 5.9(b) show the

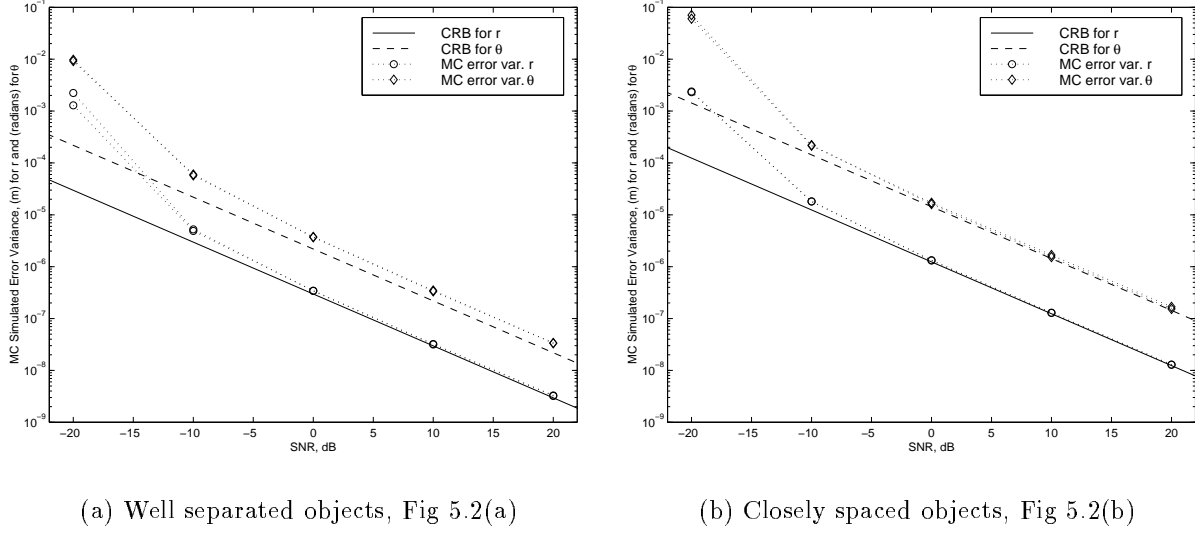


Figure 5.9: Comparison of analytical CRB with Monte-Carlo simulations for multiple object geometries given in Fig. 5.2

comparison when the objects are 10 centimeters apart. Again, the solid and dashed lines are the CRBs for radial and angular positions of the objects, respectively. The range variables have the unit of squared meters, and the bearing variables have the unit of squared radians. As before, both coordinate variables are defined with respect to the center point of the array. The symbols \circ and \diamond show the Monte-Carlo simulated error variances for the range and bearing variables, respectively. For this case, since there are two targets present in the region, there are two symbols at each SNR value. The problem geometry is symmetric, and thus one would expect that the error variances should be the same. Indeed, for analytical Cramér-Rao bounds calculated from (5.13), the bounds for coordinates of both objects are the same. For the simulated error variances, however, we can notice different values for the range variables in Fig. 5.9(a) and the bearing variables in Fig. 5.9(b). The difference

in simulated variances is more pronounced for low signal to noise ratios, which, we believe, implies that more Monte-Carlo simulations are needed at those SNR values.

In both Fig. 5.8 and Fig. 5.9, we observe that the simulated error variances approach the lower limit provided from the Cramér-Rao bounds as the signal to noise ratio increases. This is expected by the results reported in [49] which states that MUSIC is an efficient estimator for large SNR values. The results presented here, therefore, reveals the fact that at high signal to noise ratios MUSIC is an efficient estimator for near field object localization problems, too.

5.6 Summary

In this chapter we presented a matched field based high resolution array processing technique for localization of near field targets. The algorithm is presented in three parts: single object localization, multiple object localization ignoring the interactions between objects, and multiple object localization taking multiple scattering into account. When the interactions are ignored, the computational load is alleviated since the electromagnetic model is simpler Mie series scattering and a two-dimensional search in parameter space suffices to localize all objects. The drawbacks, on the other hand, are the necessity to take care of the coherent signal issue, and the failure to resolve and localize closely spaced targets. When the electromagnetic interactions are accounted for, these drawbacks are remedied, but the computational load due to multi-dimensional search, and complex, multiple scattering forward model increases considerably.

We have also calculated the analytical Cramér-Rao Bound expressions for coordinates of multiple objects when the interactions are taken into consideration. These lower bounds are then verified with Monte-Carlo simulated error variances. We have shown that as the signal to noise ratio increases, simulated error variances approach the lower limit set by the Cramér-Rao bounds.

Chapter 6

Contributions, Future Work, and Conclusions

We begin this chapter by reviewing the contributions presented in this thesis in the area of forward electromagnetic scattering, and array processing-based object localization algorithms. In Section 6.2, we discuss extensions and future research opportunities based on the ideas presented in the thesis. Finally, in Section 6.3, we will draw conclusions from this work.

6.1 Contributions

The research presented in this thesis is comprised of two distinct parts. In the first part, Chapter 3, we dealt with the electromagnetic forward scattering problem to obtain an efficient, flexible, and stable algorithm. In the second part, Chapters 4 and 5, we introduced two

signal processing algorithms based on high resolution array processing. The second part of the thesis extensively used the efficient forward solver developed in the first part. However, the algorithms developed in the second part are independent of the forward solver, and any other forward solver can be used instead of the recursive algorithm presented in Chapter 3.

We will, therefore, present the contributions of this thesis in two categories.

6.1.1 Forward Scattering

Motivated by the ground penetrating radar type measurements, for the forward scattering, we wanted to solve scattering problems in the near field for a uniformly spaced, linear array. The main difference between the recursive T-matrices reported earlier [14, 15, 23–27] and the work presented here is that this previous work was interested in obtaining the scattered fields in the far field, whereas we are interested in the scattered fields in the near field. As a result of this difference in the position of observation points, we presented two new ideas in order to make the recursive T-matrix algorithm a useful tool for near field measurements.

- Because of the requirements on the loci of observation points imposed by harmonic expansions of the fields (2.7), the scattering origin relative to scatterers and the receivers should be carefully selected. We have derived expressions for valid scattering origin regions given a linear receiver array and scatterer positions. We have pointed out that the trivial solution for this problem would impose placing the scattering origin at the infinity. However, this choice would imply the use of infinitely large harmonics in the

field expansions. Therefore, we defined an optimum scattering origin in the valid scattering origin region, that minimizes the number of harmonics in the field expansions, thereby minimizing the computational complexity.

- The optimum choice of the scattering origin, however, may result in convergence problems in a particular addition formula used in the recursive T-matrix algorithm as discussed in Section 3.2.2. In order to circumvent the convergence issue in the addition formula, while using the optimum scattering origin, we introduced a modification the recursion equations in Section 3.2.3. The modified algorithm is shown to have the same order of computational complexity as the original algorithm.
- In addition to these two contributions in the near field, we have also developed an alternative tessellation scheme for metallic scatterers in Section 3.1. The reported work in the literature [24, 26, 27, 42] tessellated metallic objects by decomposing the surface of the scatterer into small strips and patches. The Method of Moment (MoM) was then employed to find the individual T-matrices of these strips and patches. We, on the other hand, suggested using small metallic cylinders to decompose the scatterer surface. We have shown with numerous examples that the alternative tessellation scheme also results in highly accurate solutions. By using cylinders, the need to use MoM to find individual T-matrices is eliminated since we can use the closed form harmonic expansions to find the individual T matrices of the cylinders. Furthermore, for problems involving both metallic and dielectric objects, only one type of tessellation unit, i.e. a cylinder, can be used to decompose all objects. Without this contribution,

metallic objects would have to be tessellated with strips, whereas dielectric objects would have to be tessellated with cylinders.

6.1.2 Detection and Localization

The localization problems of interest in this thesis assume some level of knowledge of the targets we are trying to detect. For example, in land-mine remediation, and hazardous waste drum recovery, we generally know the shapes and electrical properties of the targets. Therefore, we can use the object-based framework to parameterize the detection problem. The inherent array structure of the measurement geometry coupled with the object-based approach suggested that high resolution array processing would be well suited for the near field detection problem. We have developed two algorithms for this purpose: quick and efficient subarray processing, and more computationally demanding matched field processing.

- This work is one of the first in the subsurface object localization area that uses high resolution array processing. The only previous work in this area that has been brought to our attention is a work by group of European researchers [43]. The work in [43] concentrates on polarimetric radar imaging with the MUSIC algorithm. Our work is different in that we took an object-based approach rather than an imaging approach. Therefore, it is safe to say that the localization algorithms presented in this thesis are the first ones that detect and localize subsurface, near field objects using the MUSIC algorithm.

- The subarray processing divides the receiver array into subarrays so that the scattered fields impinging on each subarray is locally planar. Then using the conventional MUSIC algorithm, we determined the directions of arrivals (DOAs) of the planar surfaces, and triangulating these DOAs we estimate the target locations.
- For single target localization, all triangulated DOAs intersect at a very compact region in the vicinity of the target. For multiple targets, however, the crossings can be quite complex and dispersed. The target regions can still be recognized by a large number of crossings in a small region, but those dense crossing regions should be discriminated from background crossings. For this purpose, we modeled the crossings in the target and background region with two Poisson distributions with two rate parameters: the large rate parameter indicating the target regions, and the small rate parameter indicating the background crossings. The Poisson model provided a solid groundwork for a detailed statistical analysis. We introduced a hypothesis test, and defined probabilities of detection and false alarm.
- The matched field processing makes use of the spatial complexities of the fields to localize the targets. The direction vector of the plane wave MUSIC is replaced by the locus vector which contains the scattered fields observed along the receiver array. Since the matched field processing requires calculation of scattered fields repetitively, it is computationally demanding. In general, in order to localize N targets, a $2N$ -dimensional search in range and bearing space of all targets is required. However, if the targets are far from each other, we may ignore the electromagnetic interaction

between them, and reduce the $2N$ -dimensional search to a 2-dimensional search, at the expense of incurring a signal coherence problem.

- We have also addressed the signal coherence problem when multiple scatterers independently scatter the incident plane wave. For this purpose, we employed frequency diversity, Section 5.3.2, which obtains a decorrelated autocovariance by using scattering experiments at multiple frequencies.
- Furthermore, we have derived analytical Cramér-Rao Bound expressions for multiple object, near field object localization. These analytical bounds agreed quite well with the Monte-Carlo simulated error variances. Our simulation results are also a multiple dimensional verification of those in [49] which reports that MUSIC estimator is efficient for the large signal to noise ratio operating regimes.

6.2 Future Work

Even though the work presented in this thesis provides interesting ideas about subsurface object detection, the issues we dealt with suggest numerous avenues for possible extensions and future work. In this section, we provide an overview of such ideas in order to shape the future of the work presented in the thesis.

6.2.1 Forward Scattering Model

In the area of the forward scattering model, the following provides a list of possible research directions:

- As shown in Appendix A, the translation matrices α and β are inherently Toeplitz matrices. Additional efficiency and speed up in the recursive T-matrix algorithms might be obtained by exploiting the Toeplitz structure of these translation matrices.
- While taking the derivatives of the scattered fields using recursive T-matrix methods, we noticed that the translation matrices show certain structures that can be exploited in future work. For example, the n th order derivative of β with respect to its argument can be written in terms of other matrices obtained by shifting rows of β up and down.

$$\frac{\partial^n \beta}{\partial z^n} = \frac{1}{2^n} \sum_{i=0}^n \binom{n}{i} (-1)^i \beta^{\{-n+2i\}}, \quad (6.1)$$

where $\beta^{\{-n+2i\}}$ is obtained by shifting the rows of β up (resp. down) if the superscript $-n+2i$ is positive (resp. negative).

- The recursive T-matrix algorithm in its present form cannot take the air-earth interface into account. It would be extremely useful to alter the recursive algorithm such that air-earth interface is included in the formulation. In fact, [74] reports a T-matrix approach to find the scattered field from buried inhomogeneities. Kristensson and Ström's work may form a basis to extend the recursive T-matrix algorithm to layered media.

- It would also be beneficial to extend the results of the modified T-matrix algorithm to three dimensional geometries. Chew et al. [23] reported a recursive T-matrix algorithm in three-dimensions by tessellating objects into small spheres. As with the two-dimensional case, however, computation of near field quantities directly from [23] might rekindle the convergence problem described in Section 3.2.2. Thus, extension of the modified algorithm to include near field scattering in three-dimensions would be valuable.

6.2.2 Detection and Localization

To improve detection and localization algorithms, the following items will be considered for the future:

- Since the detection algorithms presented are model based, sensitivity to the model parameters will be crucial to estimate the performance of the algorithms under different conditions. Therefore, we intend to analyze the sensitivity of localization performance to object radius, object shape, and object and background material properties.
- In Section 4.4 we presented an example on detection performance of SAP for randomly located objects. We noticed that the uniform distribution of random object locations resulted in non-uniform distribution of relative distance between them. The non-uniform distribution of relative distance, in fact, favored smaller distances as depicted in Fig 4.11. As a result, SAP performed badly in this example. In the future, we would like to repeat the same experiment by enforcing the distribution of relative distance to

be uniform.

- In [49], the authors derive a closed form error variance of MUSIC estimator. It would be appropriate to perform a similar analysis for multiple object, near field MUSIC to obtain the error variance explicitly.
- MFP for multiple objects will also require that the number of targets buried under the receiver array is known a priori. For our preliminary work in MFP, we assume that this information is provided to us. However, in the future, we would like to estimate the number of objects in the region of interest by using signal processing techniques like Akaike's information theoretic criterion [44, 45] or the Minimum Description Length (MDL) criterion [46, 47].
- The last extension we would like to suggest will be the generalization of the linear array used in the algorithms into a two-dimensional array. In order to achieve this goal, the last item in Section 6.2.1 will have to be realized to calculate the scattered fields from three-dimensional objects.

6.3 Closing

In this thesis, we have considered two complementary sides of object localization. In the first part, we have developed an efficient, flexible, and stable recursive T-matrix algorithm for electromagnetic forward scattering. This algorithm allows us to determine the scattered field over a linear receiver array when scatterers are located relatively close to the array.

Furthermore, we demonstrated that conducting scatterers tessellated with small metallic cylinders along their perimeters can be used in the recursive T-matrix algorithms.

In the second part, we developed two localization algorithms that used the forward models developed in the first part. The algorithms developed in the second part are based on a high resolution array processing technique, the multiple signal classification (MUSIC) algorithm. Of the two algorithms developed, subarray processing can localize the targets very efficiently. The other algorithm, the matched field processing, localizes targets very accurately at the expense of increased computational complexity. We have shown that the Monte-Carlo simulations agree quite well with the analytical Cramér-Rao Bound expressions, and that the MUSIC estimator becomes efficient as the signal to noise ratio increases.

While we believe that the contributions in this thesis indicate improvements in the near field object localization problems, it is also true that the results obtained here open new avenues for further research in the same area.

Appendix A

Translation Matrices

Both translation matrices $\boldsymbol{\beta}$ and $\boldsymbol{\alpha}$ have the same form, except that they contain Bessel functions and Hankel functions, respectively. Here, we briefly show their structure, and how they are constructed efficiently. For detailed analysis, interested readers are referred to [33, 58]. Further information can be obtained by referring to “addition theorem” sections of books on Bessel functions, e.g. [62]. Both matrices translate the wavefields in the direction indicated by their subscripts. For example, $\boldsymbol{\beta}_{p,q}$ translates the standing waves from the q th coordinate system to the p th coordinate system. Similarly, $\boldsymbol{\alpha}_{p,q}$ translates the traveling waves from the q th coordinate system to the p th coordinate system. The direction of translation is denoted by the vector $\mathbf{a}_{p,q} = \mathbf{a}_q - \mathbf{a}_p$, where \mathbf{a}_q and \mathbf{a}_p are vectors from the scattering origin to the q th and the p th local origin, respectively. The matrices $\boldsymbol{\beta}_{p,q}$ and $\boldsymbol{\alpha}_{p,q}$ are functions of this vector, $\mathbf{a}_{p,q} = a_{pq}\mathcal{L}\theta_{pq}$. Then, the (m,n) th entry of $\boldsymbol{\beta}_{p,q}$ and $\boldsymbol{\alpha}_{p,q}$ can be written as:

$$\left[\boldsymbol{\beta}_{p,q}\right]_{m,n} = J_{m-n}(ka_{pq})e^{-j(m-n)\theta_{pq}} \quad (\text{A.1})$$

and

$$[\boldsymbol{\alpha}_{p,q}]_{m,n} = H_{m-n}^{(2)}(ka_{pq})e^{-j(m-n)\theta_{pq}} \quad (\text{A.2})$$

where $J_{m-n}(\cdot)$ is the Bessel function of order $(m-n)$, $H_{m-n}^{(2)}(\cdot)$ is the Hankel function of second kind of order $(m-n)$, k is the wavenumber in the medium of propagation, and $j = \sqrt{-1}$.

Assuming that the fields in the p th coordinate system are expanded with M harmonics, and those in the q th coordinate system are expanded with N harmonics. The resulting $\boldsymbol{\beta}_{p,q}$ and $\boldsymbol{\alpha}_{p,q}$ matrices would be $(2M+1) \times (2N+1)$, since both M and N run from negative to positive values. Some entries in these matrices are repeated. Therefore, instead of generating each entry one by one, we can develop a more efficient strategy. We noticed that the indices of these matrices at each entry are:

$$\begin{bmatrix} 1,1 & 1,2 & 1,3 & \cdots & 1,2N+1 \\ 2,1 & 2,2 & 2,3 & \cdots & 2,2N+1 \\ 3,1 & 3,1 & 3,3 & \cdots & 3,2N+1 \\ \vdots & \vdots & \vdots & \ddots & \vdots \\ 2M+1,1 & 2M+1,2 & 2M+1,3 & \cdots & 2M+1,2N+1 \end{bmatrix}. \quad (\text{A.3})$$

Since (A.1) and (A.2) imply that at the (m,n) th entry, Bessel and Hankel functions are of order $(m-n)$, we write the difference of indices at each entry:

$$\begin{bmatrix}
0 & -1 & -2 & \cdots & -2N \\
1 & 0 & -1 & \cdots & -2N + 1 \\
2 & 1 & 0 & \cdots & -2N + 2 \\
\vdots & \vdots & \vdots & \ddots & \vdots \\
2M & 2M - 1 & 2M - 2 & \cdots & -2N + 2M
\end{bmatrix} \tag{A.4}$$

which clearly shows that consecutive rows of the translation matrices differ only by leftmost and rightmost entries. Thus, instead of forming each entry one by one, we form a vector using (A.1) and (A.2) with $(m - n)$ running from $-2N$ to $2M$. Then, as suggested by (A.4), we take $1 \times (2N + 1)$ sub-vectors of this $1 \times (2N + 2M + 1)$ vector, and form every row of the translation matrices by shifting the sub-vector $(2M + 1)$ times.

Appendix B

Bound on Electromagnetic Interactions

In this appendix, we derive the interaction terms between two infinitesimally thin scatterers. To quantify the relative difference between the exact scattered field at a receiver (i.e. the field obtained when all electromagnetic interactions are taken into account) and the field computed when multiple interactions are ignored, we define an interaction term as:

$$\delta_1 = \frac{E_{s1}^{(2)} - E_{s1}}{E_{s1}}, \quad (\text{B.1})$$

where $E_{s1}^{(2)}$ is the scattered field due to the first object in the presence of the second object, and E_{s1} is the scattered field from the first object when there are no other scatterers around. The field that takes the electromagnetic interactions into account can be computed exactly using the T-matrix algorithm, or using the simplified expressions in this appendix. The

normalized interaction term is then defined as:

$$\delta = \frac{|\delta_1|}{\max\{|\delta_1|\}}. \quad (\text{B.2})$$

Using the definition of the normalized interaction in (B.2), we calculate the electromagnetic interactions between two infinitesimal scatterers here, and then compare these simple interaction terms with those of extended objects in Section 5.5.1.

First we derive the scattered field from two filamentary objects separated by a distance d , when they are excited with a plane wave, $e^{j\mathbf{k}\cdot\mathbf{r}}$. With a simple approach, schematically shown in Fig. B.1, we account for the multiple scattering between these objects iteratively by assuming that there is no interaction between them. Consider the scattered field radiated by the first object. The field scattered from the first object due to the plane wave is obtained by setting $n = 0$ in (5.4):

$$E_{s1} = c_0 H_0^{(2)}(kr) \quad (\text{B.3})$$

where c_0 depends on the object radius, and r is the distance between the scatterer and

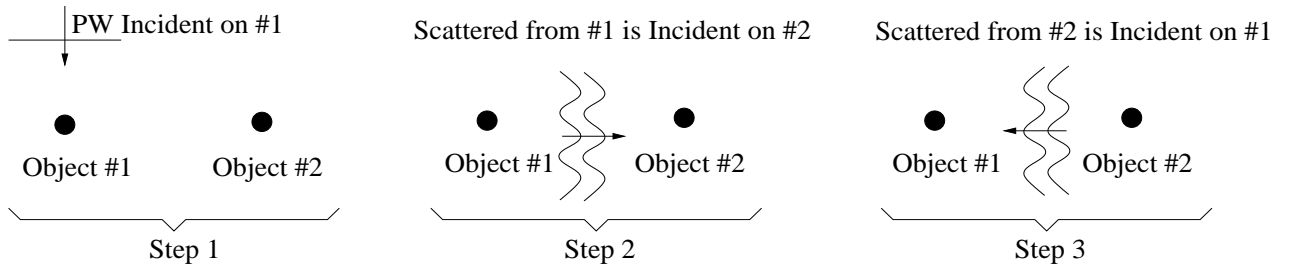


Figure B.1: Finding the scattered field due to a filamentary object by incorporating the electromagnetic interactions between two scatterers step by step. Steps 2 and 3 are repeated infinitely many times successively to account for all interactions

the observation point. When the field in (B.3) arrives at the location of the second object,

it becomes $c_0 H_0^{(2)}(kd)$, where d is the distance between them. Then, still assuming no interaction, we use $c_0 H_0^{(2)}(kd)$ as incident field on the second object, and find the scattered field due to the wave scattered from the first object as:

$$E_{s12} = d_0 H_0^{(2)}(kr) \quad (\text{B.4})$$

where $d_0 = c_0 [c_0 H_0^{(2)}(kd)]$. When the field in (B.4) arrives at the location of the first object, it becomes $d_0 H_0^{(2)}(kd)$. Using this as the incident field on the first object, we calculate the third term as:

$$E_{s121} = e_0 H_0^{(2)}(kr)$$

where $e_0 = c_0 [d_0 H_0^{(2)}(kd)]$. By carrying no-interaction scattered fields between scatterers in this manner, the scattered field due to the first object, in the presence of the second is given in the form of an infinite sum:

$$E_{s1}^{(2)} = E_{s1} + E_{s12} + E_{s121} + E_{s1212} + \dots,$$

or

$$E_{s1}^{(2)} = \sum c_0 \left\{ 1 + c_0 H_0^{(2)}(kd) + [c_0 H_0^{(2)}(kd)]^2 + [c_0 H_0^{(2)}(kd)]^3 + \dots \right\} H_0^{(2)}(kr). \quad (\text{B.5})$$

Using (B.3) and (B.5) in (B.1) the interaction term can be expressed as:

$$\delta_1 = \sum c_0 H_0^{(2)}(kd) + [c_0 H_0^{(2)}(kd)]^2 + [c_0 H_0^{(2)}(kd)]^3 + \dots,$$

which can be written concisely as:

$$\delta_1 = \frac{c_0 H_0^{(2)}(kd)}{1 - c_0 H_0^{(2)}(kd)}. \quad (\text{B.6})$$

Normalized interaction term δ signifies the similarity between no-interaction and with-interaction fields can be easily obtained using (B.6) in (B.2). When $\delta \rightarrow 0$, it means that the interaction between scatterers is small, and a large δ indicates that the interaction between scatterers is considerable.

Appendix C

A Simplified Proof for Frequency Diversity

In this appendix, we will show that under simplifying assumptions the frequency diversity described by (5.5) and (5.6) increases the rank of the autocovariance matrix. Consider the data model:

$$\mathbf{y}_i = \mathbf{s}_i + \mathbf{n}_i \quad (\text{C.1})$$

where \mathbf{s}_i is the noise-free scattered field due to a scatterer at frequency f_i , \mathbf{n}_i is the white, Gaussian noise as before, and \mathbf{y}_i is the observed data vector at frequency f_i , $i = 1, 2, \dots, N$. To simplify the problem, we will assume that the number of scatterers is limited to two ($N = 2$), and the scatterers are infinitesimally thin.

The exact expression for the rank enhanced autocovariance matrix, \mathbf{R}_d is:

$$\mathbf{R}_d = \frac{1}{2} \mathbf{E} \{ \mathbf{y}_1 \mathbf{y}_1^H + \mathbf{y}_2 \mathbf{y}_2^H \} \quad (\text{C.2})$$

which can be written as:

$$\mathbf{R}_d = \frac{1}{2} [\mathbf{s}_1 \mathbf{s}_1^H + \mathbf{s}_2 \mathbf{s}_2^H + 2\sigma^2 \mathbf{I}]. \quad (\text{C.3})$$

For two scatterers, the frequency diversity should ensure that the signal subspace of \mathbf{R}_d is two dimensional. To see the conditions for which the signal subspace of \mathbf{R}_d is two dimensional, we rewrite (C.3) as:

$$\mathbf{R}_d = \underbrace{\frac{1}{2} [\mathbf{s}_1 \mathbf{s}_2] \begin{bmatrix} 1 & 0 \\ 0 & 1 \end{bmatrix}}_{\mathbf{S}} \begin{bmatrix} \mathbf{s}_1^H \\ \mathbf{s}_2^H \end{bmatrix} + \sigma^2 \mathbf{I}. \quad (\text{C.4})$$

For signal subspace of \mathbf{R}_d to be two dimensional, the matrix \mathbf{S} should have rank two which is possible if vectors \mathbf{s}_1 and \mathbf{s}_2 are linearly independent. Since the maximum likelihood estimate of the rank enhanced autocovariance matrix $\hat{\mathbf{R}}_d$ in (5.6) is asymptotically equal to the exact matrix \mathbf{R}_d , the proof for \mathbf{R}_d is valid for $\hat{\mathbf{R}}_d$ for large snapshots, i.e. $L \rightarrow \infty$. In the rest of the appendix, we show that \mathbf{R}_d has a two dimensional signal subspace, by proving that \mathbf{s}_1 and \mathbf{s}_2 are independent.

For this purpose, we show that the scattered fields due to the filament scatterers observed at two points, A and B , in space at two distinct frequencies, f_1 and f_2 , are independent. Thus, the data vectors measured over an array at more than two points will also be independent. The general Mie scattering series given in (5.4), is reduced to the following expressions for filament scatterers:

$$\begin{aligned} E_{s1}^A &= c_0 H_0^{(2)}(k_1 r_A) & E_{s2}^A &= d_0 H_0^{(2)}(k_1 r_A) \\ E_{s1}^B &= c_0 H_0^{(2)}(k_1 r_B) & E_{s2}^B &= d_0 H_0^{(2)}(k_2 r_B) \end{aligned} \quad (\text{C.5})$$

where r_A and r_B denote the observation points, coefficients c_0 and d_0 are dependent on the

frequency and object properties, $H_0^{(2)}(.)$ is the zeroth order outgoing Hankel function, and k_i is the wavenumber at f_i , $i = 1, 2$. We will show that the vectors

$$\mathbf{s}_1 = \begin{bmatrix} E_{s1}^A \\ E_{s1}^B \end{bmatrix} \quad \text{and} \quad \mathbf{s}_2 = \begin{bmatrix} E_{s2}^A \\ E_{s2}^B \end{bmatrix} \quad (\text{C.6})$$

are independent, i.e. equations

$$E_{s1}^A = \alpha E_{s2}^A \quad \text{and} \quad E_{s1}^B = \alpha E_{s2}^B \quad (\text{C.7})$$

cannot be satisfied as long as $f_1 \neq f_2$.

Equations (C.5) and (C.7) imply that:

$$c_0 H_0^{(2)}(k_1 r_A) = \alpha d_0 H_0^{(2)}(k_2 r_A) \quad \text{and} \quad c_0 H_0^{(2)}(k_1 r_B) = \alpha d_0 H_0^{(2)}(k_2 r_B) \quad (\text{C.8})$$

which can be written as

$$\gamma = \frac{\alpha d_0}{c_0} = \frac{H_0^{(2)}(k_1 r_A)}{H_0^{(2)}(k_2 r_A)} = \frac{H_0^{(2)}(k_1 r_B)}{H_0^{(2)}(k_2 r_B)}. \quad (\text{C.9})$$

Properties of Hankel functions require that $|H_0^{(2)}(k_1 r)|$ and $|H_0^{(2)}(k_2 r)|$ are monotonically decreasing, and they do not intersect at any r . These two properties and the fact that the ratio of $H_0^{(2)}(k_1 r)$ to $H_0^{(2)}(k_2 r)$ is not a constant imply that if we choose a γ such that $H_0^{(2)}(k_1 r_A) = \gamma H_0^{(2)}(k_2 r_A)$, then there would be no r_B which satisfies $H_0^{(2)}(k_1 r_B) = \gamma H_0^{(2)}(k_2 r_B)$ unless $k_1 = k_2$ and $\gamma = 1$. Therefore, the vectors given in (C.6) are mutually dependent only when $k_1 = k_2$, i.e. $f_1 = f_2$.

Appendix D

Derivatives of Fields in Recursive T Matrix Algorithm

In this appendix, we will describe the details of differentiating the scattered fields with respect to object coordinates, (r_i, θ_i) , $i = 1, 2, \dots, L$. We will use the variable p to replace r and θ in order not to write similar expressions for both r and θ . For example, $\frac{\partial \psi^{sca}}{\partial p_i}$ would mean both $\frac{\partial \psi^{sca}}{\partial r_i}$ and $\frac{\partial \psi^{sca}}{\partial \theta_i}$.

As described in Chapters 2 and 3, the scattered field in terms of T-matrices can be written as:

$$\psi^{sca}(\underline{r}) = \sum_{i=1}^L \underline{\psi}^T(\underline{r}_i) \mathbf{T}_{i(L)} \boldsymbol{\beta}_{i,0} \underline{a} \quad (\text{D.1})$$

which can be equivalently written by translating the observation point coordinates from local (i th) coordinate system to global coordinate system as:

$$\psi^{sca}(\underline{r}) = \sum_{i=1}^L \underline{\psi}^T(\underline{r}) \boldsymbol{\beta}_{0,i} \mathbf{T}_{i(L)} \boldsymbol{\beta}_{i,0} \underline{a} \quad (\text{D.2})$$

where $\mathbf{T}_{i(L)}$ is the T-matrix of the i th object in the presence of L scatterers. Then, we write the derivative as:

$$\frac{\partial \psi^{sca}}{\partial p_k} = \sum_{i=1}^L \underline{\psi}^T(r) \beta_{0,i} \frac{\partial \mathbf{T}_{i(L)} \beta_{i,0}}{\partial p_k} \underline{a} + \underline{\psi}^T(r) \frac{\partial \beta_{0,k}}{\partial p_k} \mathbf{T}_{k(L)} \beta_{k,0} \underline{a}, \quad (\text{D.3})$$

where $k = 1, 2, \dots, L$.

Using the recursion equations (3.11) and (3.12), we can write $\mathbf{T}_{i(L)}$ as:

$$\mathbf{T}_{L(L)} \beta_{L,0} = \left[\mathbf{I} - \mathbf{T}_{L(1)} \sum_{i'=1}^{L-1} \alpha_{L,i'} \mathbf{T}_{i'(L-1)} \beta_{i',0} \beta_{0,i'} \alpha_{i',L} \right]^{-1} \mathbf{T}_{L(1)} \left[\beta_{L,0} + \sum_{i'=1}^{L-1} \alpha_{L,i'} \mathbf{T}_{i'(L-1)} \beta_{i',0} \right] \quad (\text{D.4})$$

and

$$\mathbf{T}_{i'(L)} \beta_{i',0} = \mathbf{T}_{i'(L-1)} \beta_{i',0} + \mathbf{T}_{i'(L-1)} \beta_{i',0} \beta_{0,i'} \alpha_{i',L} \mathbf{T}_{L(L)} \beta_{L,0}. \quad (\text{D.5})$$

where $i' = 1, 2, L-1$. In these expressions β 's α 's and $\mathbf{T}_{i'(L-1)} \beta$'s are dependent on object positions. The T matrix of a single object, $\mathbf{T}_{L(1)}$, is independent of object locations. To simplify the derivatives, we write (D.4) as:

$$\mathbf{T}_{L(L)} \beta_{L,0} = U^{-1} \mathbf{T}_{L(1)} V,$$

where

$$U = \mathbf{I} - \mathbf{T}_{L(1)} \sum_{i'=1}^{L-1} \alpha_{L,i'} \mathbf{T}_{i'(L-1)} \beta_{i',0} \beta_{0,i'} \alpha_{i',L}$$

and

$$V = \beta_{L,0} + \sum_{i'=1}^{L-1} \alpha_{L,i'} \mathbf{T}_{i'(L-1)} \beta_{i',0}.$$

We then write the derivative of $\mathbf{T}_{L(L)} \beta_{L,0}$ as:

$$\frac{\partial \mathbf{T}_{L(L)} \beta_{L,0}}{\partial p_k} = \frac{\partial U^{-1}}{\partial p_k} \mathbf{T}_{L(1)} V + U^{-1} \mathbf{T}_{L(1)} \frac{\partial V}{\partial p_k}$$

or equivalently:

$$\frac{\partial \mathbf{T}_{L(L)} \boldsymbol{\beta}_{L,0}}{\partial p_k} = U^{-1} \frac{\partial U}{\partial p_k} \mathbf{T}_{L(1)} U^{-1} V + U^{-1} \mathbf{T}_{L(1)} \frac{\partial V}{\partial p_k}.$$

For derivatives of U and V , we have two cases:

1. $k < L$

$$\begin{aligned} \frac{\partial U}{\partial p_k} = & 0 - \mathbf{T}_{L(1)} \left[\sum_{i'=1}^{L-1} \boldsymbol{\alpha}_{L,i'} \frac{\partial \mathbf{T}_{i'(L-1)} \boldsymbol{\beta}_{i',0}}{\partial p_k} \boldsymbol{\beta}_{0,i'} \boldsymbol{\alpha}_{i',L} - \frac{\partial \boldsymbol{\alpha}_{L,k}}{\partial p_k} \mathbf{T}_{k(L-1)} \boldsymbol{\beta}_{k,0} \boldsymbol{\beta}_{0,k} \boldsymbol{\alpha}_{k,L} \right. \\ & \left. - \boldsymbol{\alpha}_{L,k} \mathbf{T}_{k(L-1)} \boldsymbol{\beta}_{k,0} \frac{\partial \boldsymbol{\beta}_{0,k}}{\partial p_k} \boldsymbol{\alpha}_{k,L} - \boldsymbol{\alpha}_{L,k} \mathbf{T}_{k(L-1)} \boldsymbol{\beta}_{k,0} \boldsymbol{\beta}_{0,k} \frac{\partial \boldsymbol{\alpha}_{k,L}}{\partial p_k} \right] \end{aligned}$$

$$\frac{\partial V}{\partial p_k} = 0 + \sum_{i'=1}^{L-1} \boldsymbol{\alpha}_{L,i'} \frac{\partial \mathbf{T}_{i'(L-1)} \boldsymbol{\beta}_{i',0}}{\partial p_k} + \frac{\partial \boldsymbol{\alpha}_{L,k}}{\partial p_k} \mathbf{T}_{k(L-1)} \boldsymbol{\beta}_{k,0}$$

2. $k = L$

$$\frac{\partial U}{\partial p_k} = 0 - \mathbf{T}_{L(1)} \sum_{i'=1}^{L-1} \left[\frac{\partial \boldsymbol{\alpha}_{L,i'}}{\partial p_k} \mathbf{T}_{i'(L-1)} \boldsymbol{\beta}_{i',0} \boldsymbol{\beta}_{0,i'} \boldsymbol{\alpha}_{i',L} - \boldsymbol{\alpha}_{L,i'} \mathbf{T}_{i'(L-1)} \boldsymbol{\beta}_{i',0} \boldsymbol{\beta}_{0,i'} \frac{\partial \boldsymbol{\alpha}_{i',L}}{\partial p_k} \right]$$

$$\frac{\partial V}{\partial p_k} = \frac{\partial \boldsymbol{\beta}_{L,0}}{\partial p_k} + \sum_{i'=1}^{L-1} \frac{\partial \boldsymbol{\alpha}_{L,i'}}{\partial p_k} \mathbf{T}_{i'(L-1)} \boldsymbol{\beta}_{i',0}.$$

The derivatives of the translation matrices $\boldsymbol{\beta}$ and $\boldsymbol{\alpha}$ can be taken easily using the definitions of these matrices given in Appendix A, and the identity [62]:

$$\frac{d}{dx} \mathcal{Q}_p(ax) = \frac{a}{2} [\mathcal{Q}_{p-1}(ax) - \mathcal{Q}_{p+1}(ax)],$$

where \mathcal{Q} is either the Bessel function J or the Hankel function H , and a is a scalar.

These general expressions are greatly simplified for two scatterers. For reference, we present the derivatives for two scatterers. Equation (D.2) can be written as:

$$\psi^{sca} = \underline{\psi}^T \boldsymbol{\beta}_{0,1} \mathbf{T}_{1(2)} \boldsymbol{\beta}_{1,0} \underline{a} + \underline{\psi}^T \boldsymbol{\beta}_{0,2} \mathbf{T}_{2(2)} \boldsymbol{\beta}_{2,0} \underline{a}$$

and (D.3) for $k = 1, 2$ can be written as:

$$\frac{\partial \psi^{sca}}{\partial p_1} = \underline{\psi}^T \left[\frac{\boldsymbol{\beta}_{0,1}}{\partial p_1} \mathbf{T}_{1(2)} \boldsymbol{\beta}_{1,0} + \boldsymbol{\beta}_{0,1} \frac{\partial \mathbf{T}_{1(2)} \boldsymbol{\beta}_{1,0}}{\partial p_1} \right] \underline{a} + \underline{\psi}^T \boldsymbol{\beta}_{0,2} \frac{\partial \mathbf{T}_{2(2)} \boldsymbol{\beta}_{2,0}}{\partial p_1} \underline{a}$$

$$\frac{\partial \psi^{sca}}{\partial p_2} = \underline{\psi}^T \boldsymbol{\beta}_{0,1} \frac{\partial \mathbf{T}_{1(2)} \boldsymbol{\beta}_{1,0}}{\partial p_2} \underline{a} + \underline{\psi}^T \left[\frac{\boldsymbol{\beta}_{0,2}}{\partial p_2} \mathbf{T}_{2(2)} \boldsymbol{\beta}_{2,0} + \boldsymbol{\beta}_{0,2} \frac{\partial \mathbf{T}_{2(2)} \boldsymbol{\beta}_{2,0}}{\partial p_2} \right] \underline{a}.$$

Bibliography

- [1] A. Şahin and E.L. Miller, “Object-Based Localization of Buried Objects Using High Resolution Array Processing Techniques”, in *Proc. of SPIE– AeroSense:Detection and Remediation Technologies for Mines and Minelike Targets*, May 1996, vol. 2765, pp. 409–419.
- [2] A. Şahin and E.L. Miller, “Performance Bounds for Matched Field Processing in Sub-surface Object Detection Applications”, in *Proc. of SPIE– AeroSense:Detection and Remediation Technologies for Mines and Minelike Targets III*, April 1998, vol. 3392.
- [3] A. Şahin and E.L. Miller, “Object Detection Using High-Resolution Near-Field Array Processing”, *IEEE Trans. on Geoscience and Remote Sensing*, Submitted for Review.
- [4] A.J. Witten and J.E. Molyneux, “Ground Penetrating Radar Tomography: Algorithms and Case Studies”, *IEEE Trans. Geoscience and Remote Sensing*, vol. 32, pp. 461–467, March 1994.
- [5] E. Wolf, “Three-dimensional structure determination of semi-transparent objects from homographic data”, *Opt. Commun.*, vol. 1, pp. 153–156, 1969.

- [6] T.M. Habashy, R.W. Groom, and B.R. Spies, “Beyond the Born and Rytov Approximations: A Nonlinear Approach to Electromagnetic Scattering”, *Journal of Geophysical Research*, vol. 98, no. B2, pp. 1759–1775, February 1993.
- [7] A.J. Devaney and M.L. Oristaglio, “Inversion Procedure for Inverse Scattering Within the Distorted Wave Born Approximation”, *Physical Review Letters*, vol. 51, no. 4, July 1983.
- [8] W.C Chew and Y.M. Wang, “Reconstruction of Two-Dimensional Permittivity Distribution Using the Distorted Born Iterative Method”, *IEEE Trans. on Medical Imaging*, vol. 9, no. 2, pp. 218–225, June 1990.
- [9] G. Beylkin and M.L. Oristaglio, “Distorted-wave Born and Distorted-wave Rytov Approximation”, *Opt. Commun.*, vol. 53, 1985.
- [10] R.F. Harrington, *Field Computation by Moment Methods*, IEEE Press, (Originally published: Malabar, Fla. :R.E. Krieger, 1968), 1993.
- [11] V. Rokhlin, “Rapid Solution of Integral Equations of Scattering Theory in Two Dimensions”, *Journal of Computational Physics*, vol. 86, no. 2, pp. 414–439, 1990.
- [12] A. Taflov, *Computational Electrodynamics: The Finite-difference Time-domain Method*, Artech House, Boston, 1995.
- [13] M.N.O Sadiku, *Numerical Techniques in Electromagnetics*, CRC Press, Boca Raton, Fla., 1992.

- [14] W.C. Chew and Y.M. Wang, “A Fast Algorithm for Solution of a Scattering Problem Using a Recursive Aggregate τ Matrix Method”, *Microwave and Optical Technology Letters*, vol. 3, no. 5, pp. 164–169, May 1990.
- [15] Y.M. Wang and W.C. Chew, “An Efficient Algorithm for Solution of a Scattering Problem”, *Microwave and Optical Technology Letters*, vol. 3, no. 3, pp. 102–106, March 1990.
- [16] A. Şahin and E.L. Miller, “Recursive T-matrix Algorithm for Multiple Metallic Cylinders”, *Microwave Opt. Tech. Lett.*, vol. 15, no. 6, pp. 360–363, August 1997.
- [17] A. Şahin and E.L. Miller, “Recursive T-matrix Methods for Scattering from Multiple Dielectric and Metallic Objects”, *IEEE Trans. on Antennas and Propagation*, vol. 46, no. 5, pp. 672–678, May 1998.
- [18] Y.M. Wang and W.C. Chew, “An iterative solution to the two-dimensional electromagnetic inverse scattering problem”, *Intl. Journal of Imaging Systems and Technology*, vol. 1, no. 1, pp. 100–108, 1989.
- [19] E.L. Miller, *The Application of Multiscale and Stochastic Techniques to the solution of Inverse Problems*, PhD thesis, M.I.T., Cambridge, MA, August 1994.
- [20] N. Joachimowicz, C. Pichot, and J.P. Hugonin, “Inverse Scattering: An Iterative Numerical Method for Electromagnetic Imaging”, *IEEE Trans. on Antennas and Propagation*, vol. 39, no. 12, pp. 1742–1752, December 1991.

- [21] E.L. Miller and A.S. Willsky, “A Multiscale, Statistically Based Inversion Scheme for Linearized Inverse Scattering Problems”, *IEEE Trans. on Geoscience and Remote Sensing*, vol. 34, no. 2, pp. 346–357, March 1996.
- [22] E.L. Miller and A.S. Willsky, “Multiscale, Statistical Anomaly Detection Analysis and Algorithms for Linearized Inverse Scattering Problems”, *Multidimensional Systems and Signal Processing*, vol. 8, pp. 151–184, 1996.
- [23] W.C. Chew, J.A. Friedrich, and R. Geiger, “A Multiple Scattering Solution for Effective Permittivity of a Sphere Mixture”, *IEEE Trans. Geoscience and Remote Sensing*, vol. 28, no. 2, pp. 207–214, March 1990.
- [24] W.C. Chew, Y.M. Wang, and L. Gürel, “Recursive Algorithm for Wave-Scattering Solutions Using Windowed Addition Theorem”, *Journal of Electromagnetic Waves and Applications*, vol. 6, no. 11, pp. 1537–1560, 1992.
- [25] W.C. Chew, L. Gürel, Y.M. Wang, G. Otto, and R.L. Wagner Q.H. Liu, “A Generalized Recursive Algorithm for Wave-Scattering Solutions in Two Dimensions”, *IEEE Trans. on Microwave Theory and Techniques*, vol. 40, no. 4, pp. 716–722, April 1992.
- [26] L. Gürel and W.C. Chew, “A Recursive T-matrix Algorithm for Strips and Patches”, *Radio Science*, vol. 27, pp. 387–401, May-June 1992.
- [27] L. Gürel and W.C. Chew, “Scattering Solution of Three-dimensional Array of Patches Using the Recursive T-matrix Algorithms”, *IEEE Microwave and Guided Wave Lett.*, vol. 2, pp. 182–184, May 1992.

- [28] H. Krim and M. Viberg, “Two Decades of Array Signal Processing Research: The Parametric Approach”, *IEEE Signal Processing Magazine*, pp. 67–94, July 1996.
- [29] M. Bouvet and G. Biennu, Eds., *High-Resolution Methods in Underwater Acoustics*, Springer-Verlag, Heidelberg, Germany, 1991.
- [30] A.B. Baggeroerr, W.A. Kupperman, and P.N. Mikhalevsky, “An Overview of Matched Field Methods in Ocean Acoustics”, *IEEE J. of Oceanic Engineering*, vol. 18, no. 4, pp. 401–424, October 1993.
- [31] A. Tolstoy, *Matched Field Processing for Underwater Acoustics*, World Scientific, Singapore, 1993.
- [32] H.P. Bucker, “Use of calculated sound fields and matched field detection to locate sound sources in shallow water”, *J. of the Acoustical Soc. of America*, vol. 59, no. 2, pp. 368–373, 1976.
- [33] W.C. Chew, *Waves and Fields in Inhomogeneous Media*, Van Nostrand Reinhold, 1990.
- [34] W.C. Chew and G.P. Otto, “Microwave Imaging of Multiple Conducting Cylinders Using Local Shape Functions”, *IEEE Microwave and Guided Wave Letters*, vol. 2, no. 7, pp. 284–286, July 1992.
- [35] A.N. Tikhonov and V.Y. Arsenin, *Solutions to Ill-Posed Problems*, V.H. Winston & Sons, 1977.

- [36] C.W. Groetsch, *The Theory of Tikhonov Regularization for Fredholm Equations of the First Kind*, Pitman Publishing Limited, Boston, 1984.
- [37] H.T. Lin and Y.W. Kiang, "Microwave Imaging for a Dielectric Cylinder", *IEEE Trans. on Microwave Theory and Techniques*, vol. 42, no. 8, pp. 1572–1579, August 1994.
- [38] Y. Bresler, J.A. Fessler, and A. Macovski, "Model-Based Estimation Techniques for 3-D Reconstruction from Projections", *Machine Vision and Applications*, vol. 1, pp. 115–126, 1988.
- [39] D.J. Rossi and A.S. Willsky, "Reconstruction from Projections Based on Detection and Estimation of Objects— Parts I and II: Performance Analysis and Robustness Analysis", *IEEE Trans. on Acoustics, Speech and Signal Processing*, vol. 32, no. 4, pp. 886–906, August 1984.
- [40] A.J. Devaney and G.A. Tsihrintzis, "Maximum Likelihood Estimation of Object Location in Diffraction Tomography", *IEEE Trans. on Signal Processing*, vol. 39, no. 3, pp. 672–682, March 1991.
- [41] A. Schatzberg, A.J. Devaney, and A.J. Witten, "Estimating Target Location from Scattered Field Data", *Signal Processing*, vol. 40, pp. 227–237, 1994.
- [42] L. Gürel and W.C. Chew, "Recursive T-matrix Algorithms with Reduced Complexities for Scattering from Three-dimensional Patch Geometries", *IEEE Trans. Antennas Propagat.*, vol. AP-41, pp. 91–99, January 1993.

- [43] M. Baquero, J. Fortuny, G. Nesti, and A.J. Sieber, “3-D Polarimetric Superresolution Radar Imaging Using the MUSIC Algorithm”, Tech. Rep. I.96.72, European Commission Joint Research Centre, Space Applications Institute, Ispra, Italy, May 1996.
- [44] H. Akaike, “Maximum Likelihood Identification of Gaussian Autoregressive Moving Average Models”, *Biometrika*, vol. 60, pp. 255–265, 1973.
- [45] H. Akaike, “A New Look at the Statistical Model Identification”, *IEEE Trans. on Automatic Control*, vol. 19, pp. 716–723, 1974.
- [46] J. Rissanen, “Modelling by Shortest Data Description”, *Automatica*, vol. 14, pp. 465–471, 1978.
- [47] G. Schwartz, “Estimating the Dimension of a Model”, *Ann. Stat.*, vol. 6, pp. 461–464, 1978.
- [48] R.O.Schmidt, “Multiple Emitter Location and Signal Parameter Estimation”, *IEEE Trans. Antennas and Propagation*, vol. AP-34, no. 3, pp. 276–280, March 1986.
- [49] P. Stoica and A. Nehorai, “MUSIC, Maximum Likelihood, and Cramer-Rao Bound”, *IEEE Trans. Acoust., Speech, Signal Processing*, vol. 37, no. 5, pp. 720–741, May 1989.
- [50] S. Valaee, B. Champagne, and P. Kabal, “Parametric Localization of Distributed Sources”, *IEEE Transactions on Signal Processing*, vol. 43, no. 9, pp. 2144–2153, September 1995.

- [51] J.W. Choi and Y.H. Kim, “Spherical Beam-Forming and MUSIC Methods for the Estimation of Location and Strength of Spherical Sound Sources”, *Mechanical Systems and Signal Processing*, vol. 9, no. 5, pp. 569–588, 1995.
- [52] J.W. Choi and Y.H. Kim, “Estimation of Locations and Strengths of Broadband Planar and Spherical Noise Sources Using Coherent Signal Subspace”, *Journal of Acoustical Society of America*, vol. 98, no. 4, pp. 2082–2093, October 1995.
- [53] Y.D. Huang and M. Barkat, “Near-Field Multiple Source Localization by Passive Sensor Array”, *IEEE Transactions on Antennas and Propagation*, vol. 39, no. 7, pp. 968–974, July 1991.
- [54] N. Yuen and B. Friedlander, “Performance Analysis of Higher Order ESPRIT for Localization of Near-Field Sources”, *IEEE Transactions on Signal Processing*, vol. 46, no. 3, pp. 709–719, March 1998.
- [55] P.C. Waterman, “New Formulation of Acoustic Scattering”, *J. Acoust. Soc.*, vol. 45, no. 6, pp. 1417–1429, 1969.
- [56] P.C. Waterman, “Symmetry, Unitarity and Geometry in Electromagnetic Scattering”, *Physical Review D*, vol. 3, no. 4, pp. 825–839, February 1971.
- [57] B. Peterson and S. Ström, “T Matrix for Electromagnetic Scattering from an Arbitrary Number of Scatterers and Representations of $E(3)$ ”, *Physical Review D*, vol. 8, no. 10, pp. 3661–3678, November 1973.

- [58] B. Peterson and S. Ström, “Matrix Formulation of Acoustic Scattering from an Arbitrary Number of Scatterers”, *J. Acoust. Soc. Am.*, vol. 56, no. 3, pp. 771–780, September 1974.
- [59] V.K. Varadan and V.V. Varadan, Eds., *Acoustic, electromagnetic, and elastic wave scattering—focus on the T-matrix approach*, Pergamon Press, 1980.
- [60] Y.M. Wang, *Theory and Applications of Scattering and Inverse Scattering Problems*, PhD thesis, University of Illinois, Urbana-Champaign, IL, 1991.
- [61] P. Stoica and A. Nehorai, “MUSIC, Maximum Likelihood, and Cramer-Rao Bound: Further Results and Comparisons”, *IEEE Trans. Acoust., Speech, Signal Processing*, vol. 38, no. 12, pp. 2140–2150, December 1990.
- [62] G.N. Watson, *A Treatise on the Theory of Bessel Functions*, Cambridge University Press, second edition, 1966.
- [63] A.Z. Elsherbeni and M. Hamid, “Scattering by Parallel Conducting Circular Cylinders”, *IEEE Trans. on Antennas and Propagation*, vol. 35, no. 3, pp. 355–358, March 1987.
- [64] K.K. Mei and J.G. Van Bladel, “Scattering by perfectly conducting rectangular cylinders”, *IEEE Trans. on Antennas and Propagation*, vol. 11, pp. 185–192, 1963.
- [65] M. Ouda, M. Hussein, and A. Sebak, “Multiple Scattering by Dielectric Cylinders Using a Multi-filament Current Model”, *Journal of Electromagnetic Waves and Applications*, vol. 7, no. 2, pp. 215–234, 1993.

- [66] D.L. Snyder and M.I. Miller, *Random Point Processes in Time and Space*, Springer-Verlag New York Inc., 2nd edition, 1991.
- [67] C.A. Balanis, *Advanced Engineering Electromagnetics*, John Wiley and Sons, Inc, New York, 1989.
- [68] D. C. Hoaglin, “A Poissones Plot”, *The American Statistician*, vol. 34, no. 3, pp. 146–149, August 1980.
- [69] J.E. Hipp, “Soil Electromagnetic Parameters as Functions of Frequency, Soil Density, and Soil Moisture”, *Proceedings of the IEEE*, vol. 62, no. 1, pp. 98–103, January 1974.
- [70] J.A. Kong, *Electromagnetic Wave Theory*, John Wiley & Sons, 1986.
- [71] P.E. Gill, W. Murray, and M.H. Wright, *Practical Optimization*, Academic Press, Inc., San Diego, CA, 1981.
- [72] S.D. Silvey, *Statistical Inference*, Chapman and Hall Ltd., 1975.
- [73] W.H. Press, B.P. Flannery, S.A. Teukolsky, and W.T. Vetterling, *Numerical Recipes*, Cambridge University Press, Cambridge, UK, 1986.
- [74] G. Kristensson and S. Ström, “The T Matrix Approach to Scattering from Buried Inhomogeneities”, in *Acoustic, electromagnetic, and elastic wave scattering—focus on the T-matrix approach*, V.K. Varadan V.V. Varadan, Ed., pp. 135–167. Pergamon Press, 1980.